Additive-Free Near-Intrinsic Narrow Band Gap Perovskites via Sequential Thermal Evaporation

for Photovoltaic Applications

N. van Silfhout

TU Delft

Additive-Free Near-Intrinsic Narrow Band Gap Perovskites via Sequential Thermal Evaporation

for Photovoltaic Applications

by

N. van Silfhout

A thesis
submitted in partial fulfilment of the requirements for
the degree of Master of Science in Chemical Engineering
at the Delft University of Technology,
to be defended publicly on
Monday April 15th, 2024 at 1:15 PM

Student number:	4771311
Project duration:	September 4th, 2023 - April 15th, 2024
Thesis committee:	Prof. Dr. T.J. Savenije, Supervisor
	Prof. Dr. L. Mazzarella
	Prof. Dr. S.J. Picken
Daily Supervisor:	L. van der Poll

An electronic version of this thesis is available at http://repository.tudelft.nl/.

TU Delft

ABSTRACT

Tin/lead (Sn/Pb) iodide perovskites (PVKs) have emerged as promising absorber layer materials for high-efficiency tandem solar cells due to their low cost, high light absorption coefficients, and narrow band gaps. However, current solvent-based synthesis techniques offer poor scalability, in turn hindering commercialization.

This study introduces sequential thermal evaporation (STE) as a scalable method for producing narrow band gap Sn/Pb iodide PVK absorber layers for application in solar cells. The produced thin films show low doping densities, charge carrier mobilities close to 100 cm^2/Vs, and charge carrier lifetimes of over 2 μs. Contrary to the established convention in solvent-based synthesis, no additives were required.

An alloy of precursors ($PbSnI_4$) was used in the deposition, lowering the number of required sources and increasing the production rate. Optimal annealing temperatures for $FAPb_{0.5}Sn_{0.5}I_3$ and $Cs_{0.05}FA_{0.95}Pb_{0.5}Sn_{0.5}I_3$ produced via STE were determined at 200 °C, showing significant improvements in charge carrier mobilities and lifetimes compared to lower annealing temperatures. The drastic increase in performance was ascribed to a recrystallization mechanism. Contrary to spin coating-based research, the introduction of cesium into the PVK structure led to reduced charge carrier mobility and lifetime. The underlying mechanism remains unclear. Addition of tin(II)fluoride (SnF_2) led to reduced charge carrier mobilities and lifetimes, with slight improvement in morphology. However, its direct effects were uncertain, questioning its necessity in vacuum deposition methods for Sn-based PVK films.

This works demonstrates the significant potential of STE for the production of near-intrinsic high-performance Sn/Pb iodide PVKs for solar cell applications.

CONTENTS

1

INTRODUCTION

Over the last decade, tremendous effort has been invested into researching metal halide perovskites (MHPs) for application in solar cells.[1–6] Not without reason, MHPs offer many advantages over conventional absorber layer materials, such as lower material cost,[7] improved carrier dynamics,[8, 9] high light absorption coefficients,[10] and a tunable band gap.[11] The power conversion efficiency (PCE) of lab-scale MHP solar cells has reached over 25%, competing with convectional silicon-based solar cells.[12]

Solar cells consisting of a single absorber layer have a physical radiative efficiency limit of 33%. This limit arises from the energy losses through thermalization of high-energy photons and failing to absorb below band gap photons.[13] To go beyond this limit, solar cells with multiple absorber layers (multi-junction) with dissimilar band gaps are required. Due to their tunable absorption bandwidths[14, 15] in combination with favourable optoelectronic properties[11, 16, 17], MHPs are perfect candidates for implementation in multi-junction solar cells.[18] Multi-junction perovskite solar cells (PSCs) theoretically offer PCEs of over 50%.[18–20]

To reach PCEs of over 40%, band gaps smaller than 1.3 eV are required.[18, 20] Due to a phenomenon called ”band gap bowing”, tin/lead (Sn/Pb) iodide MHPs can exhibit band gaps as small as 1.1 eV.[21] These narrow band gaps will in theory lead to highly effective tandem and triple-junction architectures. However, MHPs are faced with many challenges. The inherent poor chemical stability of Sn/Pb iodide MHP materials against moisture and oxygen greatly hinders practical application.

Currently, MHP absorber layers are most often deposited using solution-based techniques such as spin coating. Spin coating is ideal for quick iteration at lab-scale due to short processing time, low capital investment cost, as well as ambient processing conditions.[22, 23] To mitigate some of the degradation, it has become standard practice to use additives such as tin(II)fluoride (SnF_2) in spin coating.[24] However, when it comes to commercial-scale production, the limitations of solution-based techniques become apparent: Inconsistent thicknesses over larger areas and incompatibility with complex geometries.[18] For commercialization of PSCs, it is essential to overcome these limitations.

One of the main proposed alternatives for scalable production of MHPs is thermal evaporation (TE). In TE, the required precursors are sublimated by heating, which then get deposited onto the target substrate while under a vacuum. TE is solvent-free and is able to conformally coat complex geometries while staying uniform over larger areas.[25, 26] Without solvents, one of the major causes for degradation in Sn-containing perovskite (PVK) materials is avoided.[27–29] In addition, using TE it is possible to create complete solar cell devices, both single-junction and multi-junction.[30, 31]

When it comes to research output, TE techniques significantly lag behind spin coating due to their higher capital investment costs and slower iteration speeds.[26, 31] Among the TE techniques, co-deposition is currently the most well researched for the production of MHPs.[25, 26] In co-deposition, the required compounds are sublimated and deposited simultaneously. The composition is determined by precisely tuning the deposition rate of each precursor. The formation of the PVK phase in co-deposition is complex and difficult to control, consisting of a multitude of vapour-vapour and vapour-solid interactions.[25] To allow for more precise control over PVK composition and formation, the precursors can instead be deposited individually, this is called sequential thermal evaporation (STE). In STE, the PVK phase forms in a solid-vapour reaction.[32–34]

Top-performing spin-coated PVK materials often consist of four or more different components, plus an additive.[35, 36] However, TE techniques are limited in the compositions they can achieve by the number of available sources. In addition, STE is severely underrepresented in research, as of writing this work, no research has been published on the STE of Sn/Pb-based perovskites. In addition, due to the difference in formation mechanism, knowledge gained in spin coating and co-deposition research might no be transferable.

1.1. Research Objectives

This study aims to explore STE as a scalable method for producing narrow band gap (approximately 1.25 eV) Sn/Pb iodide PVK absorber layers for application in solar cells. In addition, this work seeks to establish a foundation for future work by uncovering similarities and differences in research outcomes compared to more conventional techniques such as spin coating and co-deposition. The following research objectives were formulated:

1. Reduce the number of required sources by using lead(II)tin(II)iodide(+10 mol% SnF_2) ($PbSnI_4$) in the production of narrow band gap Sn/Pb iodide PVK absorber layers via STE.
2. Determine the optimal annealing temperature for organic and organic-inorganic Sn/Pb iodide PVK absorber layers synthesized via thermal evaporation.
3. Explore the role of excess SnF_2 on Sn/Pb iodide PVK materials produced via STE.
4. Investigate the influence of the substitution of formamidinium (FA^+) with cesium (Cs^+) in varying fractions on the optoelectronic properties, crystallographic characteristics, and morphology of Sn/Pb iodide PVK absorber layers synthesized via STE.

2

THEORY

2.1. Perovskite Solar Cells

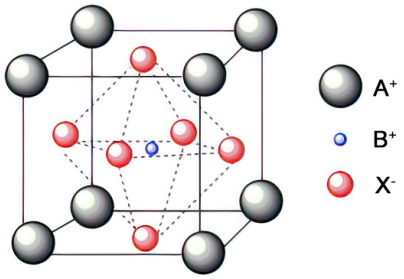

Figure 2.1: A unit cell of the perovskite crystal structure, where A and B are cations and X is an anion.[37]

Perovskites (PVKs) are a category of crystal structures with the chemical composition ABX_3, where A and B are cations and X is an anion (figure 2.1). Metal halide perovskites (MHPs) are a specific group within this category where the B site is occupied by a divalent cation and the X site is occupied by a halide. MHPs have garnered large amounts of interest in the last decade for their application in solar cells[2], not without reason. MHPs offer favourable optoelectronic properties, such as: high charge carrier lifetime mobility product[11, 16, 17], low exciton binding energy[38], a direct and tunable band gap[14, 15] and a high light absorption coefficient[39]. Furthermore, the optoelectronic properties of MHPs can be adjusted via compositional engineering[40] in a way that is not possible with conventional semi-conductor materials. In addition, The low cost of the precursors combined with the high absorption coefficient means that less material is required and total costs are lower than with conventional solar cell materials.[39, 41, 42]

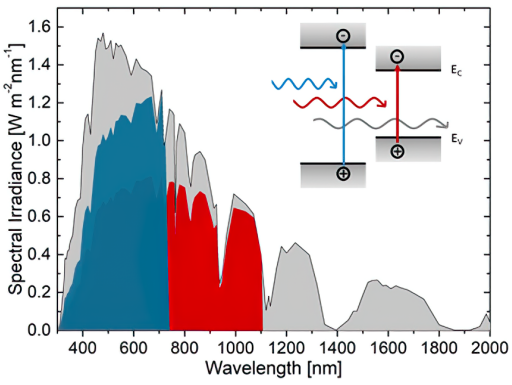

Figure 2.2: The solar radiation spectrum (AM1.5) shown in gray. The detailed balance limit for a single-junction solar cell is shown in red. Note that a large part of the solar radiation spectrum is not covered. By adding a second absorber layer (blue) with a larger band gap, the coverage of the solar spectrum is increased.[43]

Conventional solar cells consist of an active layer containing a single p-(i-)n or n-(i-)-p junction. Power conversion efficiencies (PCE) of single junction solar cells are currently approaching the detailed balance limit of 33%[13], a fundamental restriction in the maximum attainable efficiency (figure 2.2). The detailed balance limit is a consequence of absorber materials with a single band gap. Energy efficiency is limited due to below-band gap photons failing to absorb and thermal relaxation of above-band gap photons.

A possible solution to improve PCEs past the detailed balance limit, is the use of multi-junction architectures. By combining two or more different active layers with dissimilar band gaps, the maximum area of the solar spectrum that can be covered increases (figure 2.2). This way, the efficiency losses due to below and above-band gap photons are decreased, increasing the maximum attainable PCE. MHP double- and triple-junction cells have a calculated maximum PCE of over 50%[19, 20]. Reaching a PCE limit of over 40% with multi-junction solar cells requires a base absorber layer with a narrow band gap (<1.3 eV)[18, 20].

2.2. Tin/Lead Perovskites

Tin/lead (Sn/Pb) iodide perovskites can have band gaps as narrow as 1.17 eV[44, 45], lower than what is possible using either pure lead (Pb) iodide (1.6 eV)[46–48] or tin (Sn) iodide perovskites (1.3 eV)[49–51]. This small band gap is possible because of a phenomenon called band gap bowing. Literature on the exact nature of band gap bowing is conflicting, but DFT and QSGW calculations have shown that the effect is not likely caused by spin-orbit coupling or changes in the crystal structure, but rather a product of the mismatch in energy between the s and p orbitals of Pb and Sn which make up the edge states of the band gap[52]. By modifying the ratio of Sn and Pb, a band gap between 1.2 and 1.6 eV can be attained.

In addition to the benefit of a small and widely tunable band gap, Sn/Pb halide perovskites offer a potential improvement in charge-carrier mobility[53–55], charge-carrier cooling[56–58] and exciton binding energy[54, 59–61] over pure Pb halide perovskites.

2.2.1. Phase Transitions

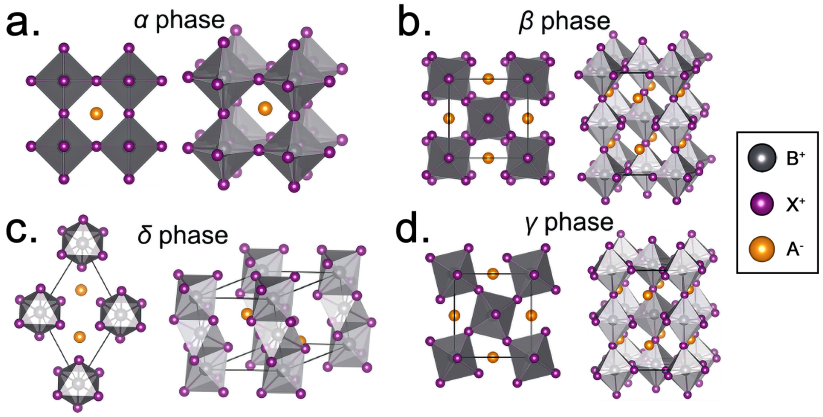

Figure 2.3: The four different crystal phases: the cubic α phase (**a.**), the tetragonal β phase (**b.**), the δ phase, in this case depicted as trigonal (**c.**), and the orthorhombic γ phase (**d.**).[62]

A PVK material that exhibits a cubic crystal structure with the Pm3m space group is generally preferred for solar cell applications. This configuration, that is called the α-phase (figure 2.3 **a.**), often shows the best optoelectronic characteristics for use in solar cells and the smallest band gap.[62–64] Changes in temperature, pressure or composition can lead to octahedral tilting and displacement of the A and B cations, causing the PVK material to deviate from the cubic phase and undergo transitions into other phases, such as the tetragonal β-phase, the orthorhombic γ-phase, or the hexagonal, orthorhombic or trigonal δ-phase (figure 2.3 **b.** to **d.**).[62]

The transition from the α-phase to either the tetragonal β-phase or the orthorhombic γ-phase

induces notable changes in band gap size, charge carrier mobilities and lifetimes, as well as thermal and oxidative stability.[65] Despite these changes, the relatively minor deviation from the cubic structure preserves the perovskite structure and photoactivity. In contrast, a large deviation results in the presence of the non-perovskite δ-phase. This phase is generally considered unfavorable, it causes a large increase in band gap energy, which results in a significant reduction in photoactivity (at the wavelengths of interest).[62, 66]

The Goldschmidt tolerance factor (equation (2.1)) describes the distortion of the crystal structure and can be used as a predictor for the stability of the photoactive phases.

$$\tau = \frac{r_A + r_B}{\sqrt{2}(r_B + r_X)} \tag{2.1}$$

Where τ is the Goldschmidt tolerance factor and r_A, r_B, and r_X are the atomic radius of ions A^+, B^{2+}, and X^-. A tolerance factor between 0.85 and 1 leads to a stable (pseudo)cubic photoactive phase at ambient conditions.[65–67]

2.2.2. A-site Design

The composition of the A-site should have minimal direct effect on the optoelectronic properties of a Sn/Pb PVK material, as the electronic states associated with the A-site are situated deep into the conduction and valence band. However, alterations in the size and shape of the A cation influence the aforementioned Goldschmidt tolerance factor and can cause significant lattice distortion. This lattice distortion alters the electronic structure of the PVK, resulting in a change in band gap size, charge carrier mobilities and lifetimes, and (phase) stability.[68, 69]

The three most common A-site cations in MHP research are methylammonium (MA^+), formamidinium (FA^+), and cesium (Cs^+). Over time, MA^+ has become less popular due to concerns over its poor atmospheric and thermal stability. In Pb-based MHPs, the addition of Cs^+ has been shown to improve optoelectronic properties as well as thermal stability.[70–72] Based on the results from Pb-based PVKs, most top performing Sn/Pb iodide PVKs in research have an A-site composition of $Cs_{0.2-0.3}FA_{0.8-0.7}$.[73] However, the effect of A-site size and composition of Sn/Pb iodide PVKs on optoelectronic properties and phase stability has yet to be quantified in research.

2.3. Tin Oxidation

A major hurdle in the development of MHPs is their poor chemical stability[27, 74–80]. Pure Sn-based MHPs are known to degrade in minutes upon contact with oxygen and/or water.[74, 81, 82] The limited research into Sn/Pb PVKs has shown that the addition of Pb greatly improves the stability over pure Sn PVKs.[76, 83] However, the stability is still significantly reduced compared to pure Pb halide PVKs.[76]

Research on pure Sn halide PVKs has shown that the degradation is driven by the oxidation of Sn.[29, 76, 82] The relatively facile oxidation of Sn^{2+} to Sn^{4+}, demonstrated by the low reduction potential of +0.15 V vs +1.67 V for Pb (Pb^{4+}/Pb^{2+}), causes trapping and self-p-doping behaviour, lowering charge carrier lifetime and mobility[79, 84, 85].

2.3.1. Mechanism and Effects

Currently, no research has been published on the degradation mechanisms of Sn in Sn/Pb PVK materials specifically, thus the theory presented in this section is based on research in pure Sn PVKs. The exact mechanism and effects of Sn oxidation in Sn-based PVKs are still under debate.[29, 51, 79, 82, 85, 86] The oxidation of Sn within the MHP is generally understood to have three main effects:

1. **P-type doping:** Sn oxidation in the bulk leads to p-type doping. Sn^{4+} spontaneously reverts to Sn^{2+} by absorbing two electrons from the valence band, effectively releasing two holes. Upon contact with oxygen, I_2 is produced as a degradation product. I_2 can further increase the p-type doping by reacting with Sn, as demonstrated in equation equation (2.2).

$$Sn^{2+} + 2I_2 \rightarrow SnI_4 + 2h^+ \tag{2.2}$$

This self-p-doping behaviour leads to high background hole density and a decrease in charge carrier lifetime and diffusion length.[29, 79, 85]

2. **Creating Trap States:** Sn surface vacancies caused by Sn oxidation lead to under-coordinated iodide sites which are centers for non-radiative recombination. These tend to capture free charges, preventing their escape and increasing recombination.[29, 79, 86]
3. **Promoting degradation:** The creation of surface and interior Sn vacancies degrades the crystal lattice structure of the MHP. This degradation ultimately undermines the long-term stability of Sn-based perovskites leading to device failure.[29, 51] In addition, oxygen in combination with water can induce further degradation of the perovskite structure via a self-sustaining mechanism.[82]

2.3.2. Factors Leading to Tin Oxidation

Factors such as exposure to ambient oxygen and moisture encountered during fabrication and storage, play a major role in the degradation of Sn-based MHP. Even at the low oxygen and water concentrations of a glove box (<1ppm H_2O, O_2), degradation can be substantial.[29, 87]

Zhang et al.(2023) revealed that higher degradation rates occur under simultaneous exposure to light and oxygen.[29] Their research proposes that superoxides created by the interaction between oxygen and photoexcited electrons are the underlying cause. These superoxides can enter a reaction route that allows for the degradation of the entire perovskite structure without the initial availability of ambient moisture required under dark conditions.

Other sources of Sn oxidation can be traced back to the raw materials and their preparation. The highest available purity of 99.999% SnI_2 can still introduce significant amounts of SnI_4 into the final film.[29] Generally, observable doping can occur at concentrations as low as parts per billion. In addition, raw materials can be a source of oxygen, either in the form of neutral free oxygen (O_2) or bound oxygen (SnO_2, PbO, PbO_2, etc.).[27] Raw material oxidation can occur during handling and storage as well as production. For wet deposition techniques such as spin coating, solvents can be a cause of oxidation both in the precursors as well as the final film.[27–29]

2.4. Spin Coating

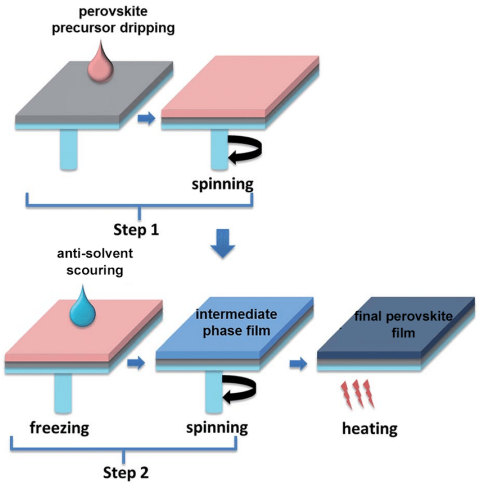

Figure 2.4: The two-step spin coating process. In the first step, a mixture of the perovskite precursors is drop casted and spun to form a uniform layer of solvent. In the next step, the precursor solution is formed to crystallize into the PVK phase by adding an anti-solvent. Afterwards the film is heated to drive off the remaining solvent.[88]

Currently, the most widely used method for preparing high-performance Sn/Pb PVK thin films at lab-scale is the two-step spin coating method. Figure 2.4 shows the basic working principle of two-step spin coating. In the initial step, a precursor solution containing both the metal halide salt (e.g., SnI_2) and the organic component (e.g., FAI) is deposited onto the substrate and spun, forming a thin layer of solvent. In the second step, an anti-solvent is applied to force the dissolved precursors to crystallize.

Finally, thermal annealing is used to improve morphology and ensure complete precursor conversion by promoting evaporation of the solvents.

Spin coating techniques are widely employed in research due to their cost-effectiveness and simplicity.[22, 23] In addition, spin coating allows for fast iteration. However, the commercialization of MHPs produced via spin coating faces numerous challenges. The crystallization of the perovskite phase, governed by numerous parameters, proves difficult to control,[89] leading to issues with morphology, surface coverage, uniformity, and reproducibility. Although spin coating allows for the production of cells with PCEs of over 26 %, the maximum size of these cells is less than 0.1 cm^2.[12] Achieving uniform depositions over larger areas is difficult, hindering performance of large-scale devices.[90, 91]

Alternative solution-based methods for large-scale production such as slot-die coating, blade coating, inkjet printing, and spray coating have been proposed.[89, 90, 92] However, apart from facing challenges over uniformity, solvent based techniques are inherently limited by their inability to conformally coat surface geometry.[30, 89, 90, 92] Conformal coating is critical when dealing with textured substrates such as silicon-based absorber layers. The inability to conformally coat complex geometries hinders the fabrication of PVK/Si tandem cells.[30, 93] In addition, the use of solvents in the fabrication of Sn-based MHPs introduces oxidation, severely limiting the performance without additives.[27–29]

2.4.1. Tin(II)Fluoride (SnF_2)

Sn(II)fluoride (SnF_2) has become ubiquitous as an additive in Sn/Pb PVKs produced via spin coating.[24] Due to the extent of the oxidation that occurs during synthesis, the performance of additive-free perovskites produced via spin coating is severely limited. The self p-doping leads to severely shortened charge carrier lifetimes and increased recombination. The addition of SnF_2 is required to sufficiently suppress the presence of Sn^{4+}. In addition, SnF_2 is shown to improve other properties of Sn-based PVKs, such as their thermal, oxidative and phase stability, film morphology and crystallinity.[24, 94]

In the early stages of Sn-based PVK development, SnF_2 was believed to reduce Sn^{4+} to Sn^{2+}.[95] Pascual et al.(2021) later revealed that fluoride anions preferentially bind to Sn^{4+} over Sn^{2+} in solution, forming SnF_4 complexes by a ligand exchange in solution as shown in equation 2.3.[24]

$$Sn(IV)I_4 + 2Sn(II)F_2 \rightarrow Sn(IV)F_4 + 2Sn(II)I_2 \tag{2.3}$$

They show that the formed SnF_4 exhibits minimal integration into the perovskite structure compared to SnI_4, leading to a reduction of Sn^{4+} in the film. In addition, Pascual et al. propose that the improved morphology and crystallization due to SnF_2 is owed to the promoted homogeneously distributed growth during nucleation in solution.[24]

2.5. Thermal Evaporation

The majority of research is conducted on MHPs made by solution processing methods, such as spin coating. Spin coating is accessible to most research groups due to the low cost and simplicity of the required equipment.[22, 23] Although spin coating is ideal for exploratory research, the poor uniformity over larger areas leads to poor scalability. For the commercial success of MHP solar cells, more research into scalable techniques is necessary.

One of the main proposed alternative is thermal evaporation (TE). TE is a vapour deposition technique where material is deposited via sublimation and desublimation onto a target substrate. TE offers several advantages over spin coating. TE techniques boast high uniformity over larger areas.[31]Furthermore, TE is solvent-free, avoiding one of the major causes for degradation in Sn-containing perovskite (PVK) materials.[27–29] This is corroborated in research by Yu et al.(2016), they show that additive-free production of low doping density Sn-based PVKs is possible using thermal evaporation.[96] In addition, TE boasts technological maturity in industry, improving feasibility for large-scale production.[31] Lastly, TE has the capability to conformally coat complex geometries,[26] critical for application in Si/PVK tandem solar cells.[30, 93] Using TE it is possible to create complete solar cell devices, both single-junction and multi-junction.[30, 31] However, when it comes to research output, TE techniques significantly lag behind spin coating due to their high capital cost, slower iteration rate and complexity.[26, 31]

2.5.1. Co-Deposition

Among the TE techniques, co-deposition is currently the most well-researched for the production of MHPs.[25, 26, 59] In co-deposition, multiple precursors are deposited simultaneously. The stoichiometry is controlled by varying the deposition rate of each precursor. Parameters such as the sticking coefficient, pressure in the deposition chamber and the deposition rate can have profound effects on the composition, morphology and overall uniformity of the final film. This means that the partial pressures of each component need to be accurately controlled for the right ratio of material to be deposited.

FORMATION AND GROWTH MECHANISM

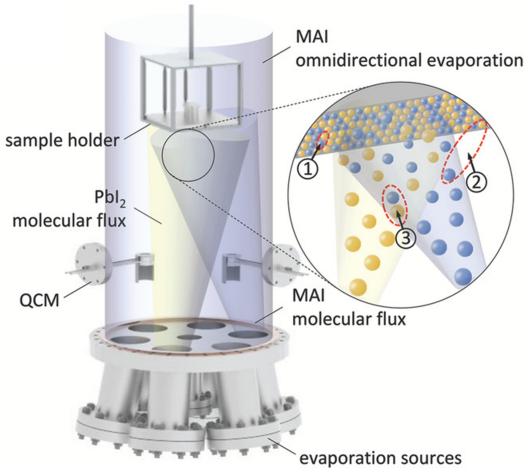

Figure 2.5: Figure showing the three types of formation and growth mechanisms that occur in co-deposition (of $MAPbI_3$), **1** as-deposited molecules interdiffuse forming and growing the PVK phase, **2** components on the surface and in vapour phase interact resulting in the formation and growth of the PVK phase, and **3** components in the vapour phase collide resulting in premature nucleation.[97]

The nucleation and growth of the PVK phase in co-deposition is complex and difficult to control, consisting of vapour-vapour, vapour-solid and solid-solid interactions (figure 2.5).[25, 97] The as-deposited solid mixture of components can interdiffuse and react to form the PVK phase (figure 2.5 ①). In addition, deposited molecules on the surface can interact with components in the vapour phase (figure 2.5 ②). As all components are evaporated simultaneously, collision between different precursors in vapour phase can result in nucleation before the substrate is reached figure 2.5 ③.[97] In co-deposition, nucleation is dominant over crystal growth, resulting in a small grain size without post-deposition treatments.[25, 97]

2.5.2. Sequential Deposition

In sequential deposition, the sources are evaporated individually. Sequential thermal evaporation (STE) allows for more precise control over stoichiometry, as rates and thickness of each precursor can be adjusted independently. Although the final composition is less affected by partial pressure, deviations can still affect the perovskite formation and the error in measured deposition rate.

FORMATION AND GROWTH MECHANISM

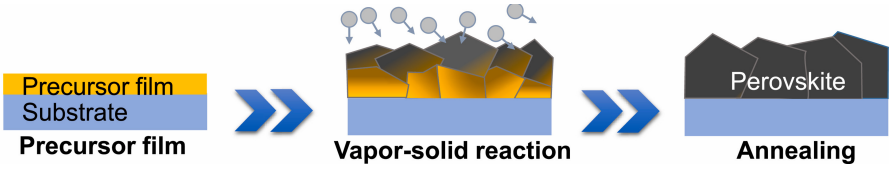

Figure 2.6: The perovskite growth mechanism in STE is based on interdiffusion of the vapour phase precursor into the yet-deposited precursor film.[98]

In STE, the first layer to be deposited is often the B-site precursor. In the production of perovskite solar cells (PVKs), significant lattice mismatches between substrates and precursors typically lead to weak binding forces.[99] Nucleation is energetically unfavorable compared to grain growth due to the predominant precursor-precursor binding force over the precursor-substrate binding force. However, deposition kinetics can influence this balance; an increase in deposition rate enhances nucleation, leading to the growth of nucleated islands and the formation of a polycrystalline precursor film. Due to the weak precursor-substrate interactions, STE often results in thin films with strong preferentially orientated crystal structures.[100]

Once the deposition of the first A-site species starts, the reaction undergoes a significant shift from a purely physical process to a combination of chemical and physical processes between the vapor-phase precursor and the solid substrate. Upon interaction between the yet deposited B-site precursor and the A-site molecules, the formation of the PVK phase starts to initiate (figure 2.6).[34, 98, 101, 102] Research indicates that the initial precursor layer serves as the framework for PVK phase formation, often referred to as the seed layer.[32, 33] Enhancing the morphology of this seed layer correlates with improvements in the final PVK structure.[34] Promoting large grains in absorber layers for PSCs has been shown to be advantageous for minimizing exciton binding energy, reducing carrier recombination losses, and enhancing photovoltaic performance.[25] Grain size regulation methods include controlling nucleation amount, adjusting annealing temperature, and stoichiometry control.[25]

2.5.3. Thermal Annealing

Despite in-situ PVK phase formation, the penetration depth of the gaseous precursor may be insufficient to convert the film. Complete PVK phase formation often requires in-situ or post-deposition annealing to promote inter-diffusion and increase reaction depth.[25] In addition to promoting the formation of PVK phase, thermal annealing can promote grain growth[25, 103] and transition the PVK from undesired to desired crystal phases.[62, 104–106]

MECHANISM

Although it is thermodynamically favourable for the system to move towards a lower energy state, the activation energy owed to the bond energy prevents spontaneous relaxation. Annealing supplies thermal energy, which allows the atoms to overcome bond energy, in turn allowing for the diffusion and rearrangement of atoms to a lower energy configuration. Annealing at higher temperatures leads to an increased diffusion rate.[107–109]

The promoted diffusion allows for the formation of the PVK phases from precursor material. For an existing PVK crystal structure, the annealing process works in three stages depending on time and temperature: recovery, recrystallization, and grain growth. During recovery, stresses due to dislocations in the original crystal structure are minimized. During recrystallization, new strain-free grains nucleate, replacing deformed ones. If annealing continues, the newly nucleated grains grow to larger sizes, minimizing surface energy.[107–109]

2.5.4. Lead(II)Tin(II)Iodide alloy

There has been a recent trend among the highest performing solution-processed Sn/Pb PVKs to move towards more complex compositional design, with compositions often containing three A-site ions (FA^+, MA^+, Cs^+), two B-site ions (Sn^{2+}, Pb^{2+}), in addition to additives (e.g. SnF_2).[35, 36] The composition of PVK materials produced via TE is limited by the number of sources. Although it is possible to expand the number of crucibles in a TE setup, it introduces complications in both co-deposition and sequential deposition. In co-deposition, a higher number of sources leads to more difficult control over stoichiometry, as the deposition rates need to be simultaneously controlled for all sources. In sequential deposition, additional sources lead to longer deposition times, as each source is deposited individually. Reducing the number of sources required in STE would significantly increase the production rate, in turn improving outlooks on commercialization.

One method for reducing the number of required sources is to combine several precursors in what is referred to as a melt or an alloy. Ball et al.(2019) employed a melt of cesium iodide (CsI), lead(II)iodide (PbI_2), and tin(II)iodide (SnI_2) to reduce the number of required sources from four to

two.[59] Other organic or mixed organic-inorganic melts have also been explored in Pb halide perovskites.[110, 111]

In research published in 1988, Kuku et al. demonstrated the successful synthesis of a PbI_2/SnI_2 alloy, called lead(II)tin(II)iodide ($PbSnI_4$). Their findings indicate a unique lattice parameter and a singular melting point, suggesting the formation of a single material or eutectic mixture.[112] In 1999, Kuku reported the vacuum deposition of a $PbSnI_4$ thin film on a glass substrate. Although they claim that analysis confirmed that these films maintained a stoichiometric composition, no data is provided to substantiate this claim.[113]

2.5.5. The role of SnF_2 in Thermal Evaporation

As stated in section 2.4.1, SnF_2 currently plays a vital role in the production of Sn-based PVKs. In spin coating, SnF_2 is necessary to sufficiently suppress the formation of Sn^{4+} and improve crystallization and morphology. However, the role of SnF_2 in TE is unclear.

Firstly, Yu et al.(2016) have proven that the production of low-doping density Sn-based PVKs is possible without SnF_2 using thermal evaporation.[96] This leads to the conclusion that STE as a technique inherently introduces significantly lower concentrations of Sn^{4+} than spin coating. As the main function of SnF_2 in spin coating is to suppress the formation of Sn^{4+}, the improvements to be gained by the addition of SnF_2 are unclear.

Multiple papers have however shown that SnF_2 can have a positive effect in PVKs produced via vacuum deposition techniques. Moghe et al.(2016) managed to improve the short circuit current density from 0 to 2.5 mA/cm^2 in $CsSnBr_3$ produced via STE upon the addition of 2.5 mol % SnF_2. The addition of SnF_2 also realized a significant increase in external quantum efficiency (EQE).[114] Igual-Munoz et al. (2019) show that the addition of 5 to 10 mol% excess SnF_2 in $FAPb_{0.5}Sn_{0.5}I_3$ produced via co-deposition leads to improved light absorption and a reduction in the excess PbI_2 and SnI_2 phase.[115] In research by Ball et al. (2019), SnF_2 is added substitutionally to a mixture of SnI_2, PbI_2 and CsI, and formed into a single precursor via a melt reaction. This alloy is then co-deposited in combination with FAI to form a PVK with the composition $Cs_{0.25}FA_{0.75}Pb_{0.5}Sn_{0.5}I_3$. At an SnF_2 substitution of 27 mol%, they report significant improvements over SnF_2-free samples, showing increased short circuit current density (4 vs 20 mA/cm^2), EQE and PCE (5 vs 12 %).[59]

Although these papers have shown an improvement in optoelectronic characteristics upon the addition of SnF_2 in PVKs produced via TE, it is yet unclear via which mechanism these effects are attained.

3
METHODS

3.1. Experimental Methods
3.1.1. Thermal Evaporation Setup

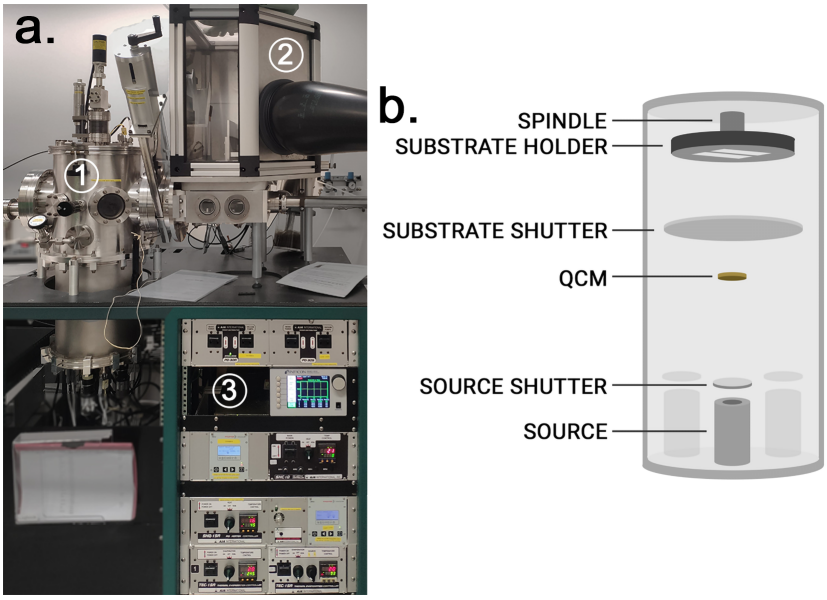

Figure 3.1: a. The STE setup consisting of **1** the deposition chamber, **2** The antechamber and load lock, and **3** the instrumentation panels, including the temperature controls. **b.** Diagram showing the main components inside the deposition chamber (**1**) of the STE setup.

The AJA international thermal evaporation setup (figure 3.1 **a.**) consists of a deposition chamber, a load lock, an antechamber and an instrumentation panel. All depositions performed during this research were controlled manually by raising and lowering the temperatures directly via the temperature controllers of each source (figure 3.1 **a.**, bottom right).

A diagram of the deposition chamber and its components can be found in figure 3.1. The substrate holder containing the quartz substrate covered with a mask is attached upside-down to the spindle, which provide rotation and height adjustment. The deposition rate is measured using the quart crystal microbalance (QCM). The source and substrate shutter can be opened independently to allow for adjusting the deposition rate before starting the deposition. The sources consist of a mantle, a heating coil and a crucible, which can be loaded with the desired component. The entire deposition chamber is kept under vacuum during depositions.

3.1.2. $PbSnI_4$(+10 mol% SnF_2) Alloy Synthesis

To both decrease the number of sources and allow for varying the A-site composition, this research proposes a melt based on the B-site precursors, PbI_2 and SnI_2. In previous work, $PbSnI_4$ was synthesized by putting equimolar amounts of PbI_2 and SnI_2 inside evacuated pyrex ampoules, which was heated to 500 °C for 48 hours.[112] This research introduces a simplified and shortened version of this procedure.

Equimolar amounts of PbI_2 and SnI_2 (and 10 mol% SnF_2) were added to a crucible, which was put inside one of the sources of the evaporation chamber (figure 3.1). Under N_2 atmosphere, the temperature of the crucible was raised to 420 °C. This temperature was then held for 20 min, before the heating was turned off. The detailed protocol for this procedure can be found in Appendix E.

3.1.3. Substrate Cleaning and (Un)Loading

The substrate were cleaned with 2-propanol (IPA) and acetone, and dried using a Kimtech Science tissue. Finally, the substrates were placed inside a Harrick Plasma plasma-ozone cleaner for ten minutes. Next, the quartz substrates were loaded into the substrate holder and transferred into the deposition chamber of the evaporation setup using the load lock.

After a deposition was completed, the thin films were transferred to antechamber of the evaporation setup and put inside a transfer unit while under N_2 atmosphere. The closed transfer unit containing the substrates was then brought into a glovebox for thermal annealing and/or storage. Detailed protocols for the preparation and loading of the quartz substrates can be found in Appendix E.

3.1.4. Deposition

After the substrate was loaded, the spindle was set to the correct height, and rotation was activated. No set rotation speed was used. Instead the rotation speed was increased until the spindle rotated smoothly. Next, the first source to be deposited was heated up.

For inorganic sources, starting from ambient the target temperature was increased in 10 to 20 °C increments. For the FAI source, the target temperature was always set only a few degrees above the current temperature. When approaching the evaporation temperature, the temperature ramping was slowed to prevent overshoot. Once the target temperature was reached, the source shutter was opened, and the deposition rate measured.

If the deposition rate was lower than desired, the temperature was increased in two to three degree increments. Once the target deposition rate was reached, the substrate shutter was opened. During the deposition, the rate was continually monitored, and the temperature was adjusted if necessary. Once the target thickness was reached, the substrate and source shutters were closed. The source heater was turned off. Once the deposition rate reached zero, the next source was heated up, and the process was repeated.

3.1.5. Deposition Parameters

Table 3.1: Starting and final deposition temperatures required for the target deposition rate of each component.

Compound	Starting Deposition Temperature (°C)	Final Deposition Temperature (°C)	Deposition Rate Å/s
$PbSnI_4$	210-220	245-255	0.50
FAI	125-150	135-170	0.30
CsI	355-370	365-375	0.15

3.1.6. Determining Tooling Factors

Due to the difference in positioning between the QCM and the substrate (and other parameters such as sticking factor, deposition cone shape, vapour pressure), there is a discrepancy between the measured deposited thickness and the actual deposited thickness. To estimate the ratio between the measured and actual deposited thickness (the tooling factor), a singular layer of a precursor was deposited at a

measured thickness of 250 nm. Next, the actual thickness was determined using profilometry. Now, the tooling factor was determined as:

$$ToolingFactor = \frac{d_{actual}}{d_{sensor}} \tag{3.1}$$

Where d_{actual} is the thickness as measured using the profilometer, and d_{sensor} is the thickness as measured by the QCM. The resultant tooling factors are shown in table 3.2.

Table 3.2: The tooling factor describing the difference between measured thickness (QCM) and actual thickness (profilometry). * FAI tooling factor was not directly determined, instead it was based on layer recipes from Pb-based PVK materials.

Compound	Tooling Factor
$PbSnI_4$	0.78 ± 0.11
FAI	0.48*
CsI	0.72 ± 0.11

3.1.7. Layer Recipes

Table 3.3: The layer recipes of the different PVK compositions

Composition	PbSnI4 (QCM Thickness, nm)	FAI (QCM Thickness, nm)	CsI (QCM Thickness, nm)
$FAPb_{0.5}Sn_{0.5}I_3$	162.5	272.1	0
$Cs_{0.05}FA_{0.95}Pb_{0.5}Sn_{0.5}I_3$	162.5	258.5	5.5
$Cs_{0.25}FA_{0.75}Pb_{0.5}Sn_{0.5}I_3$	162.5	194.2	31.5
$Cs_{0.40}FA_{0.60}Pb_{0.5}Sn_{0.5}I_3$	162.5	151.31	54.8

Initially, the layer recipes were determined based on the tooling factors. It was assumed that the tooling factor was independent of the layer that was deposited before. The target thickness was 200 nm. Using XRD, it was determined that this resulted in an accurate A-site to B-site ratio. However, according to EDS, the ratio of the A-site cations in the organic-inorganic perovskites was incorrect. Based on ratio measured in the EDS, the deposited thickness was adjusted. The final layer recipes are shown in table 3.3.

3.1.8. Thermal Annealing (for PVK films)

Higher annealing temperatures generally lead to improved morphology, as the increased diffusion enables the formation of larger grains and promotes crystallization.[116, 117] However, in organic MHPs produced via spin coating, the organic A-site components (MA^+ or FA^+) start to decompose at temperatures above 150 °C, in turn causing a sharp decline in optoelectronic performance.[116, 118–120] Additionally, annealing temperatures above 130 °C are observed to induce excess strain and cracks in FA^+-rich MHPs produced via spin coating.[117]

However, in organic Pb MHPs produced via STE, the reported optimal annealing temperatures (>170 °C) are significantly higher.[25, 72] The difference in required annealing temperature is ascribed to the poor reaction depth of STE,[25] however it remains unclear why the organic component is less susceptible to decomposition in MHPs produced via STE. The optimal annealing temperature for Sn/Pb organic MHPs produced via STE has yet to be described in literature. Based on the significant difference in annealing temperature in Pb-based perovskites between deposition methods, additional investigation is warranted.

Based on this research, it was chosen to produce an annealing trend for $FAPb_{0.5}Sn_{0.5}I_3$ and $Cs_{0.05}FA_{0.95}Pb_{0.5}Sn_{0.5}I_3$ from 120 to 200 °C, at increments of 20 °C. To anneal the films, a hot plate inside the glovebox was heated to the desired temperature, and allowed to stabilize (approx. 30 - 60 min). After reaching the desired temperature, the coated substrates were placed on the hot plate, and a timer was started for 10 minutes. After the sample was retrieved, the temperature was increased by 20 °C, allowed to stabilize for 10-20 minutes, before the next sample was placed on the hot plate for 10 minutes. This was repeated until all samples were annealed.

3.2. Characterization Techniques

3.2.1. X-ray diffraction crystallography (XRD)

X-ray diffraction crystallography is used to determine the atomic and molecular structure of a crystal. It relies on the principles of wave interference, where X-rays are scattered by the periodic arrangement of atoms in a crystal lattice. The resulting diffraction pattern can be analyzed to reveal information about the spatial distribution of electrons within the crystal, providing insight into its structure.

WORKING PRINCIPLE

The equation fundamental to X-ray diffraction is Bragg's Law, which relates the angle of incidence (θ) of X-rays on a crystal lattice to the wavelength of the X-rays (λ) and the spacing between crystal planes (d):

$$2dsin(\theta) = n\lambda \tag{3.2}$$

Where n is an integer, representing the n-th harmonic of that wavelength. Bragg diffraction in a crystal lattice occurs when plane waves strike the lattice at an angle θ. These waves are partially reflected by parallel crystal planes separated by a distance d. Constructive interference occurs if Bragg's law is met, which translate to a measured increase in intensity.

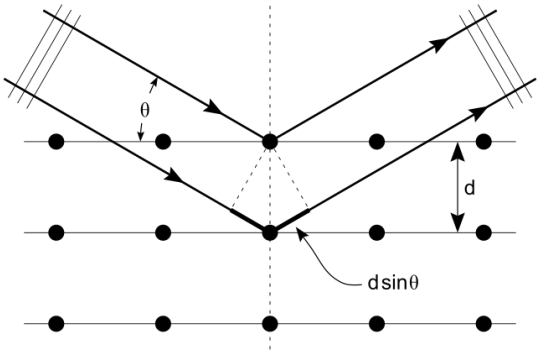

Figure 3.2: When polarized parallel X-rays hit a crystal lattice, the power of the reflected X-rays changes due to interference depending on the angle of the incoming wave (θ) as well as the distance between planes (d) according to Bragg's law (Eq. 3.2).[121]

DATA INTERPRETATION

The sensitivity of XRD is dependent on the repetition of crystal planes. The presence of a well ordered crystalline phase is revealed by sharp diffraction peaks, while the absence or presence of an amorphous phase is indicated by broad peaks or noise. Highly ordered crystalline domains give rise to more distinct peaks. Crystal structures may exhibit preferred orientation, where certain crystallographic planes are more common. This preferential alignment results in intensity variations among diffraction peaks corresponding to the different refraction planes. The width of diffraction peaks in an XRD pattern is related to the size of the crystalline domains (grains) within the sample. Smaller grains result in broader diffraction peaks due to the increased number of crystallographic defects at the grain boundaries. However, the broadening of the diffraction peaks stems not only from defects on the surface crystal, but also from crystal defects within the grains and instrumental broadening. The positions of diffraction peaks in an XRD pattern can be used to determine the lattice parameters of the crystal structure using Bragg's law. A shift in peak position can indicate lattice expansion, contraction or distortion. In addition, strain causes shifts in the positions of diffraction peaks, known as peak broadening or peak asymmetry.[122]

PROCEDURE

The to-be-measured thin films were placed on top of a sample holder with a glass substrate, and levelled by eye. XRD measurements were performed in ambient air using a Bruker D8 Advance diffractometer with a Cu X-ray source. During this research all spectra were collected in the Bragg-Brentano geometry. Diffraction data was obtained at 2θ angles ranging from 5 to 70 degrees. The produced data was not corrected for Kα2 or noise.

3.2.2. UV-Vis-NIR spectroscopy

UV-Vis-NIR spectroscopy is a characterization technique that is used to measure the intensity of transmitted, reflected and absorbed light. UV-Vis-NIR data can give valuable insight into the electronic structure, chemical composition, and helps to determine the maximum attainable PCE of the PVK.

INTEGRATING SPHERE

The presence of considerable reflection, scattering and interference in PVK samples can significantly influence the accuracy of the measurement. In this case, a special sample stage is used in conjunction with the conventional UV-Vis-NIR setup.[123] This sample stage, called an integrating sphere, consist of a spherical cavity whose inner walls are coated in a highly diffuse material, often magnesium oxide or barium sulfate. The detectors are positioned within the walls of the integrating sphere. By placing the sample in front of, and inside the integrating sphere, it is possible to take into account the scattering and reflective effects. The transmitted intensity is measured by placing the sample at the entrance of the integrating sphere, while the absorbance data is obtained by placing the sample inside of the integrating sphere.[123]

DATA INTERPRETATION

The relation between absorbance and transmittance is given by the Lambert-Beer law:

$$A = \frac{I_A}{I_0} = log(\frac{I_0}{I_T}) = log(T) \tag{3.3}$$

Where A is the absorbance, I_A and I_T are the intensity of absorbed and transmitted light, I_0 is the intensity of the incoming light, and T is the transmittance. Using the following relation, the absorbance (A) can be calculated from the transmittance and reflectance data.

$$A = 1 - (\frac{I_T}{I_0} + \frac{I_R}{I_0}) = 1 - (T + R) \tag{3.4}$$

In addition, this formula can be applied to separate the transmissive and reflective terms.

The absorption data can be used to estimate the band gap energy of a semiconductor material. The absorption onset, often given in wavelength, can be translated to a band gap energy using the following relationship:

$$E_g = \frac{hc}{\lambda} \tag{3.5}$$

Where E_g is the (band gap) energy, h is the Planck constant, c is the speed of light in vacuum, and λ is the wavelength.

Although the absorption onset allows for a rough estimation of the band gap energy, a Tauc plot is required for a more accurate determination. A Tauc plot shows the relationship between photon energy ($h\nu$) and $(\alpha h\nu)^{\frac{1}{n}}$, where α is the absorption coefficient, h the Planck constant, ν the photon frequency, and n a constant dependent on the electronic band structure. As most PVK materials possess a direct band gap, an n of 0.5 is assumed. The absorption coefficient α can be calculated using the following formula:[124]

$$\alpha = -\frac{1}{d} ln(\frac{T}{(1-R)^2}) \tag{3.6}$$

Where d is the thickness of the sample, T is the transmittance and R is the reflectance. The slope of the Tauc plot can be fitted to calculate the intersection with the $h\nu$ axis, which corresponds to the band gap energy (E_g) according to the following formula:[125]

$$(\alpha h\nu)^2 = A^2 h\nu - A^2 E_g \tag{3.7}$$

PROCEDURE

The PVK thin films were measured under ambient air conditions using a PerkinElmer UV/VIS/NIR Lambda 1050S spectrometer equipped with a 150mm Spectralon integrating sphere. In the near infrared (NIR) range, detection was performed using a InGaAs sensor, while a PMT sensor was used

for the ultraviolet-visible (UV-VIS) range. The Lambda 1050S spectrometer features Deuterium and Tungsten Halogen light sources. Measurements of the perovskite thin films were conducted within the wavelength range of 400 to 1100 nm.

For measuring the sum of the reflectance and transmittance, the samples were measured inside the integrating sphere, while the transmittance was measured in front of the integrating sphere.

3.2.3. Time-Resolved Microwave Conductivity (TRMC)

Time-resolved microwave conductivity (TRMC) is a method that uses a pulsed laser to photoexcite carriers in a semiconductor, causing a temporary change in conductivity. The alteration in conductivity is then measured over time using microwaves. TRMC provides a detailed examination of carrier lifetimes, mobility, and recombination dynamics with precise temporal resolution, all without the need for electrical contacts or transport layers.

WORKING PRINCIPLE

When a material undergoes photoexcitation, mobile charge carriers are produced. The increase in free charge carriers results in an enhancement of the material's conductivity. The electrical conductivity σ, by definition, is proportionate to the concentrations of free electrons (n_e), free holes (n_h), and their mobilities (μ_e and μ_h) as noted in Equation 3.8.

$$\sigma = e(\mu_e n_e + \mu_h n_h) \tag{3.8}$$

The TRMC technique involves studying the change in conductivity ($\Delta\sigma$) between the dark and illuminated states. Subsequently, the photo-conductance (ΔG) can be determined, a concept that will be elaborated upon later in this chapter. ΔG is directly proportional to the product of the overall number of photo-induced free charges and their mobility, as indicated in Equation 3.9. The microwave power (P) on the detector is diminished due to the absorption of microwaves by photo-induced charges. The normalized reduction in microwave power ($\frac{\Delta P}{P}$) is connected to ΔG by:

$$\frac{\Delta P}{P} = -K\Delta G \tag{3.9}$$

Here, K represents a sensitivity factor, and it is important to note that ΔP is negative, while ΔG is positive. ΔP is recorded over time following the laser pulse, enabling the TRMC technique to ascertain both the mobility and time-dependent concentration (i.e., the lifetime) of photo-induced free charges. Since both electrons and holes contribute to the photoconductance, ΔG is proportionate to the sum of their concentrations and mobilities.

The sensitivity factor K contains parameters such as the dimensions of the microwave cell, the dielectric properties of the materials present in the cell as well as the applied microwave frequency. K can be determined experimentally by comparing the reflected microwave power of a cell loaded with a bare substrate to a cell loaded with a substrate with a known conductivity. Using the following formula:

$$\frac{\Delta P}{P} = -K\Delta\sigma\beta L \tag{3.10}$$

The normalized change in reflected microwave power ($\frac{\Delta P}{P}$) is equal to the change in conductivity ($\Delta\sigma$) between the two measured substrates. As β (inner dimensions of the cell) and L (sample thickness) are known physical parameters of the cell and substrate, K can be calculated. It is important to note that the calculated parameter K is specific to the combination of cell, sample, substrate and microwave frequency.

MEASUREMENT SETUP

A magnetron is used to produce microwaves with the desired wavelength (figure 3.3 **a.**). Next, these microwaves are guided towards a circulator, which both reflects the incoming waves into the measurement cell and the outgoing waves into the microwave detector. The power of the reflected microwaves is then measured using a microwave detector and amplified using a broadband amplifier to filter out

extraneous frequencies. To aid in the propagation of the microwaves, the walls of the waveguides are coated in gold. The wavelength of the laser pulse can be set between 240 nm and 2400 nm with a FWHM of 3-5 ns.[126] There are two cell types that can be used in TRMC: a (resonant) cavity cell or

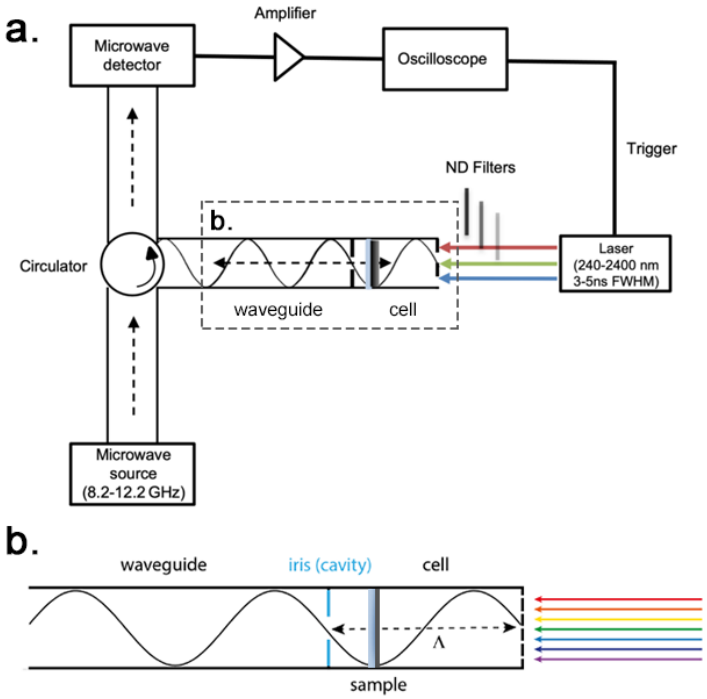

Figure 3.3: a. A diagram of the main components in the TRMC device setup.[126] **b.** A magnified version of the microwave (cavity) cell containing the sample positioned at 1/4 of the standing wave wavelength.[124]

an open cell. A cavity cell, shown in figure figure 3.3 **b.**, has a small opening which limits the frequency of the incoming microwaves. When the correct frequency is applied to a cavity cell, a standing wave is formed. The sample is placed at 1/4 of the length of the cavity, which corresponds to the maximum amplitude of the electric field. Cavity cell measurements offer higher sensitivity at the cost of a slower transient response (18 ns cavity vs 2 ns open cell) when compared to open cell measurements.[124, 126]

For both the open cell and the cavity cell, one side of the cell is covered with metal grating. This grating reflects microwaves while being largely transparent (>80%) to the incoming laser pulses. The metal grating is covered with quartz to reflect microwaves while being transparent to visible light. The microwave side is sealed with a film to provide an airtight environment inside of the cell. The walls of the cell are made of brass coated with gold.

PROCEDURE

Note that only the procedure for a cavity cell measurement will be discussed, as open cell measurements were not performed during this project. First, the applied microwave frequency is varied from 8.2 GHz to 12.2 GHz under dark conditions. The measurement is corrected for losses in microwave power due to the waveguide by dividing the sample measurement by a measurement performed on a reflective backplate. The resultant graph shows the normalized microwave power vs. the microwave frequency (figure 3.4 **a.**). Minima in microwave power indicate the formation of a standing wave in the cavity at that frequency. The lowest frequency microwave power minimum is the fundamental frequency (f_0) (figure 3.4 **b.**). At this frequency, the electric field is maximized at the position of the sample, i.e. a standing wave has formed inside the measurement cell cavity. The height of the fundamental frequency (R_0) is related to the dark conductivity of the sample.[127] A smaller R_0 is related to a larger microwave power loss, which corresponds to a greater dark conductivity (eq. 3.10). A bare quartz substrate has an R_0 value of 0.65 to 0.8.[127]

For the time resolved measurement, the frequency of the microwaves is fixed at the fundamen-

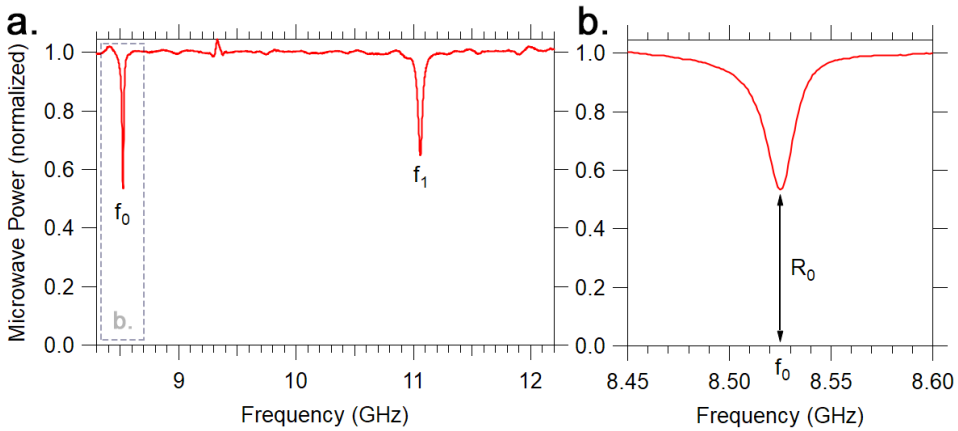

Figure 3.4: **a.** SSMC plot showing the fundamental resonance frequency (f_0) at 8.5 GHz and the first overtone (f_1) at 11 GHz. **b.** The

tal frequency for the highest sensitivity. The photon energy of the laser should be slightly larger than the band gap to guarantee adequate adsorption. Photon energy far above the band gap energy will result in excess heating due to thermalization losses which can impact cell performance and longevity. In this research, the excitation wavelength was set to 800 nm for all measurements. The maximum laser power at this wavelength was measured, this is later used to calculate the incoming light intensity I_0.

The first measurement is performed at the lowest possible laser intensity. Next, the optical density (OD) of the filter array was reduced until a perturbation became visible in the oscilloscope. Then, 300 measurements are performed and averaged to produce one TRMC trace. For each subsequent measurement, the optical density (OD) of the neutral density filters was decreased by 0.5. The traces are normalized for the fraction of absorbed light and the K-factor (equation 3.9) was adjusted to 66,000 based on previous work.[127]

DATA INTERPRETATION

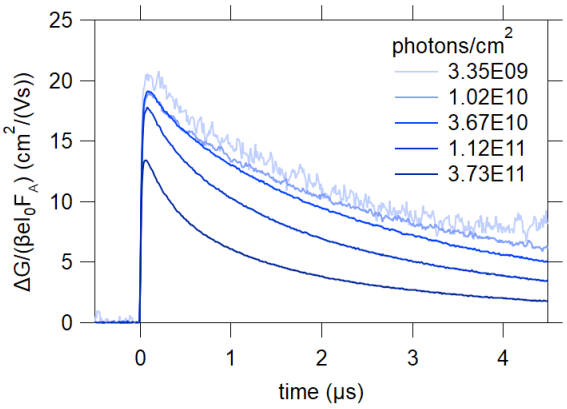

Figure 3.5: An example of a TRMC plot. At t=20-80 ns, the standing resonant wave forms inside the cavity. Over time, the free charges recombine, resulting in a decay in conductance. The traces show a regression in conductance and increased recombination with an increase in photon density (top right), signifying increased higher-order recombination.

An example of a series of TRMC traces is provided in figure 3.5. The y-axis of the plot shows the photoconductance (ΔG) divided by the product of the inner cell dimensions (β), the elementary charge (e), the intensity of the incoming light (I_0), and the fraction of absorbed light (F_A). This can be translated to the yield (ϕ) mobility (μ) product via equation 3.11.

$$\frac{\Delta G}{\beta e I_0 F_A} = \frac{L}{F_A I_0}\frac{\Delta G}{e\beta L} = \frac{Ln}{F_A I_0}\frac{\Delta \sigma}{en} = \phi\Sigma\mu \tag{3.11}$$

Here L is the film thickness, n is the number of free holes and electrons. $\Sigma\mu$ is the sum of the electron (μ_e) and hole mobility (μ_h), i.e. the total charge carrier mobility. ϕ describes the fraction of absorbed photons ($F_A I_0/L$) which yield free charges (n). Due to the low exciton binding energy of PVK materials, this value is assumed to approach unity at room temperature.[124] By expressing the y-axis in $\phi\Sigma\mu$, the TRMC data can be compared between samples with different thicknesses, compositions, and absorption coefficients. In addition, the maximum $\phi\Sigma\mu$ of a trace (t=20-80 ns) can be used to compare the charge carrier mobility in samples with similar decay kinetics. However, when the recombination rate is very high, the decay occurring during the system response (20-80 ns) is so significant that it severely limits the observed $\phi\Sigma\mu$ value (figure 3.6).

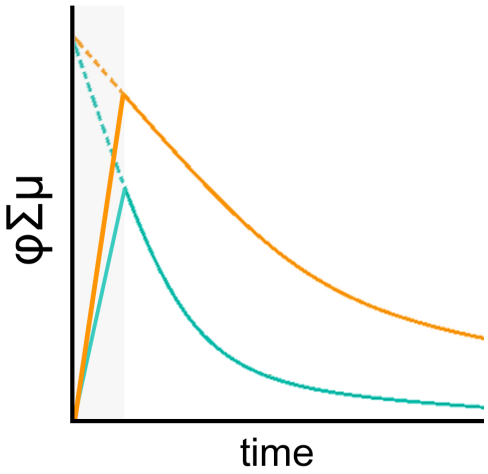

Figure 3.6: Higher-order decay can lead to lower observed $\phi\Sigma\mu$, even when the initial concentration and mobility of the charge carriers is identical, as the recombination occurring during response time (gray area) is increased.

The decay time and shape give insight into charge carrier lifetimes and recombination mechanisms. First-order decay, observed in the traces corresponding to the lower three fluencies in figure 3.5, typically emerges in materials with low carrier concentrations or when recombination predominantly occurs at localized defects or traps within the material. It reflects the scenario where recombination is mainly influenced by the concentrations of one species of charge carrier. In contrast, second-order behavior is more prevalent in materials with high carrier concentrations (trace corresponding to the highest fluency in figure 3.5), where recombination involves two carriers of opposite charge coming into close proximity. This behavior is characterized by the recombination rate being proportional to the product of carrier concentrations, indicating a dependency on the frequency of opposite charge carrier encounters. The shift from first-order to higher order at higher fluencies is the primary cause for the lowered photoconductance peak at higher photons densities (figure 3.6).[124, 126] Where possible, similar fluencies were used for comparison between different samples to minimize differences in carrier dynamics caused by charge carrier concentration.

The decay can show quasi-asymptotic behaviour at longer timescales, where the photoconductance stabilizes. This decay pattern is called a tail and can indicate an imbalance in positive and negative charge carriers, often caused by trapping or doping behaviour.

3.2.4. Stylus profilometer

Stylus profilometry is a characterization technique that allows to measure the topography and thickness of a sample.

WORKING PRINCIPLE

The stylus, often fabricated from diamond or other hard materials, is traversed across the sample's surface. As the stylus moves, it encounters variations in surface height, reflecting the topography of the sample. This displacement is measured and recorded, enabling the reconstruction of the surface profile. By analyzing the stylus displacement data, parameters such as step heights, surface roughness and morphology can be quantitatively assessed.

PROCEDURE

In preparation of thickness analysis, multiple scratches were placed across the width of the samples. Next, the depth profile was measured perpendicular to the scratches using a Bruker Dektak 8 Stylus profilometer. Both measurement and sample preparation was performed in ambient air.

The thickness was determined from the depth profile by calculating the difference between the height of the plateau and the average of the two valleys surrounding the plateau.

3.2.5. Scanning Electron Microscope (SEM) & Energy Dispersive X-ray Spectroscopy (EDS)

SEM operates by scanning a focused high-energy electron beam across the surface of a sample within a vacuum chamber. As the electron beam interacts with the sample, it emits electrons and photons which convey information about the sample's surface morphology and composition.

WORKING PRINCIPLE

Upon interaction with the sample, a high energy electron experiences both elastic and inelastic scattering. Elastic scattering occurs when the beam collides with atomic nuclei, while inelastic scattering happens when it interacts with atomic electrons. Typically, these interactions result in deflections further into the material, causing the beam to both widen and progress deeper into the sample.

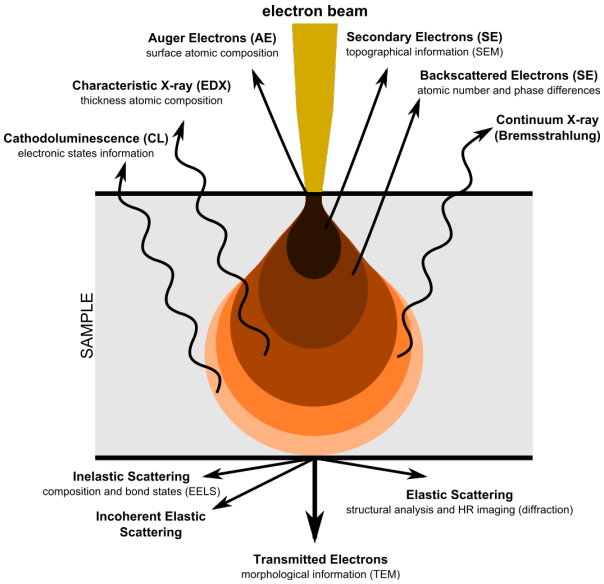

Figure 3.7: A cross-sectional view of the interaction volume of the electron beam[128]

Secondary electrons (SEs) are generated through inelastic interactions between the electron beam and weakly bound outer atomic electrons. Due to the relatively weak bonding energy, only a small portion of the primary electron's energy is used to detach the SEs from the atom. The remaining energy, in the order of around 100 eV, gets transferred in the form of kinetic energy. These electrons have a limited travel distance of 1-2 nm within the material, so only those produced near the surface can escape the material. The yield of secondary electrons is strongly influenced by the angle of the incident electron beam relative to the sample surface. More SEs are generated at the edges of surface features, resulting in a brighter signal. Due to this phenomenon, SEs are able to provide information on the morphology and grain structure of the film.[129]

Backscattered electrons (BSEs) are generated through elastic interactions between the electron beam and the atomic nuclei contained in the sample. Elastic backscattering creates electrons that escape at high angles (around 180°) with energies in the same order of magnitude as the energy of the electron beam. Due to the elastic nature of the interaction, the high-angle of diffraction and their high energy, BSEs can be detected from much deeper into the material compared to SEs (10-100 nm

vs 1-2 nm). Heavier elements possess bigger nuclei with a more positive charge, leading to stronger scattering. This allows for the differentiation of atoms based on the signal strength.[129]

ENERGY DISPERSIVE X-RAY SPECTROSCOPY (EDS)

As stated before, inelastic collision with inner-orbital electrons can lead to vacancy formation. Relaxation of the outer-orbital electrons to this vacancy involves the release of energy, either in the form of an Auger electron or a high-energy photon. Due to the discrete nature of the electron transitions, the released photons possesss well-defined characteristic wavelengths dependent on the orbital structure of the material. The high energies and random direction of the produced X-ray photons (100-1000 eV) allow them to escape from deep within the material (1-2 μm). The characteristic X-ray patterns can be analyzed to reveal information on the atomic composition deep into the sample.[130]

PROCEDURE

Sample preparation for SEM was performed in ambient air. The thin films were attached to the sample stage of the SEM using carbon tape. An additional strip of carbon tape was attached on top of the film to aid in charge removal.

SEM images were collected using the JEOL JSM-IT700HR microscope in secondary electron mode (SED). Beam settings were set at 5 kV, 30 pA probe current and 10 mm working distance. Images were taken at magnifications of x5,000 to x40,000.

ImageJ was used to determine the average grain size and the grain size distribution. Approximately 100 measurements were collected at a magnification of 10,000x. The diameter was always measured across the longest side.

For EDS, the beam acceleration voltage was set to 15 kV and probe current was increased to 55 pA. EDS point measurements were performed on the material buildup created by the scratches.

3.2.6. X-ray Photoelectron Spectroscopy (XPS)

X-ray Photoelectron Spectroscopy (XPS) is an analytical technique used to determine the elemental composition and the chemical state of a material surface (<100 Å). XPS offers the advantage of detecting all elements, except hydrogen and helium, down to concentrations of 1%.

WORKING PRINCIPLE

Soft X-rays (<6 keV) are used to irradiate a sample, leading to the ejection of photoelectrons from the inner electron shells of atoms. Depending on the binding energy of the electron, the kinetic energy of the ejected electron will change in accordance with the conservation of energy show in the equation:

$$E_{photon} = E_{binding} + E_{kinetic} + \phi_{spec.} \tag{3.12}$$

Here $E_{kinetic}$ is the kinetic energy of the ejected electron (as detected), E_{photon} is the photon energy of the X-rays, $E_{binding}$ is the binding energy of the ejected electron vs the chemical potential, $\phi_{spec.}$ is the work function of the spectrometer.[131]

The binding energy is dependent on the energy level of the shell from which the electron was excited, which is unique for each material and changes with chemical environment. This allows for the precise identification of the elements within the measured material and their bonds.

To result in accurate detection, the electrons must escape the material while suffering minimal energy losses. Although X-rays are able to penetrate most materials in the order of micrometers, the produced electrons quickly lose their energy via inelastic collisions inside the material, leading to a limited depth sensitivity of around 10 nm. The lower energy electrons which have undergone inelastic collisions are occasionally able to escape the material, these are observed as the characteristic sloped background observed in XPS plots.

To give insight into the composition deeper into the sample, and ion gun can be used to etch into the material. This way, depth profiles can be attained.

DATA INTERPRETATION

XPS plots consist of a series of distinct peaks, corresponding to the characteristic electrons, accompanied by elongated tails, indicating electrons that have lost energy during their outward path. An example XPS plot can be found in figure 3.8. Note that the convention is to plot XPS plots from high to low binding energies on the X-axis.

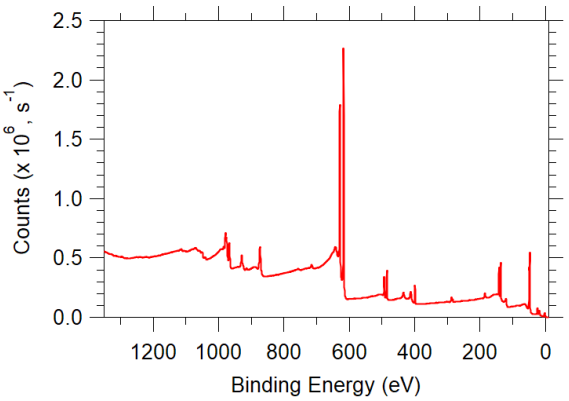

Figure 3.8: Example of an overview of an XPS spectrum, showing the characteristic peaks and elongated tails. N.B. the reversed x-axis.

Determining the elemental makeup generally involves cross-referencing the spectrum with existing data. A shift in characteristic peak position, called a chemical shift, can indicate a change in oxidation state, electronegativity, chemical milieu and lattice parameters. Different oxidation states of the same atom often show overlap in the characteristic peaks. To decompose these peaks into their constituent parts and allow for quantitative analysis, precise fitting is required.[131]

PROCEDURE

Samples were loaded into a vacuum transfer unit inside of a glovebox under N_2 atmosphere. XPS was measured using a Thermo Fisher Scientific K-Alpha X-ray Photoelectron Spectrometer (XPS) System

The hemispherical analyzer was operated at a constant analyzer energy (CAE) of 50.0. The bin size was set to 0.10 eV. Before scanning, the surface was removed using etching (except when examining depth profiles). Each scan was performed ten times.

4
RESULTS & DISCUSSION

4.1. $PbSnI_4$ alloy for Thermal Evaporation

As elaborated on in section 2.5.4, the $PbSnI_4$ alloy has the potential to reduce the complexity of the evaporation process by reducing the required number of sources. This research introduces a procedure for producing $PbSnI_4$, allowing for a faster and easier synthesis compared to the method described by Kuku et al.(1988).[112] In addition, a method was proposed to introduce excess SnF_2 into the $PbSnI_4$ alloy. The addition of excess SnF_2 was chosen to copy the procedures described in spin coating as closely as possible. Further discussion on SnF_2 in PVKs produced via STE can be found in section 4.4.

4.1.1. Structural Characterization

$PbSnI_4$ and $PbSnI_4$+SnF_2 where synthesized according to the protocol in section E. The synthesis resulted in a solid crimson-red ingot, which is shown in figure 4.1. Compared to the orange-yellow mixture of PbI_2 and SnI_2, the color has changed significantly.

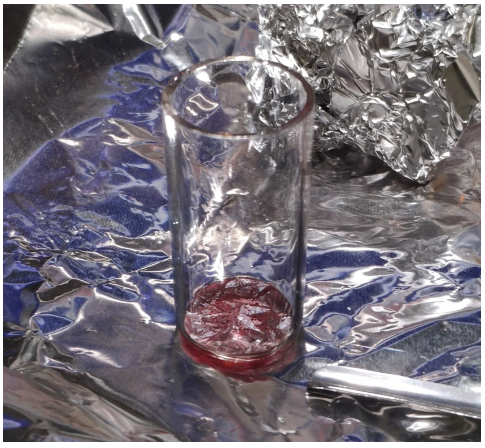

Figure 4.1: An ingot of $PbSnI_4$ contained in an evaporation crucible. Note the crimson-red appearance post-synthesis.

The produced $PbSnI_4$(+10% SnF_2) ingots were ground down to a fine powder and examined using powder XRD. The resultant patterns plus the reference pattern taken from Kuku et al.(1988)[112] can be found in figure 4.2 **a.** and **b.**.

All peaks described in the reference literature line up in both versions of the synthesized alloy powder. No excess SnI_2 or PbI_2 is observed, however the proximity between the peak angles of PbI_2 and $PbSnI_4$ makes it difficult to observe an excess PbI_2 phase. The lower intensity signal associated with a small fraction would cause the PbI_2 peak to be hidden by the tails of the higher intensity $PbSnI_4$ peak. The 300, 301, 311 and 400 peaks of the powder XRDs show a minor shift towards higher angles. Shifts in peak position can be caused by expansion or contraction of the lattice. $PbSnI_4$ is reported as

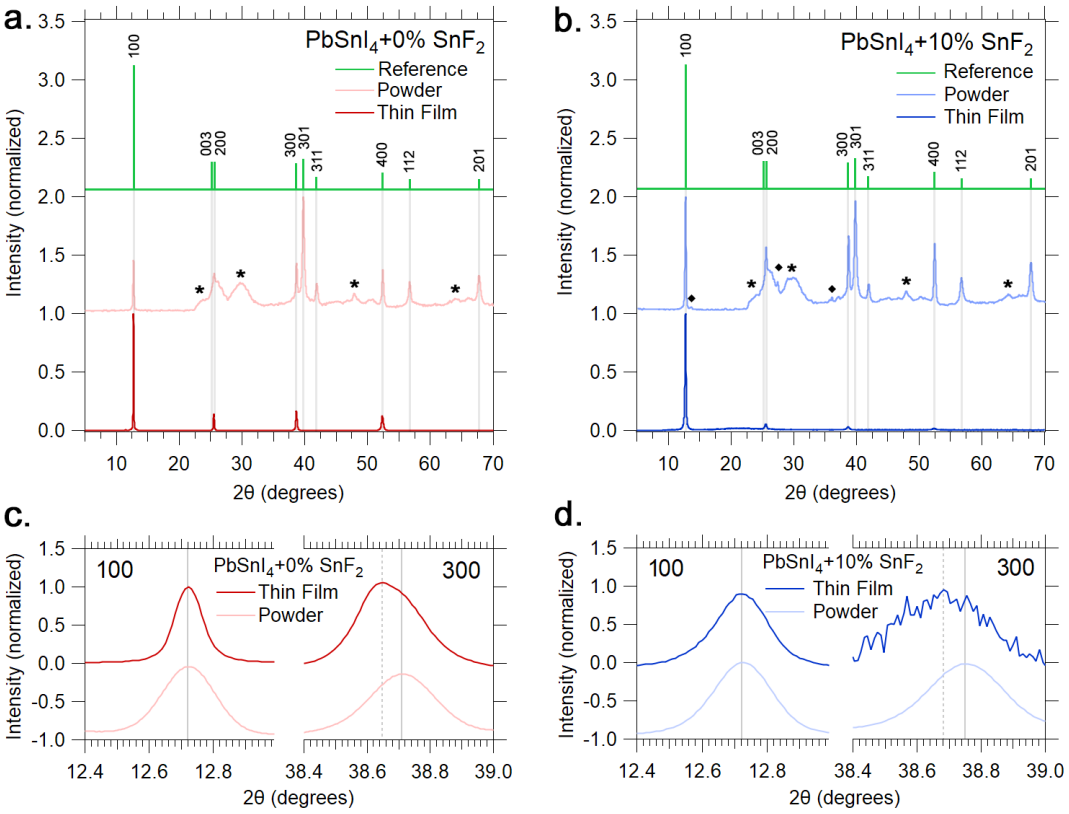

Figure 4.2: a. XRD of $PbSnI_4$ thin film (dark) and powder (light) and **b.** $PbSnI_4$+10 mol% SnF_2 thin film (dark) and powder (light) measured on a monocrystalline silicon substrate at ambient conditions. **c.** and **d.** show an enlarged view of the 100 and 300 peaks from the patterns shown in **a.** and **b.** ◆ corresponds to SnI_2, ∗ is suspected to correspond to various (surface) oxides. Reference peaks of $PbSnI_4$ (green) were reproduced from Kuku et al.(1988).[112]

having a tetragonal structure with a: 6.995 Å and c: 10.909 Å,[112] while the produced compound has lattice parameters of a: 7.00 Å and c: 9.65 Å. The 003 peak could not be observed in either alloy, likely due to overlap with the neighbouring 200 peak.

The peaks marked in figure 4.2 **a.** and **b.** with an asterisk (∗) or a diamond (◆) do not match with the spectrum reported in the reference. The peak marked with a diamond (◆) are associated with SnI_2, being only present in the $PbSnI_4$+10% SnF_2 powder. A possible explanation is that the SnF_2 powder replaces some of the SnI_2 in the $PbSnI_4$ alloy, resulting in an excess of SnI_2.

The broad peaks marked with an asterisk (∗) in figure 4.2 **a.** and **b.** are atypical in shape, making it difficult to accurately characterize. Considering that the measurements were performed in ambient air, potential matches for these peaks are PbI_2, PbO, Pb_2O_3, $Pb_{1.785}I_{3.570}$, SnO, $SnI_2.H_2O$ and I_2O_4. Additional research, found in Appendix A, to determine the exact nature of the peaks was inconclusive. The broad nature of the peaks indicates small domain size, which leads to the conclusion that the peaks marked with an asterisk (∗) are associated with various surface oxidation products. In the reference paper by Kuku et al.(1988), the material was stored in ambient air, yet the broad peaks ascribed to surface oxides in this research are not observed in the reference XRD spectrum.[112] A possible explanation lies in the reported instruments and the age of the source; the reference XRD spectrum was likely collected on photographic film and then manually digitized. This introduces a certain amount of subjectivity. The broads peaks may have been left out as they were assumed to be noise.

4.1.2. Thermal Evaporation

In section 3.1.2, it was determined that for application in the STE of narrow band gap Sn/Pb PVK absorber layers, $PbSnI_4$ should behave as a single material during evaporation. Solid solutions or mixtures are likely to result in dissimilar vapour pressures during evaporation or over a number of depositions. This would result in poor control over composition.

Table 4.1: Overview of the initial evaporation temperature for $PbSnI_4$ and its constituents. The initial evaporation temperature is defined as the temperature required for reaching 0.5 Å/s as measured by the QCM.

Compound	Evaporation Temperature, °C (vacuum, 0.5 Å/s QCM)
PbI_2	245
SnI_2	175
$PbSnI_4$	220
$PbSnI_4$+10% SnF_2	220

To test the created alloys for the above-mentioned criterion, the thermally evaporated $PbSnI_4$ and $PbSnI_4$+10% SnF_2 thin films were examined using evaporation temperature, EDS and XRD. The initial temperature required to a reach a deposition rate of 0.5 Å/s is shown for PbI_2, SnI_2 and $PbSnI_4$ in table 4.1. The evaporation temperature of $PbSnI_4$(+10% SnF_2) is distinct from that of pure PbI_2 and SnI_2, pointing towards the formation of a single material.

Table 4.2: Table showing the ratio of Sn:Pb in full PVK films deposited using the $PbSnI_4$ alloy measured using EDS in over deposition number. In total, 59 measurements were performed across 4 deposition.

EDS $PbSnI_4$	
Deposition #	Sn:Pb
3	1:1.04±0.20
4	1:1.02±0.12
5	1:1.01±0.14
6	1:1.08±0.21
Overall	1:1.04±0.17

Table 4.3: Table showing the ratio of Sn:Pb in full PVK films deposited using the $PbSnI_4$+10mol% SnF_2 alloy measured using EDS over deposition number. In total, 19 measurements were performed across 4 deposition.

EDS $PbSnI_4$+10%SnF_2	
Deposition #	Sn:Pb
2	1:0.98±0.01
3	1:0.97±0.20
4	1:0.96±0.19
5	1:0.95±0.10
Overall	1:0.97±0.16

To further compound this result, EDS data was gathered from the PVK films produced using the alloy, totalling 59 measurements across 4 different depositions for $PbSnI_4$ and 19 measurements across 4 different depositions for $PbSnI_4$+10% SnF_2(table 4.2 and 4.3). The average Pb:Sn ratio across all depositions was determined to be 1:1.04 for the $PbSnI_4$ alloy and 1:0.97 for the $PbSnI_4$+10% SnF_2 alloy. With standard deviations calculated at ±0.17 and ±0.10, respectively. The deviations from a 1:1 ratio were not statistically significant. Moreover, no statistically significant trend in composition over the deposition number was observed.

To further investigate whether $PbSnI_4$ is able to produce a stoichiometric thin film, the produced $PbSnI_4$ and $PbSnI_4$+10% SnF_2 thin films were examined using XRD. The resultant data can be found in figure 4.2 **a.** and **b.**, denoted by the dark red and blue traces. The signal-to-noise ratio of both thin films suggests that a crystalline film was successfully attained. In contrast to previous work from Kuku et al.(1999), no annealing after deposition was necessary to create a crystalline $PbSnI_4$ thin film.[113] The signal-to-noise ratio in the thin film containing SnF_2 (blue) is lower than the film containing no SnF_2 (red). This can either be caused by a difference in crystallinity or film thickness.

The presence of only the H00 reflections suggests that the deposited films show a strong preferential growth in the 100 direction. As elaborated in theory sections 2.5.1 and 2.5.2, nucleation and growth mechanisms of vacuum deposition methods are different from those in spin coating. In spin coating, rapid nucleation and crystallization occurs within the solution before deposition, resulting in a film containing disordered crystallites. As explained in section 2.5.2, nucleation is governed by substrate-vapour interactions in vacuum deposition methods such as STE. Even on amorphous substrates, when epitaxy is not possible, vacuum deposition often results in thin films with strong pref-

erentially orientated crystal structures due to the unfavourable substrate-vapour interactions.[100] The results presented in this research are in agreement with this theory

Figure 4.2 **c.** and **d.** show an enlarged version of the 100 and 300 peaks from the patterns shown in figure 4.2 **a.** and **b.**. All peaks are individually normalized. The 100 peaks were adjusted to a 2θ angle of 12.723 degrees, corresponding to a lattice parameter of 6.995 Å. Upon enlargement, a noticeable shift in the 300 peak position (relative to the 100 peak position) is observed from powder to thin film in both versions of the alloy. As explained in section 3.2.1, a shift towards lower degrees indicates an increase in lattice parameter.

Changes in crystal phase can lead to variations in lattice parameters. However, since the peak patterns remain identical, transitions to different crystal phases are deemed improbable. Substitution of smaller elements with larger ones, such as PbI_2 replacing SnI_2, can lead to lattice expansion. Due to the large error in the EDS data, a small deviation from a 1:1 PbI_2:SnI_2 ratio can not be definitively disproven. Stresses or defects in the crystal structure can also cause shifts in XRD patterns. As $PbSnI_4$ is deposited on quartz, lattice mismatch may distort the crystal structure and induce stress. Vacuum deposition of thin films is known to introduce stress.[132, 133]

Although this work is not able to definitively prove the stoichiometric evaporation of PbI_2 and SnI_2 using the $PbSnI_4$ alloy, the distinct evaporation temperature and compositional stability over many depositions point towards $PbSnI_4$ behaving as a single material during thermal deposition. The minor changes changes observed in the XRD patterns could either be cause by slight deviations in composition or material stress formed during deposition. The compositional stability is deemed sufficient for further application in the production of PVK thin films.

4.1.3. Summary

This study introduces a novel approach to synthesizing $PbSnI_4$, which reduces the number of required sources in Sn/Pb perovskite production via thermal evaporation. Powder X-ray diffraction (XRD) analysis confirms successful synthesis, albeit with slight variations in lattice parameters versus literature. XRD of thermally evaporated $PbSnI_4$ thin films show high crystallinity and strong preferential orientation, without the need for post-deposition annealing. Although stoichiometric deposition could not be definitively proven, the compositional stability and distinct evaporation temperature point towards $PbSnI_4$ forming a single material.

4.2. Annealing Temperature Optimization for $FAPb_{0.5}Sn_{0.5}I_3$ deposited via STE

Due to the lack of precedent, optimal annealing conditions for the STE of Sn/Pb PVK absorber layers have yet to be established. During this research, the impact of annealing temperatures ranging from 120°C to 200°C on $FAPb_{0.5}Sn_{0.5}I_3$ was investigated. All samples were annealed for 10 minutes. Apart from the performance improvement, this research can give valuable insight into the formation mechanism of Sn/Pb PVKs produced via STE.

4.2.1. Perovskite Phase Formation

Before the properties of the produced thin films can be assessed, successful PVK phase formation needs to be established. Before annealing, the produced films had a translucent brown appearance.

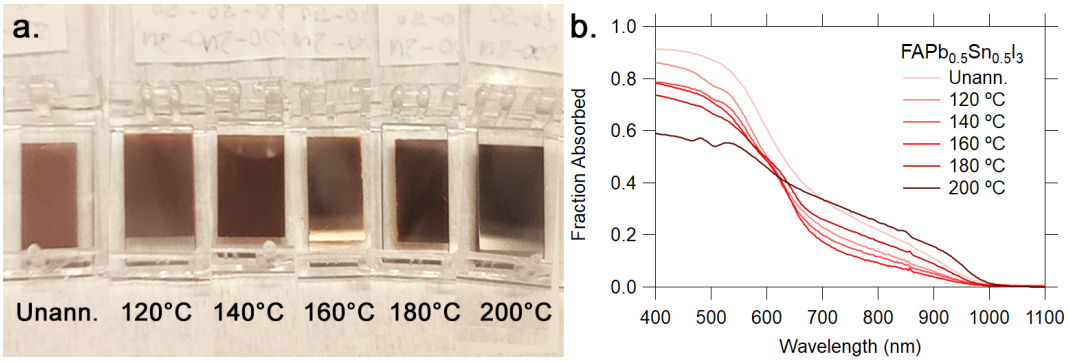

Figure 4.3: a. An image of the annealed thin films. From left to right, an unannealed sample and samples annealed at 120, 140, 160, 180 and 200 °C. **b.** The corresponding absorption spectrum is shown on the right. Note the increased opacity with increasing annealing temperature.

Upon annealing, the films darkened substantially, especially at higher temperatures (>180 °C), indicating an increase in photoactive phase (figure 4.3 **a.**). The change in opacity and color was quantified using absorption spectroscopy, resulting in the spectra presented in figure 4.3 **b.**.

Contrary to what is observed by naked eye, the absorbance decreases significantly when annealing the films at temperatures from 120 to 160 °C. At temperatures at or above 180 °C, the absorbance increases again. At 200 °C the absorbance is increased compared to the unannealed film at wavelengths above 700 nm. Interestingly, at 200 °C the absorbance is decreased significantly compared to all other annealing temperatures at wavelengths below 600 nm.

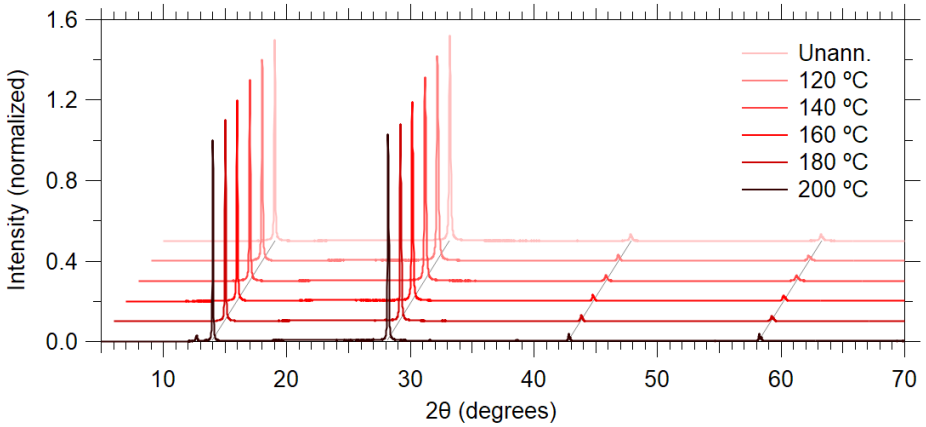

Figure 4.4: XRD patterns of the $FAPb_{0.5}Sn_{0.5}I_3$ annealing trend. Note the increase in $PbSnI_4$ phase at 200 °C and the presence of only the H00 orientations.

The normalized XRD patterns (figure 4.4) show distinct and high intensity peaks corresponding to the PVK phase. The signal-to-noise ratio (SNR) is high, indicating a highly crystalline material with a minimal amorphous phase. Similar to the $PbSnI_4$ layer shown in section 4.1, the produced films possess a strongly preferentially orientated crystal structures. As described in section 2.5.2, the first layer in STE is suspected to function as ”scaffolding” for the crystal structure of the PVK phase.[34]

Little to no excess precursor peaks ($PbSnI_4$, PbI_2, SnI_2) are present in the XRD patterns of the unannealed sample and the samples annealed from 120 to 160 °C. The film annealed at 200 °C shows a small $PbSnI_4$ peak at approximately 12.7 degrees. The absence of amorphous noise and peaks corresponding to precursors indicate that the correct composition was attained.

The XRD data demonstrates the successful formation of a highly crystalline PVK phase in all samples, including the unannealed film. This indicates that the formation of the PVK phase occurs during the thermal evaporation, and the precursors are not deposited as distinct layers. These results are in agreement with the theories presented in section 2.5.2. The appearance of a $PbSnI_4$ peak and the decrease in absorption at lower wavelengths in the sample annealed at 200 °C suggest decomposition of the PVK structure. Higher temperatures were not investigated, making it unclear whether decomposition is increased at temperatures above 200 °C.

4.2.2. Thermal Decomposition

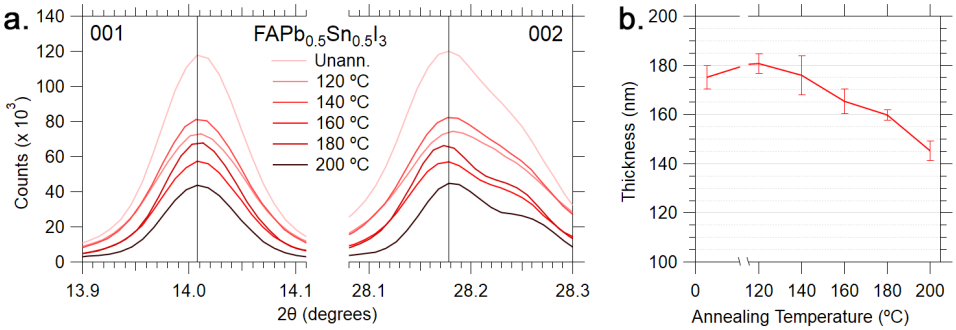

Figure 4.5: a. Magnified XRD patterns of the 001 and 002 peaks of $FAPb_{0.5}Sn_{0.5}I_3$ annealed at temperatures from 120-200 °C. The patterns were shifted to align the 001 peak. Note that the patterns were not normalized. **b.** Sample thickness as measured by stylus profilometry versus annealing temperature. The leftmost data point signifies the unannealed sample.

In figure 4.5 **a.**, the peak height of the samples annealed from 120 to 200 °C shows a downward trend with some variation. In XRD patterns, a decrease in peak height is generally caused by a decrease in crystalline volume. This means that either the total volume of the material has decreased, or the fraction of crystalline material (crystallinity) has decreased.

Profilometry confirms that the decreasing peak intensity observed in the XRD is caused by a loss in total volume (figure 4.5 **b.**). Increasing the annealing temperature leads to an increased loss in volume. As the decrease in thickness is large (approx. 30%), a likely explanation is material loss to thermal decomposition. At 200 °C the intensity of the $PbSnI_4$ phase increases significantly (figure 4.5 **b.**), this is a strong indicator of thermal decomposition.[134] However, no increase in the excess $PbSnI_4$ phase is observed in the XRD of the samples annealed from 120 to 180 °C. Here, increased compactness is the most likely explanation. Thermal annealing is known to increase film compactness, resulting in a decrease in volume without an increase in the precursor phase.

4.2.3. Effect on Optoelectronic Properties

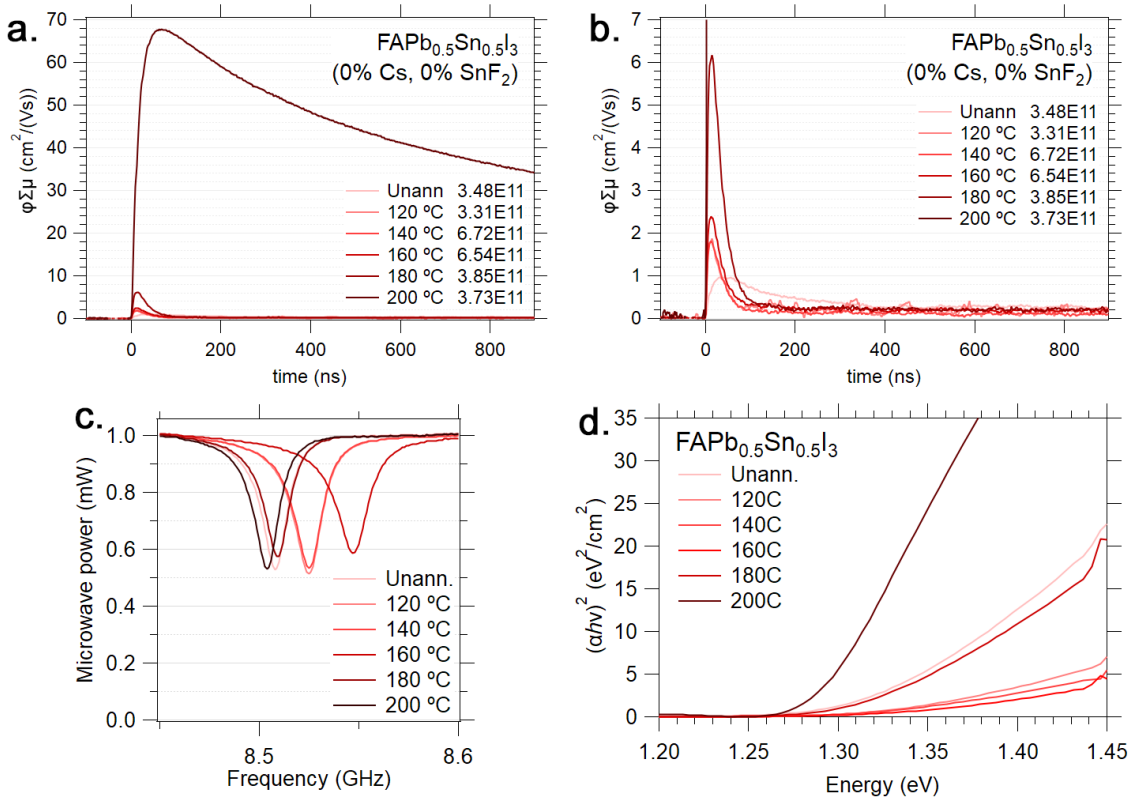

Figure 4.6: TRMC traces of $FAPb_{0.5}Sn_{0.5}I_3$ annealed at 120-200 °C. **b.** shows an enlarged version of **a.**. Both graphs were normalized for the fraction of absorbed light. To aid in comparison, similar fluencies were chosen where possible. **c.** SSMC of the samples annealed at different temperatures. The difference in x-position of the minima is a result of variation in substrate thickness. **d.** Tauc plot of the annealing trend, with on the x-axis $(\alpha h\nu)^2$ based on the assumption that most PVK materials possess a direct band gap.

TRMC was used as the primary method for assessing the performance at the different annealing temperatures. A comparison of the TRMC traces of the different annealing temperatures for $FAPb_{0.5}Sn_{0.5}I_3$ can be found in figure 4.6 **c.**. A large difference in TRMC response is observed between the sample annealed at 200 °C and all other samples. While the sample annealed at 200 °C demonstrates a high initial conductance and a slow decay, all other sample show incredibly fast recombination kinetics, resulting in a low maximum $\phi\Sigma\mu$.

SSMC measurements were performed for each annealing temperature to estimate the dark conductivity, the data can be found in figure 4.6. All R_0 values fall between 0.5 and 0.6, indicating a dark conductivity smaller than 4 μS. No correlation was observed between annealing temperature and R_0 value.

The Tauc plot, shown in figure 4.6 **d.**, shows a significant change in band structure with changing annealing temperature. All samples annealed at lower temperatures than 200 °C show a lack of linear regime within the expected energy range. Higher-order behaviour could indicate a non-direct band structure. The non-linear nature of the curves makes estimation of the band gap difficult.

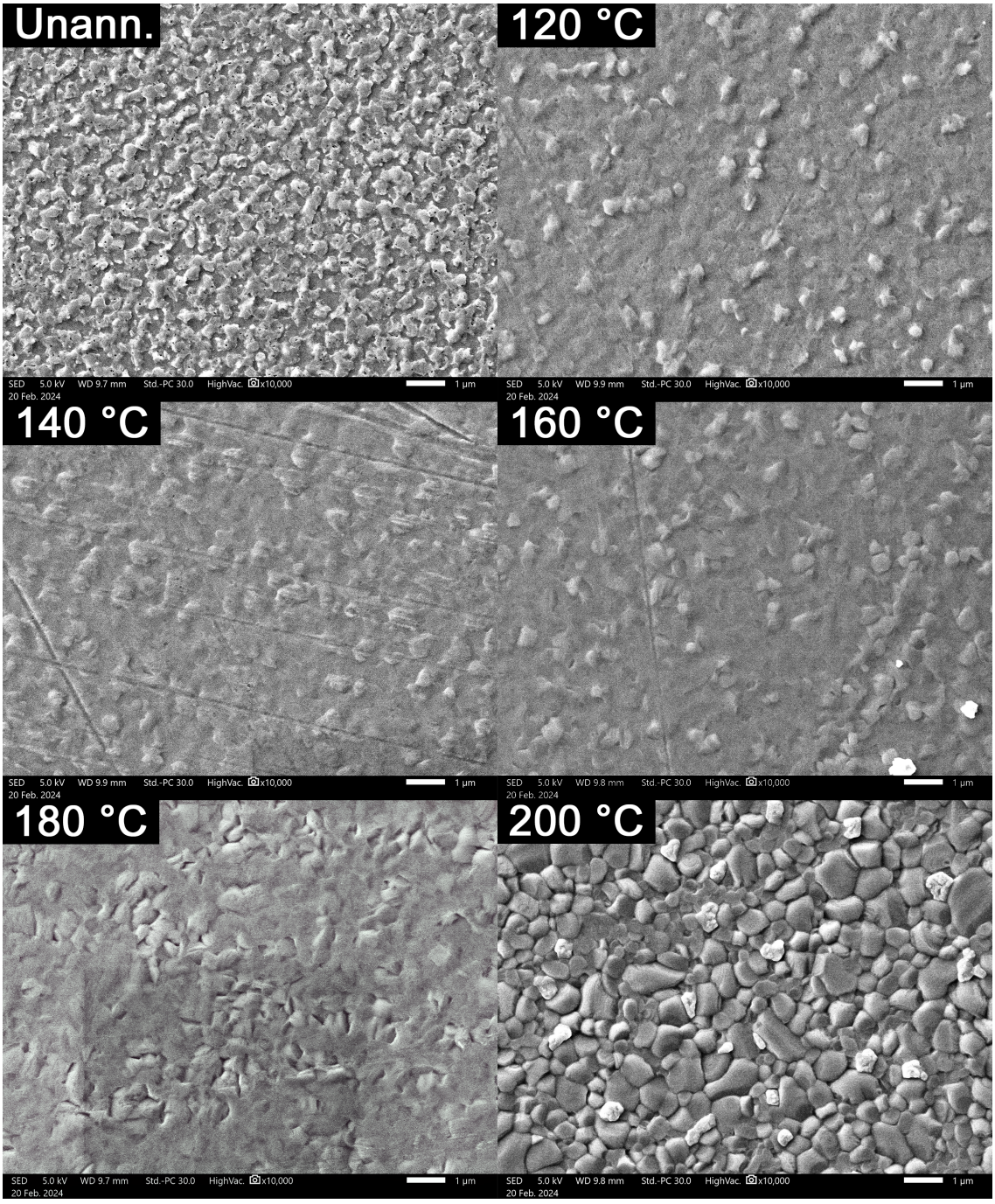

Figure 4.7: SEM images of $FAPb_{0.5}Sn_{0.5}I_3$ films annealed at different temperatures at a magnification of x10,000. The scratches visible in the 120, 140 and 160 °C samples are damage as a result of storage and transport. The sample annealed at 180 °C shows a darker area resulting from SEM images taken earlier.

4.2.4. Effect on Morphology

SEM was used to examine how grain size and morphology change with annealing temperature. A comparison between the samples is shown in figure 4.7. The unannealed sample presents with a disordered surface geometry. When the PVK film is annealed at 120 to 160 °C, the smoothness of the surface is increased, but no distinct grains are visible. From 160 to 180 °C, distinct grains start to form. A clear difference in morphology can be observed when comparing the samples annealed at 200 °C and all other samples. The samples that were annealed at 200 °C show a clearly defined grain, with grain sizes in the order of 1 μm.

4.2.5. Origin of the High Optimal Annealing Temperature

Although it can not be definitively concluded, based on the optoelectronic properties, the morphology, and the onset of decomposition observed in the XRD patterns, the optimal annealing temperature for the $FAPb_{0.5}Sn_{0.5}I_3$ PVK is determined as 200 °C.

The determined optimal annealing temperature differs significantly from values reported in literature based on spin coating. As stated in section 2.5.3, in studies on spin-coated organic-based Sn/Pb PVKs the prevailing annealing temperatures range around 100 °C.[44, 135–139] Above annealing temperatures of 150 °C, organic PVKs produced by spin coating tend to show rapid decomposition, resulting in poor optoelectronic performance and morphology.[118–120, 140, 141]

POOR INTERDIFFUSION

Although no reference on annealing temperature is available when it comes to organic Sn/Pb perovskites produced by STE, Pb-based perovskites are reported to have significantly higher optimal annealing temperatures (>170 °C) than their spin-coated counterparts.[25, 72] Based on research performed by Du et al.(2022), the need for higher annealing temperatures in STE deposited PVKs is an effect of the vapour-solid reaction mechanism explored in theory section 2.5.2.[25] Elevating the temperature and duration of in-situ or post-deposition annealing promotes interdiffusion and enhances reaction penetration depth according to Du et al..[25]

With poor reaction depth and interdiffusion, one would expect to see a poorly crystalline film, with a small PVK phase and a large precursor phase. At higher annealing temperatures, the interdiffusion would improve, and the precursor phase should decrease and the PVK phase should increase. The XRD patterns shown in figure 4.4 seems to directly contradict this claim however, as even in the unannealed sample a strong PVK phase is present with little to no visible precursor peaks. Furthermore, if interdiffusion is the primary constraint for PVK material formation, the focus shifts to understanding why electronic performance does not enhance with temperatures rising from 120 to 160 °C. The substantial difference between annealing temperatures of 180 and 200 °C raises questions about the unexpected size of the increase across 20 °C difference. One would anticipate a more consistent rise in TRMC signal with incremental increases in annealing temperatures.

COMPOSITIONAL CHANGES

Compositional changes can significantly influence the characteristics of a PVK material. Compositional changes caused by the thermal decomposition mentioned earlier could be an explanation for the sudden increase in optoelectronic performance from an annealing temperature of 180 to 200 °C.

Table 4.4: Table showing the ratio of Sn:Pb as measured by EDS versus annealing temperature. 3 to 6 measurements were performed per annealing temperatures. Due to the small sample size, the error could not be accurately calculated. The general error in EDS measurements is approximately 0.20.

Annealing T (C)	Ratio Sn:Pb
Unann.	1:1.00
120	1:1.09
140	1:1.40
160	1:1.07
180	1:0.95
200	1:1.05

The elemental ratios measured using EDS (tabel 4.4) suggest no significant change in overall composition with changing annealing temperature. However, the fraction in the crystalline phase can change without changing the overall composition.

More subtle changes in composition can be investigated using XRD. Even minor changes in composition are reflected in the lattice parameter of the PVK. Figure 4.5 **a.** shows a magnified version of the 001 and 002 peaks in figure 4.4. The angle between the 001 and 002 peaks stays constant (within error) across all annealing temperatures. This indicates that no lattice expansion or contraction has occurred. Considering the XRD and EDS data, changes in composition are deemed unlikely, and are thus ruled out as a potential cause for the high required annealing temperature.

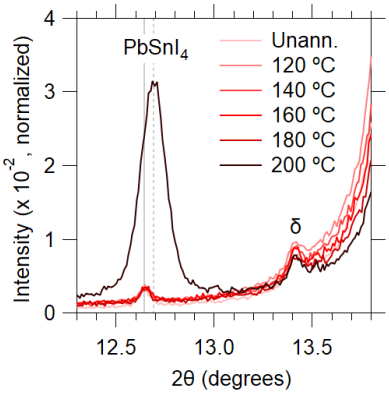

Figure 4.8: Magnified version of the XRD patterns shown in figure 4.4, showing the excess $PbSnI_4$ and the δ phase. Patterns were shifted to align the 001 peak.

NON-PHOTOACTIVE PHASES

A phase transition could be another explanation for the drastic increase in performance observed from 180 to 200 °C. As explained in sectionsection 2.2.1 and 2.5.3, non-photoactive phases can form, which can transition to photoactive alpha phases at elevated temperatures. Although the phases and their respective transition temperatures are poorly documented for Sn/Pb PVKs, in other PVK materials, alpha phase transitions above 180 °C are generally only observed in Cs-based PVKs.[116, 118–120]

The non-photoactive delta phase is marked with a δ in figure 4.8. No change in peak size is observed across any of the annealing temperatures. The non-photoactive gamma and beta phases were not observed in the XRD. Based on this, phase transitions are ruled out as a possible cause for the observed behaviour.

4.2.6. Recrystallization as the Underlying Mechanism

Considering all the gathered data, the following hypotheses on the mechanism responsible for the observed annealing behavior is put forward: After deposition, the PVK has formed a meta-stable system consisting of a crystalline phase with small grain size interspersed with amorphous material. The strongly preferred orientation results in a high count number and sharp peaks in the XRD patterns.

Annealing from 120 to 180 °C results in improved compactness, leading to small improvements in optoelectronic performance. It is unclear if the increased interdiffusion at these temperatures has any effect. At 200 °C, the thermal energy is high enough that the system can overcome the potential energy barrier of the meta-stable state and transition into a more crystalline and ordered stable state, i.e. recrystallization occurs. At the same time, the PVK structure starts to decompose. As to why the produced PVK material is able to withstand temperatures above 150 °C without decomposition is unclear.

4.2.7. Summary

Annealing temperatures ranging from 120°C to 200°C were investigated for $FAPb_{0.5}Sn_{0.5}I_3$. Using XRD, successful synthesis of the $FAPb_{0.5}Sn_{0.5}I_3$ PVK material via STE was established.

Based on optoelectronic performance, morphology, and decomposition, an annealing temperature of 200°C was determined to be the optimum within the chosen annealing range. However, it can not be definitively concluded, as 200 °C was the highest tried annealing temperature.

The drastic change in optoelectronic properties and morphology from 180 to 200 °C annealing temperature suggests a recrystallization mechanism at play. The change in morphology is assumed to be the major factor in the improved optoelectronic properties. This research underscores the contrasts with existing literature on annealing temperatures for (spin-coated) PVKs and highlights the unique behavior of STE-produced PVKs.

4.3. Additive-Free High-Performance Sn/Pb PVKs via STE

A significant conclusion can be drawn from the TRMC and SSMC data presented in the previous section: STE allows for the creation of high-performance and low-doping-density Sn/Pb PVKs, without any additives. In this section, these results will be discussed in more detail and compared to literature.

The ability to obtain near-intrinsic Sn/Pb PVKs without additives stands in stark contrast to results from spin-coated Sn/Pb perovskites (figure 4.9 **a.**). The majority of spin-coating-based research is focused on reducing doping densities through additive engineering. In spin-coated samples, R_0 values greater than 0.4 can only be achieved using additives such as SnF_2. The production of a quasi-intrinsic pure Sn-based PVK material using evaporation techniques was achieved by Yu et al.(2016), but has never been performed with Sn/Pb-based PVK materials.[96] These findings prove that the severe oxidation observed in spin-coated Sn-based PVKs is not inherent to the PVK material or the raw materials, but rather a product of the processing conditions. The charge carrier mobilities and lifetimes

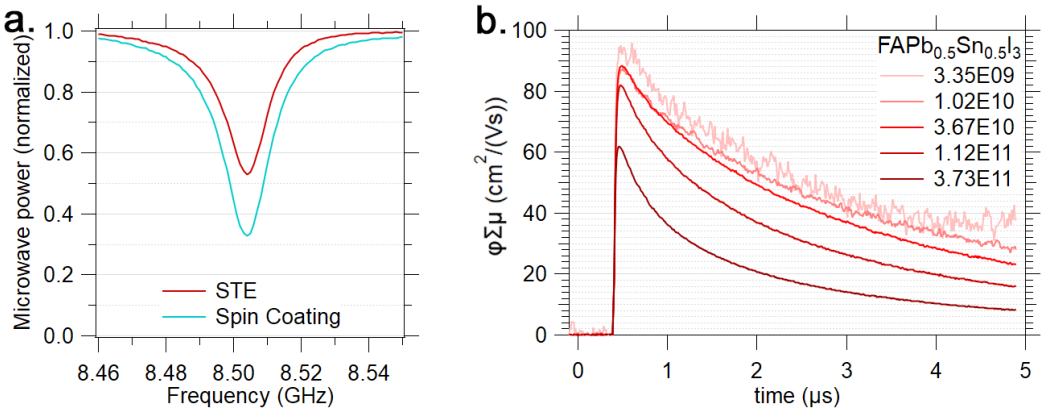

Figure 4.9: a. SSMC traces of PVKs produced via STE (red) and spin coating (teal) without additives. Even when strict synthesis protocols are followed, spin-coated PVKs present with significant doping densities sans additives. **b.** TRMC traces of $FAPb_{0.5}Sn_{0.5}I_3$ produced using STE, annealed at 200 °C for 10 minutes, without additives.

achieved in the experiment, as illustrated in Figure 4.9 **b.**, are on par with or surpassing results reported in literature based on spin coating. The charge carrier mobilities reported in literature for spin-coated $Sn_{0.5}Pb_{0.5}$ halide PVKs are approximately 50 cm^2/Vs,[55, 142] significantly lower than the 90 cm^2/Vs presented here (figure 4.9 **b.**). The attained lifetimes are 2.2 μs (figure 4.9 **b.**), while in research on spin-coated Sn/Pb halide PVKs, four had charge carrier lifetimes of >1 μs,[44, 142–144] and only one of 2 μs.[145] It is important to note that the aforementioned results from literature were all attained using additives such as SnF_2.

The produced PVK boasts a band gap energy of 1.28 eV, comparable to the numbers obtained in literature for spin-coated $FAPb_{0.5}Sn_{0.5}I_3$.[146] For better performance in tandem solar cells, the band gap energy would need to be decreased. By substitution of FA with Cs, Prassana et al.(2017) obtained a band gap energy of 1.24 eV in spin-coated Sn/Pb iodide PVKs.[146] The addition of Cs will be further explored in section 4.5.

4.4. The Role of Tin(II)Fluoride in Sn/Pb PVKs produced via STE

The incorporation of SnF_2 has become a standard practice in the fabrication of spin-coated Sn-based PVK films. Several studies have demonstrated the positive impact of SnF_2 in PVK materials synthesized through vacuum deposition, resulting in significant enhancements in short circuit current density, EQE, and power conversion efficiency (PCE).[59, 114, 115]

Despite these demonstrated improvements, the exact mechanism behind the effects of SnF_2 in Sn-based PVK materials synthesized via TE remains unclear. This section aims to elucidate the effects of excess SnF_2 in Sn/Pb PVK materials produced via sequential thermal evaporation.

As described in section E, 10 mol% excess SnF_2 was introduced via the $PbSnI_4$ alloy. All samples discussed in this chapter are based on the cesium-free composition ($FAPb_{0.5}Sn_{0.5}I_3$). Due to the relatively late discovery of the optimal annealing temperature, the samples containing SnF_2 were annealed twice, once at 130 °C, and once at 200 °C.

4.4.1. Functioning of SnF_2 in STE

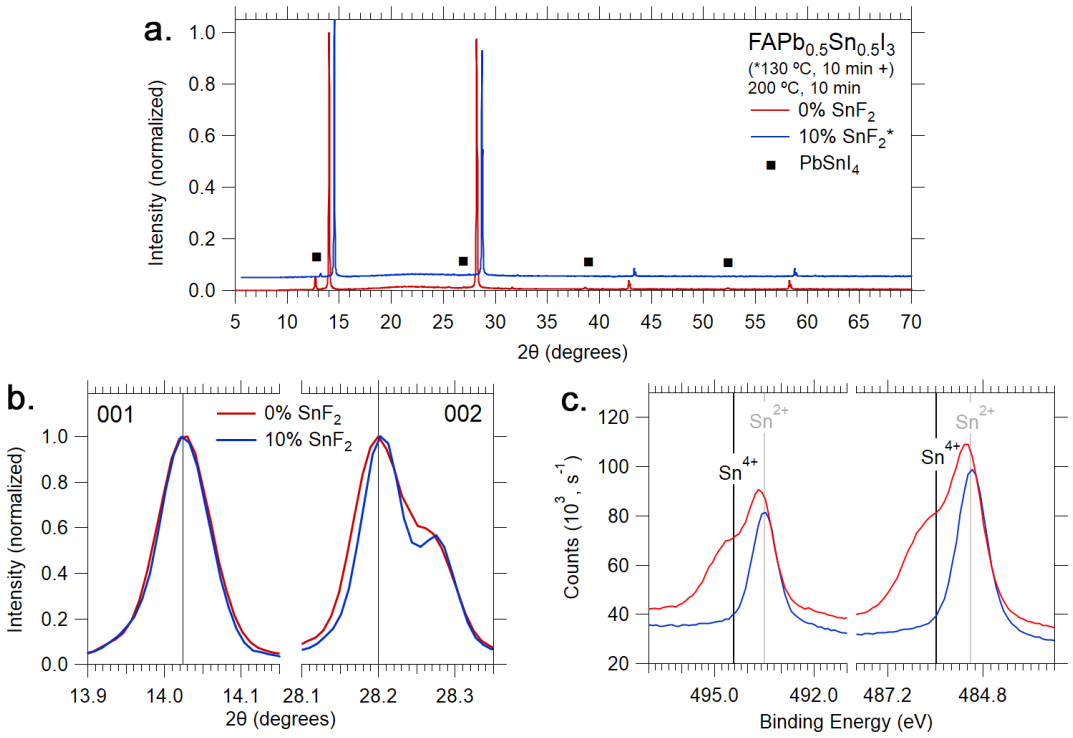

Figure 4.10: a. Normalized XRD pattern of $FAPb_{0.5}Sn_{0.5}I_3$ with and without SnF_2. **b.** Magnified 001 and 002 peaks of the XRD pattern shown in **a.**. **c.** XPS spectrum of the binding energies associated with the Sn3d orbital of $FAPb_{0.5}Sn_{0.5}I_3$ with and without SnF_2. Samples without SnF_2 are shown in red, while samples with SnF_2 are shown in blue.

Using XRD, the successful formation of the PVK phase was established in the sample were SnF_2 was added (figure 4.10 **a.**). The absorption spectrum shows a marginal increase with added SnF_2 (Appendix D, figure D.1). To exclude compositional changes as a potential cause for the effects observed in this research, the composition was examined using EDS and XRD. When comparing overall composition using EDS (table 4.2 and 4.3), the SnF_2-containing sample has a higher Sn:Pb ratio at 1:0.96 compared to 1:1.04 for the SnF_2-free sample. Although this is in line with expectation, as excess SnF_2 could result in excess Sn, the large variance in these numbers (>0.10) means that no definitive conclusions can be drawn.

Figure 4.10 **b.** shows the 001 and 002 peaks of the XRD patterns shown in figure 4.10 **a.**. A negligible shift in angle is observed between the compositions with and without SnF_2. The results from the EDS and XRD rule out compositional changes.

Table 4.5: Table showing the ratio of Sn:Pb in full PVK films deposited using the $PbSnI_4$ alloy measured using EDS in over deposition number. In total, 59 measurements were performed across 4 deposition.

EDS $PbSnI_4$	
Deposition #	Sn:Pb
3	1:1.04±0.20
4	1:1.02±0.12
5	1:1.01±0.14
6	1:1.08±0.21
Overall	1:1.04±0.17

Table 4.6: Table showing the ratio of Sn:Pb in full PVK films deposited using the $PbSnI_4$+10mol% SnF_2 alloy measured using EDS over deposition number. In total, 19 measurements were performed across 4 deposition.

EDS $PbSnI_4$+10%SnF_2	
Deposition #	Sn:Pb
2	1:0.98±0.01
3	1:0.97±0.20
4	1:0.96±0.19
5	1:0.95±0.10
Overall	1:0.97±0.16

XPS was used to investigate the effect of SnF_2 on Sn^{4+} in STE (figure 4.10 **c.**). First, the PVK films were examined for the presence of Sn^{4+} by examining the binding energies associated with the Sn3d orbital. In line with expectations from spin coating, there is a much stronger Sn^{4+} shoulder present in the SnF_2-free compared to the SnF_2-containing PVK. The explicit presence of any SnF_2 or SnF_4 could not be confirmed, as no peaks were observed in the F1s region of the XPS spectrum. However, this is expected, as the low atomic number of fluorine makes it difficult to detect at low concentrations using XPS.

4.4.2. Effect on Optoelectronic Performance

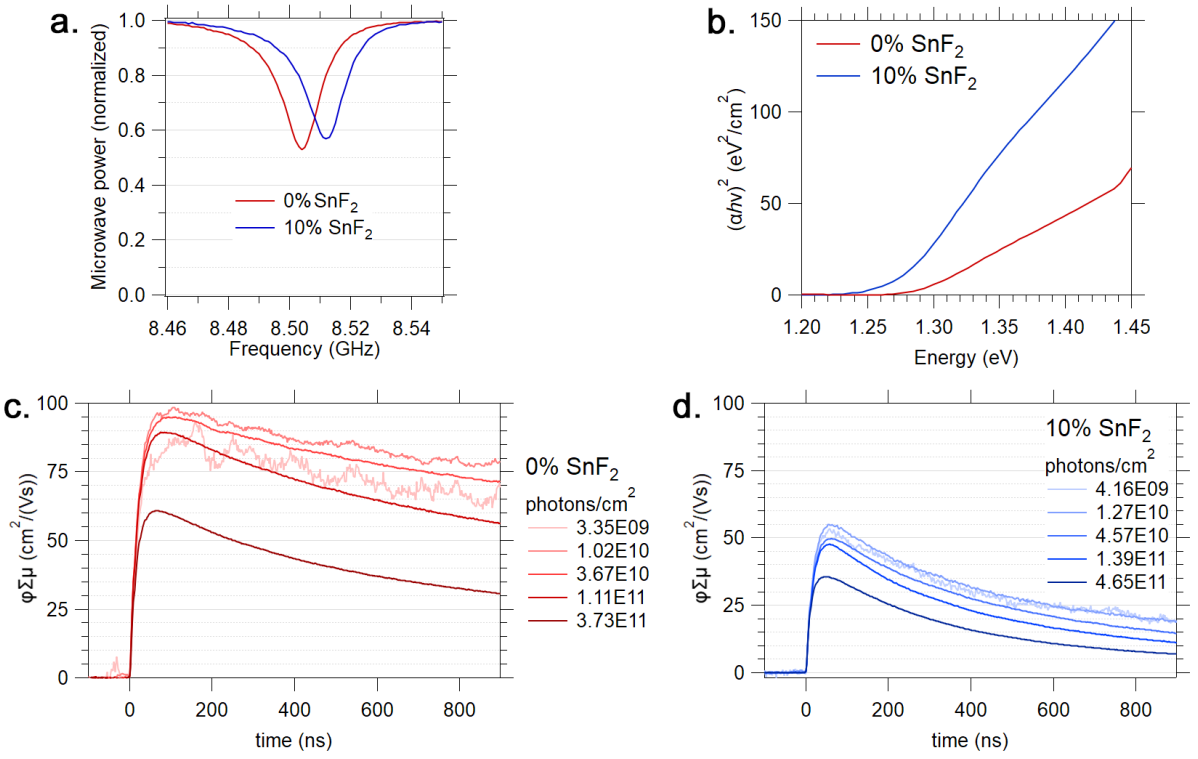

Figure 4.11: a. SSMC plot of $FAPb_{0.5}Sn_{0.5}I_3$ with and without SnF_2. **b.** Tauc plot of $FAPb_{0.5}Sn_{0.5}I_3$ with and without SnF_2. TRMC traces of $FAPb_{0.5}Sn_{0.5}I_3$ **d.** with and **c.** without SnF_2. Both traces were normalized for the fraction of absorbed light. Samples without SnF_2 are shown in red, while samples with SnF_2 are shown in blue.

As stated before, the primary application of SnF_2 in spin coating is to suppress the dark conductivity caused by tin oxidation. SSMC was used to investigate the impact of SnF_2 on the dark conductivity of PVKs produced via STE, the results can be found in figure 4.11 **a.**. The R_0 of both samples with and without SnF_2 are situated above 0.5. The difference between with and without SnF_2 is marginal, falling well within the error in conductivity of the substrate.

Additionally, the optoelectronic properties were assessed using TRMC, the results are shown in figure 4.11 **c.** and **d.**. The addition of 10 mol% excess SnF_2 significantly reduces the charge carrier lifetime. At the same fluency, the charge carrier mobility of the PVK with added SnF_2 is almost halved and the charge carrier half-life is reduced by over 75% (0.45 μs vs 1.9 μs).

These result seems contradictory to what was measured before using XPS, as the presence of the amount of Sn^{4+} observed should result in a significant dark conductivity. In addition, the TRMC shows long lifetimes for the SnF_2-free PVK (figure 4.11 **a.**), which is unlikely with significant p-doping.

A Tauc plot was constructed to investigate differences in electronic band structure (figure 4.11 **c.**). The sample with added SnF_2 shows a double linear region. The implications of a double linear region are discussed in more detail in section 4.5.2. The band gap calculated from the Tauc plot is slightly lower for the SnF_2-containing sample (1.26-1.27 eV) versus the SnF_2-free sample (1.28 eV).

4.4.3. Effect on Crystal Structure and Morphology

XRD was used to investigate the effects of SnF_2 on crystallinity in STE (figure 4.10 **a.**). Compared to the SnF_2-free sample, the SnF_2-containing samples shows a smaller excess $PbSnI_4$ phase. Signal-to-noise ratio is slightly increased upon the addition of SnF_2. Using profilometry, the thickness was determined at 168 nm with SnF_2 and 145 nm without SnF_2 (Appendix D, table D.1). This means that although the SNR is higher in the XRD pattern of the SnF_2-containing composition, when compensated for the difference in thickness the sample containing SnF_2 has similar crystallinity.

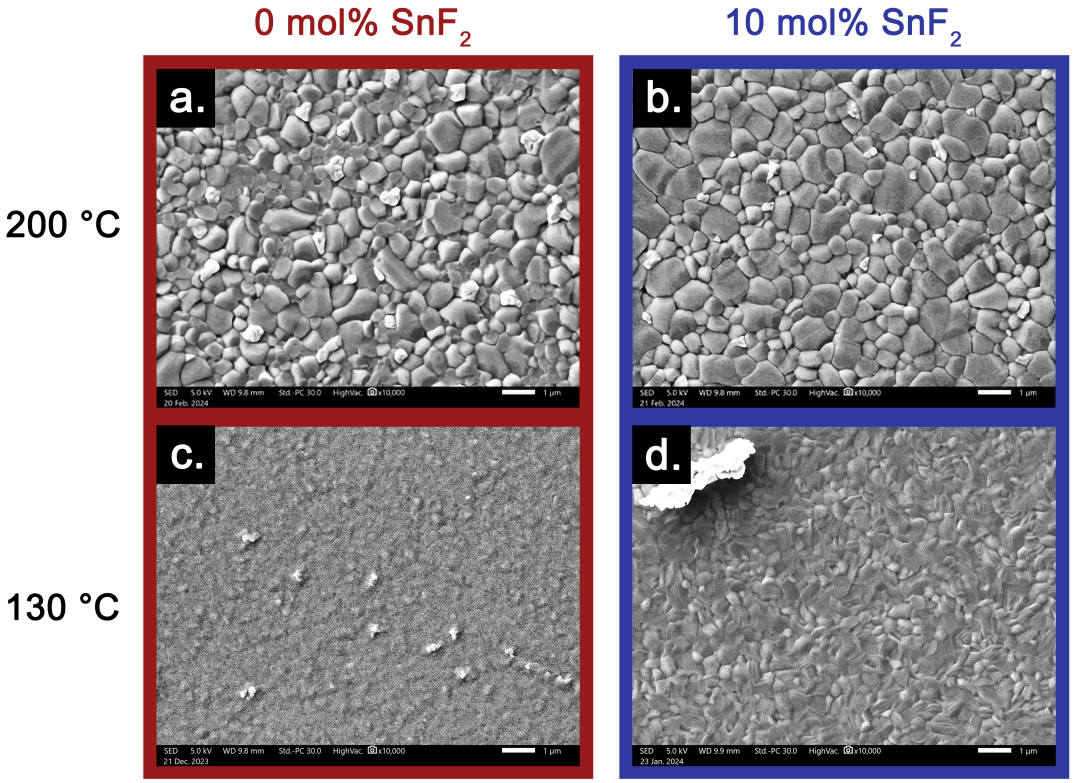

Figure 4.12: Comparison of SEM images of $FAPb_{0.5}Sn_{0.5}I_3$ with and without SnF_2, annealed at 130 and 200 °C. Note: the sample in image **b.** was annealed at 130 and 200 °C

SEM was used to compare the morphology between the samples with and without SnF_2 (figure 4.12). After annealing at 200 °C (figure 4.12 **a.** and **b.**), both samples show good morphology, with the sample containing SnF_2 showing a slightly more uniform and larger grain structure. However, this slight improvement in morphology can be caused by the double annealing procedure. To control for the error caused by the different annealing procedures, the samples are compared with identical annealing procedures (130 °C for 10 minutes, figure 4.12 **c.** and **d.**). Even at an annealing temperature of 130 °C, the sample containing SnF_2 shows a more crystalline and ordered structure.

It remains unclear whether the effects observed during this research can be directly ascribed to SnF_2. The presence of any SnF_2 or SnF_4 in the final film could not be confirmed. None of the research on SnF_2 in vacuum deposition methods were able to provide an explanation for the improved performance. This brings up the question whether the direct effects of SnF_2 are actually observed, or if they are caused by other indirect factors such as a change in vapour pressure or deposition rate. For example, Ball et al.(2019) claim to observe the effects of SnF_2 in co-evaporated samples, however the exact composition of the melt they use is never proven. As they replace SnI_2 with SnF_2, the observed effect could be caused by the decrease in SnI_2:PbI_2 ratio. Furthermore, (S)TE is able to produce low-doping-density PVK films without the need for SnF_2.

4.4.4. Summary

SnF_2 is commonly used in spin coating processes to mitigate issues related to the presence of Sn^{4+} and improve film properties. However, its effectiveness in STE remains uncertain. Several studies have shown positive impacts of SnF_2 in PVK materials synthesized through vacuum deposition.

This chapter explored the effects of excess SnF_2 (10 mol%) in $FAPb_{0.5}Sn_{0.5}I_3$ films produced via STE. Analysis using TRMC and SSMC indicates that SnF_2 does not reduce dark conductivity, and significantly decreases charge carrier lifetime. Crystal structure and morphology assessments reveal marginal differences between samples with and without SnF_2, suggesting slight improvements in morphology with SnF_2 addition.

Efforts to gain insight into the effect of SnF_2 in STE remain inconclusive. XPS analysis suggests a decrease in Sn^{4+} content in PVK films with SnF_2, however the difference in Sn^{4+} concentration seems to have no negative impact on optoelectronic performance. In literature there is significant ambiguity regarding the direct effects of SnF_2 versus potential indirect factors, such as changes in composition.

4.5. The effects of Cesium fraction in Sn/Pb PVKs deposited via STE

The Goldschmidt tolerance factor, discussed in theory section 2.2.1, is widely accepted as a predictor for thermal stability, phase stability and electronic performance. This tolerance factor serves as a guiding principle in the design and optimization of many perovskite materials.[66, 147–151] Perovskite materials with a tolerance factor between 0.85 and 1.00 generally produce a stable photoactive phase at room temperature.[66, 147, 149, 151]

In spin coating, an A-site composition of x=0.20-0.25 Cs_xFA_{1-x}, equal to a tolerance factor of 0.96-0.95, leads to the best electronic performance and stability for Sn/Pb perovskites.[73] In Pb-based iodide PVKs, the addition Cs seems to extend beyond modulation of the tolerance factor. At only 10% substitution, Cs is able to improve the PCE in Pb-based PVK devices with 50%.[152]

As underlined in the previous sections, the mechanisms at play in PVKs produced via STE are significantly different from those produced by spin coating. Whether the Goldschmidt tolerance factor can accurately predict the performance of PVKs produced via STE has not been investigated. In this section, the effect of the Cs fraction (and by extension the Goldschmidt tolerance factor) on Sn/Pb narrow band gap PVK produced using STE will be discussed.

Four different compositions with varying fractions of Cs were tested ($Cs_xFA_{1-x}Pb_{0.5}Sn_{0.5}I_3$). The composition is described as the fraction of the A-site occupied by Cs, where the remaining fraction is occupied by formamidinium. An overview of the four A-site compositions, with the corresponding tolerance factor, can be found in table 4.7.

Table 4.7: Table showing the four different target compositions, measured compositions and the corresponding Goldschmidt tolerance factor.

Target Cs fraction (ratio Cs:(Pb+Sn))	Measured Cs fraction (ratio Cs:(Pb+Sn), EDS	Goldschmidt tolerance factor (τ)
0	0	0.99
0.05	0.06	0.98
0.25	0.23	0.95
0.40	0.42	0.92

Using EDS, the final fraction of Cs was determined (table 4.7, second column). Although ideally one would calculate the fraction of the A-site occupied by Cs, the introduction of carbon via contamination makes this unreliable. Instead, the Cs content was determined using the ratio between the atomic fraction of Cs versus the atomic fraction of the sum of lead and tin. This introduces a certain amount of inaccuracy, as $PbSnI_4$ is added in excess, however the amount of excess $PbSnI_4$ is small as observed in figure C.3 found in Appendix C.

The annealing temperature optimization outlined in section 4.2 was repeated with $Cs_{0.05}FA_{0.95}Pb_{0.5}Sn_{0.5}I_3$, to serve as a model for all Cs-containing PVK materials tested. The results were largely similar to those demonstrated in section 4.2 for $FAPb_{0.5}Sn_{0.5}I_3$, showing optimal performance at an annealing temperature of 200 °C. Thus, all PVK materials discussed in this chapter were annealed at 200 °C for 10 minutes. In addition, two deposition orders of $Cs_{0.05}FA_{0.95}Pb_{0.5}Sn_{0.5}I_3$ were compared ($PbSnI_4$, FAI, CsI and $PbSnI_4$, CsI, FAI). The complete data for the annealing temperature and deposition order optimization of $Cs_{0.05}FA_{0.95}Pb_{0.5}Sn_{0.5}I_3$ can be found in Appendix B.2 and B.3.

4.5.1. Successful Cesium Doping

Before the effects of Cs can be assessed, successful doping needs to be established. To prove the successful integration of Cs, XRD was performed to examine structural changes. With an increase in Cs doping, a positive peak shift in the XRD spectrum (corresponding to lattice contraction) is expected. In addition, the peak height of the Cs phase should be minimal to indicate complete substitution, although the absence of Cs in an amorphous phase cannot be proven.

Due to the highly preferred orientation of the crystal structure, only the 100 and 200 peaks are shown in figure 4.13 **a.**. All peaks were individually normalized. The spectra were not corrected for kα2. The full XRD spectra can be found in Appendix C, figure C.3. All samples show a high signal-to-noise ratio in the XRD spectra, with similar peak sharpness. From this, the crystallinity is assumed to be comparable between samples. No peaks are observed corresponding to a CsI phase.[153] A clear positive relationship is observed between Cs fraction and peak position (figure 4.13 **a.**). An increase in diffraction angle suggests lattice contraction. The calculated lattice parameter versus Cs fraction is shown above in figure 4.13 **b.**. Using profilometry the thicknesses were determined to be similar

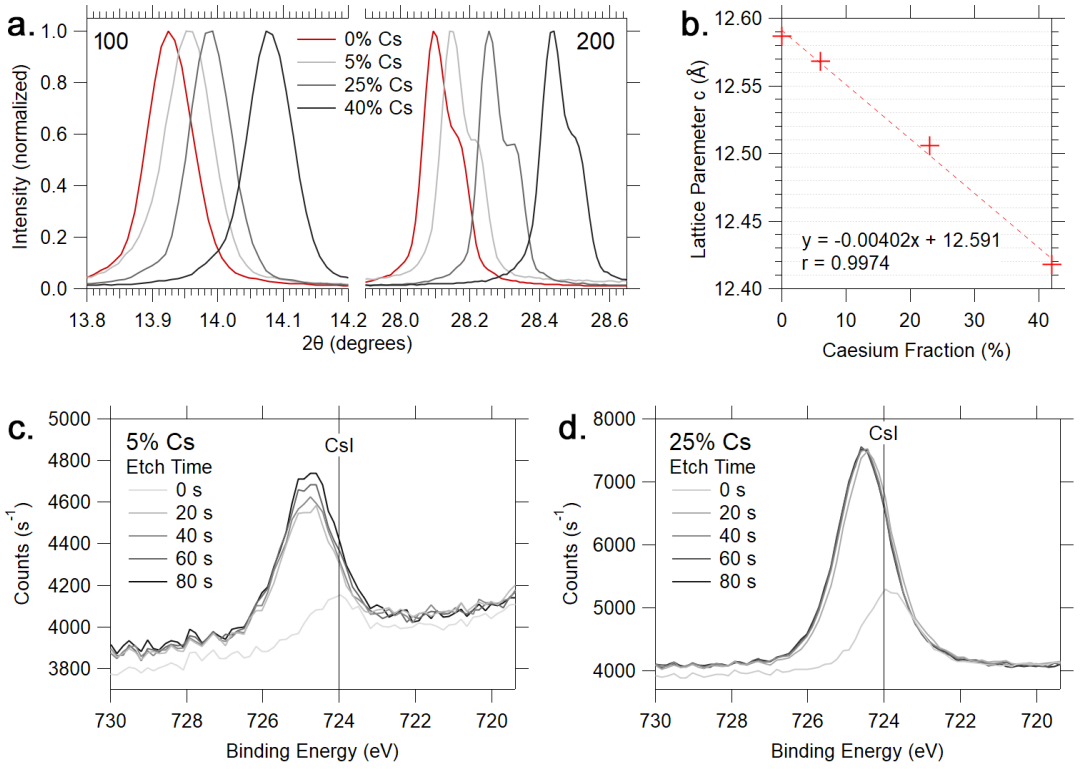

Figure 4.13: a. Normalized XRD plot of the 100 and 200 peaks of the four different A-site compositions showing the shift in lattice parameter. **b.** The lattice parameter of the different A-site compositions as calculated from the XRD spectum in **a.** versus the Cs fraction. **c.** and **d.** XPS depth profiles of 5 (**c.**) and 25% (**d.**) Cs.

at approximately 145 nm (Appendix C, tabel C.1), this means that XRD data can be used to directly compare crystallinity. Interestingly, an almost identical thickness implies that the compositions containing Cs undergo thermal decomposition and shrinkage at the same rate as the composition without Cs. Cs-containing PVK materials are generally understood to have higher thermal stability.[154–156]

XPS was performed to investigate the distribution of Cs across the films thickness (figure 4.13 **c.** and **d.**.) In both the 5 and 25% Cs compositions, the binding energy increases considerably from 0 to 20 seconds of etching. The initial peak position corresponds to CsI, while inside the film the Cs atoms are bonded differently, with a higher binding energy. The difference in binding energy between surface and bulk can either be caused by the integration of Cs into the PVK structure or due to charging and discharging effects caused by the XPS process.

A small increase in peak intensity is seen with increasing etch times for the 5% Cs composition, while the peak intensity for 25% Cs PVK remains stable. This indicates that the distribution of Cs in the 25% Cs sample is homogeneous, while the 5% shows a slight gradient.

In summary, the above-provided data points towards the successful integration of Cs into the A-site of the PVK phase. The XRD analysis reveals a positive peak shift with increasing Cs doping, indicating lattice contraction and successful integration of Cs. The absence of distinct CsI peaks in the XRD spectra further confirms Cs integration into the PVK. XPS measurements reveal an increase in bonding energy over CsI, indicating that Cs atoms have been integrated into the PVK structure.

4.5.2. Effect on Optoelectronic Properties

TRMC was used as the primary method for assessing the performance of the different A-site compositions. The TRMC traces of the different Cs fractions can be found in figure 4.14 **a.** to **d.**. The 0% Cs

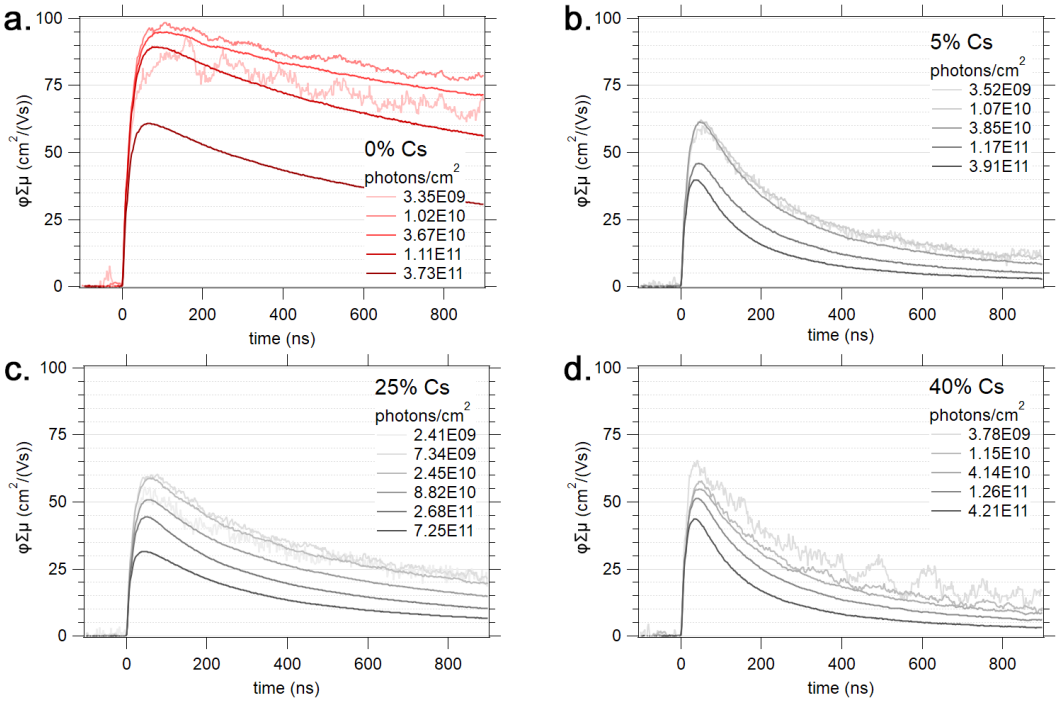

Figure 4.14: TRMC traces of $Cs_xFA_{1-x}Pb_{0.5}Sn_{0.5}I_3$, where x is **a.** 0%, **b.** 5%, **c.** 25%, and **d.** 40%. All graphs were normalized for the fraction of absorbed light (F_A). The sample without Cs (**a.**) shows superior charge carrier recombination kinetics over the samples with Cs (**b.**, **c.**, **d.**). Due to the significantly longer lifetimes of the 0% Cs sample, an additional measurement was performed with a 10 μs timescale, which can be found in Appendix C, fig.C.1

composition managed to attain a photoconductance peak of 95 cm^2/Vs, with a charge carrier half-life of 2.2 μs (section 4.3, figure 4.9 **b.**). Upon the addition of any percentage of Cs, the charge carrier lifetimes reduce significantly to less than 0.5 μs. Once Cs is added, the quantity of Cs does not effect the $\phi\Sigma\mu$ peak. Lifetimes at 25% Cs are improved over 5 and 40% Cs, however they are still much shorter than 0% Cs. All compositions show a tail that approaches zero at longer timeframes (see Appendix C, figure C.1 **a.**), which indicates minimal trapping and/or doping behavior. This is further compounded by the SSMC results (Appendix C, figure C.2), showing R_0 values upwards of 0.5, indicating low dark conductivity.

Contrary to what is observed in spin-coated PVKs, the Cs-free PVK managed to outperform all of the Cs-based PVK versions based on charge carrier kinetics.[73, 152] In spin coating, the addition of cesium results in a significant increase in charge carrier lifetimes.[156]

ELECTRONIC BAND STRUCTURE

As described in section 2.2.2, through structural changes, the A-site composition can have a significant effect on the electronic structure of a PVK material.[26, 68, 157–159] This relation has yet to be described for Sn/Pb iodide PVK materials produced by STE. The effect of A-site composition on the electronic band structure was investigated using a Tauc plot (figure 4.15). The 0% Cs composition

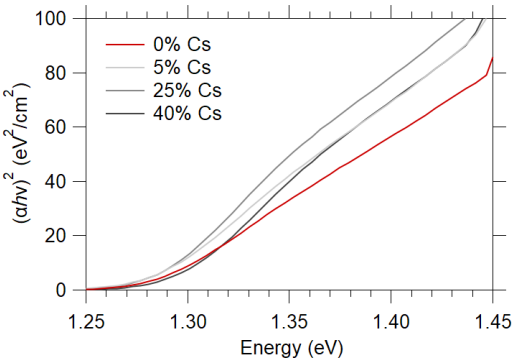

Figure 4.15: Tauc plot showing the four different A-site compositions.

shows a slope with an x-axis intersect of 1.28 eV. Interestingly, all compositions containing Cs show a double linear region with two x-axis intersects. The lowest band gap energy is observed in the upper slope of 25% Cs, with a x-axis intersect of 1.26 eV. The lower linear regions of the Cs-containing compositions show a higher band gap of approx. 1.29 eV. The lowest band gap observed at 25% Cs is in line with results from research performed in spin coating.[1, 160]

A double linear region in a Tauc plot indicates the presence of two allowed direct transitions at photon energies of <1.3 eV. There are two causes behind this behaviour, either two separate PVK phases have formed with different band gaps, or the electronic band structure was changed upon the addition of Cs, allowing for an additional transition with a different reciprocal lattice vector. The presence of two separate phases is not observed in the XRD spectra, making the first option unlikely. The introduction of Cs could cause octahedral tilting, which is known to induce Bychkov–Rashba splitting in some PVKs,[161] resulting in two allowed transitions at similar band gap energies.

The replacement of even a minimal percentage of FA with Cs significantly reduces the charge carrier lifetime. In addition, the Tauc plot suggests a change in electronic structure upon the addition of Cs. In literature, the addition of Cs in spin-coated Sn/Pb PVK materials has been shown to result in a significant increase in charge carrier lifetimes and short-circuit current density.[156] Sn/Pb PVK materials with mixed FA/Cs A-sites have consistently led to the highest-performing absorber layers in spin coating.[73] This rules out Cs as a inherent cause for poor optoelectronic behaviour. It is therefore assumed that the underlying cause lies in a process specific to STE.

The Cs-containing and Cs-free compositions were compared based on crystallinity, delta phase size, precursor phase size, composition, trapping behaviour and dark conductivity (Appendix C, figures C.1 **b.**, C.3, and table C.2), however no explanations could be found for the discrepancy in performance.

4.5.3. Effect on Morphology

SEM was employed to examine the morphology of the four different A-site compositions at different magnifications. A comparison between 0, 5, 25 and 40% Cs at a magnification of x10.000 is shown in figure 4.16 **a.** to **d.**. In addition, the average grain size and grain size distribution were determined using ImageJ, which are shown in figure 4.16.

All films exhibit grain structures with high levels of surface coverage and minimal pin-holing. Comparing various Cs compositions, a clear trend emerges: Maximum grain sizes increase with higher Cs fractions. However, this increase is accompanied by a decrease in minimum grain size, resulting in a broader size distribution as depicted by the histograms in figure 4.16.

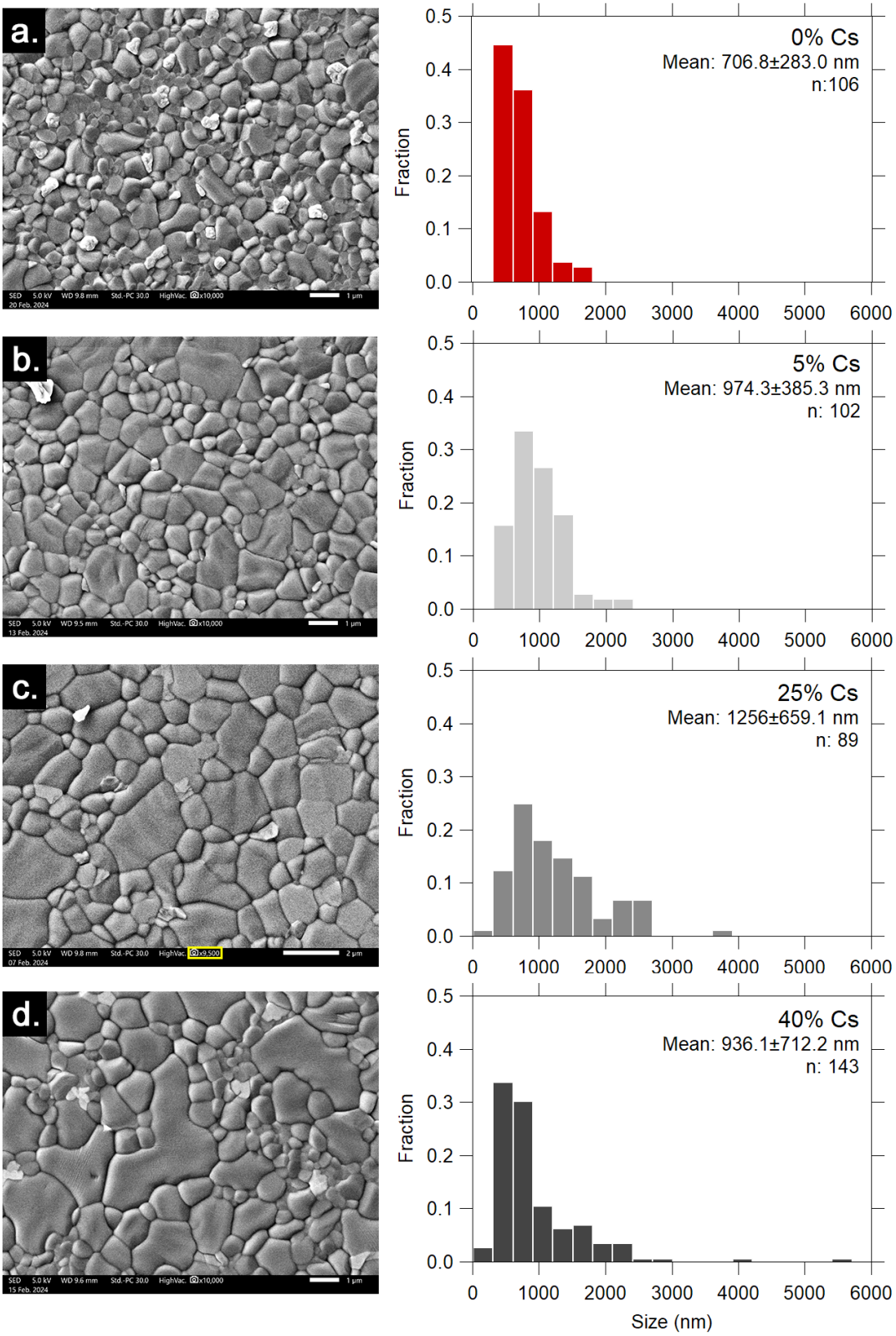

Figure 4.16: SEM SED images of 0 (**a.**), 5 (**b.**), 25 (**c.**), 40% (**d.**) Cs PVKs at a magnification of 10,000x (figure **c.** at 9,500x). On the right, the corresponding grain size distributions are shown (ImageJ).

A widening size distribution is an indication of a process called Ostwald ripening. Ostwald ripening is a phenomenon in which larger particles grow at the expense of smaller ones. It occurs due to differences in the chemical potential of smaller and larger particles as described by Kelvin's equation (equation 4.1):

$$\Delta\mu = \frac{2\sigma\nu_{at}}{r} \tag{4.1}$$

where μ corresponds to the chemical potential, σ to the surface tension, ν_{at} to the atomic volume and r to the particle radius. One could consider this process to be driven by the minimization of the overall surface energy of the system.

As the initial particle size, annealing temperature and annealing time were similar, it is deemed probable that Ostwald ripening rate increases with an increase in Cs fraction. The rate at which Ostwald ripening occurs is influenced by many factors, including diffusion rate, lattice strain, film density, surface energy and cohesion. With the data available, it is uncertain how Cs influences the Ostwald ripening rate.

According to the size distribution, the largest average grain size appears at 25% Cs. However, visually the grains in the 40% Cs sample appear to be much larger. A potential cause for this contradiction lies in the method by which the size distribution is measured. The fraction shown on the Y-axis in the histograms of figure 4.16 above is the number of grains divided by the total number of grains, this fraction does not consider the size of the grains. As the same area can either be occupied by one large grain or several small grains, the size distribution is skewed towards smaller grain sizes.

The results obtained in this research deviate from those seen in films produced using spin coating and co-deposition. Films produced via these methods often yield a more spherical and disordered grain structure with smaller grains (100-800 nm).[59, 140, 162–165] The grain structures observed in the samples produced during this research possess a much more geometric grain structure, showing visible facets.

However, the difference in formation mechanism cannot fully explain the difference in the final morphology, as films produced via STE show an equally poor structure pre-annealing. A possible explanation for the significant difference in morphology is the higher annealing temperature employed in this research. As explained in section 4.2, annealing at temperatures above 150 °C is generally avoided in organic-based perovskites. Annealing at higher temperatures generally promotes diffusion and recrystallization, leading to an improvement in morphology. This leads to the conclusion that PVK films produced via STE do not possess an inherently improved morphology, but rather allow for higher annealing temperatures, which in turn lead to improved morphology.

4.5.4. Summary

Structural analysis through XRD and XPS confirms successful Cs integration into the PVK structure. In spin coating, 20-25% Cs often leads to the best optoelectronic performance, ascribed to optimization of the Goldschmidt tolerance factor. The data from this research seems to break this trend, the addition of Cs significantly reduces charge carrier mobility and lifetime. Tauc plot analysis indicates changes in the electronic band structure with Cs addition. Morphological examination reveals a trend of increasing grain size and broadening size distribution with higher Cs fractions. The higher annealing temperatures enabled by STE are expected to contribute to the improved morphology over spin coating, suggesting that the differences in morphology between STE and spin coating methods are potentially driven by annealing conditions rather than inherent mechanisms.

5
CONCLUSIONS AND RECOMMENDATIONS

5.1. Conclusions

This research demonstrates that STE can produce high performance (charge carrier mobilities of 100 cm^2/Vs, lifetimes of over 2 μs) and low dark conductivity (<3 μS) narrow band gap (<1.28 eV) Sn/Pb PVK absorber layers without additives, a substantial deviation from results seen in spin-coated PVKs.

In-situ synthesis procedures for $PbSnI_4$ and $PbSnI_4$+SnF_2 alloys were introduced, allowing for faster production compared to previous methods. Structural characterization confirms the successful production of crystalline $PbSnI_4$ and $PbSnI_4$+SnF_2 powders. Eutectic thermal evaporation experiments demonstrate that $PbSnI_4$ evaporates as a single material. XRD analysis reveals strongly preferential growth in the 100 direction, consistent with vacuum deposition mechanisms. EDS confirms that thin films produced using $PbSnI_4$ are consistent in Sn:Pb composition across many depositions.

The optimal annealing temperature for $FAPb_{0.5}Sn_{0.5}I_3$ and $Cs_{0.05}FA_{0.95}Pb_{0.5}Sn_{0.5}I_3$ was determined at 200 °C. SSMC measurements indicate low doping densities (R_0>0.5) across all annealing temperatures. TRMC analysis revealed significant improvements in charge carrier dynamics at 200 °C over annealing temperatures of 120 to 180 °C. Examination using XRD showed that at 200 °C, decomposition of the PVK structure starts to occur. Further investigation suggests that the increase in performance from 180°C to 200°C is attributed to significant changes in morphology due to recrystallization, leading to larger and more structured grains. This hypothesis is supported by SEM analysis revealing substantial differences in grain size and morphology between samples annealed at 180°C and 200°C. Notably, the annealing temperature of 200 °C for organic(-inorganic) Sn/Pb iodide PVKs produced via STE differs significantly from spin-coated PVKs. Annealing temperatures above 150 °C are tend to introduce significant decomposition in spin-coated PVKs.

Using XRD, crystal lattice contraction was observed upon the introduction of cesium. The distribution and binding energy of cesium was examined using XPS, revealing a (nearly) homogeneous distribution with significantly altered binding energies. This data indicates successful cesium integration into the perovskite structure was achieved. The substitution of cesium into the A-site led to a reduction in charge carrier mobility (100 to 60 cm^2/Vs) and lifetime (2 to 0.5 μs). Electronic band structure analysis using a Tauc plot revealed changes in the band gap energy and structure upon cesium doping (1.28 to 1.26 eV). Sn/Pb PVK materials with mixed FA-Cs A-sites have consistently led to the highest performing absorber layers in spin coating.[73] Analysis using SEM indicated a positive correlation between cesium fraction and maximum grain size. Increasing cesium fraction led to increased grain size distribution, which was ascribed to increased Ostwald ripening. In PVKs produced via STE, the addition of cesium seems to have an effect beyond the tuning of the Goldschmidt tolerance factor.

TRMC analysis revealed that the addition of SnF_2 led to a significant reduction in charge carrier mobilities (from 100 to 55 cm^2/Vs) and lifetimes (from 2 to 0.5 μs). The morphology was slightly improved upon the addition of SnF_2, showing a more ordered grain structure. It can not be ruled out that the observed changes in morphology and optoelectronic properties, both in this work and literature, may be caused by indirect factors such as changes in composition or deposition charachteristics.

5.2. Recommendations for Future Research

The continued development of $FAPb_{0.5}Sn_{0.5}I_3$ produced via STE is strongly recommended. The produced absorber layer materials have demonstrated favourable optoelectronic properties for use in full stack devices. The next steps towards building a full device would be:

1. **Increasing the thickness of the absorber layer (>500 nm).** Despite the absorption coefficient, the low thickness of the final film (145 nm) leads to relatively low absorption at the wavelengths of interest. To improve this, it is suggested to increase the thickness of the absorber layer. For STE, multi-cycle depositions can be employed to overcome the limited reaction depth.[137, 166, 167]
2. **Investigate the cross-sectional morphology.** Grain structure plays an important role in PVK solar cell performance and stability.[168–171] By having continuous grains across the depth of the film, losses due to recombination and contact resistance are minimized.
3. **Cell fabrication.** To both streamline the production process and reduce the introduction of environmental oxygen, it is recommended to focus research on the vacuum deposition of charge transport layers. Yuan et al.(2023) have demonstrated the vacuum deposition of a complete device, including charge transport layers, based on a $CsFaPbI_3$ absorber layer.[172]

Based on the conclusions from this research, it is not recommended to pursue further research into SnF_2 for vacuum deposition. To further improve the optoelectronic performance of the $FAPb_{0.5}Sn_{0.5}I_3$ absorber layer, it is instead recommended to focus research on further optimization of the annealing procedure. It is recommended to investigate:

- **Annealing at temperatures higher than 200 °C.** Although an annealing temperature of 200 °C was assumed optimal due to the onset of decomposition, it has not been explicitly proven that higher temperatures lead to worse optoelectronic performance and morphology.
- **Annealing at temperatures higher than 200 °C, less than 1 minute.** Research conducted on spin-coated PVKs has indicated that annealing at temperatures exceeding 200 °C for shorter durations can notably enhance both optoelectronic performance and morphology, while minimizing decomposition effects.[172, 173] If the recrystallization theory put forward in section 4.2 is correct, shorter annealing procedures at higher temperatures results in similar improvements.
- **Annealing at temperatures lower than 200 °C, longer than 10 minutes.** To further investigate the recrystallization mechanism, one could anneal the samples for much longer than 10 minutes at temperatures below 200 °C, to see if the same changes occur. If the increase in performance from 180 to 200 °C seen in section 4.2 is indeed caused by recrystallization, annealing at lower temperatures for longer times will not yield the same results as annealing at higher temperature for shorter times.
- **Annealing the $PbSnI_4$ precursor layer.** According to research by Moser et al.(2022), the precursor layer functions as structural scaffolding for the formation of the PVK in STE.[34] To improve morphology while minimizing decomposition of the organic component, a thin film consisting of only $PbSnI_4$ could be annealed. The A-site components could then be deposited and annealed.

In spin-coated PVKs, the addition of cesium generally leads to an increase in charge carrier lifetimes and mobilities.[73, 156] The contradiction with the results presented during this research (section 4.5) warrants additional investigation. The changes observed in the Tauc plot (figure 4.15) suggests further research into the electronic band structure.

REFERENCES

[1] He Dong et al. “Metal Halide Perovskite for next-generation optoelectronics: progresses and prospects”. In: *eLight 2023 3:1* 3 (1 Jan. 2023), pp. 1–16. ISSN: 2662-8643. DOI: 10.1186/S43593-022-00033-Z.

[2] Pilik Basumatary and Pratima Agarwal. “A short review on progress in perovskite solar cells”. In: *Materials Research Bulletin* 149 (May 2022), p. 111700. ISSN: 00255408. DOI: 10.1016/j.materresbull.2021.111700.

[3] Xiaojuan Fan. “Advanced progress in metal halide perovskite solar cells: A review”. In: *Materials Today Sustainability* 24 (Dec. 2023), p. 100603. ISSN: 2589-2347. DOI: 10.1016/J.MTSUST.2023.100603.

[4] Zhaoning Song et al. “Pathways toward high-performance perovskite solar cells: review of recent advances in organo-metal halide perovskites for photovoltaic applications”. In: *https://doi.org/10.1117/1.JPE.* 6 (2 Apr. 2016), p. 022001. ISSN: 1947-7988. DOI: 10.1117/1.JPE.6.022001.

[5] Sebastian F. Hoefler, Gregor Trimmel, and Thomas Rath. “Progress on lead-free metal halide perovskites for photovoltaic applications: a review”. In: *Monatshefte fur chemie* 148 (5 May 2017), pp. 795–826. ISSN: 0026-9247. DOI: 10.1007/S00706-017-1933-9.

[6] Reza Taheri-Ledari et al. “A Review of Metal-Free Organic Halide Perovskite: Future Directions for the Next Generation of Solar Cells”. In: *Energy and Fuels* 36 (18 Sept. 2022), pp. 10702–10720. ISSN: 15205029. DOI: 10.1021/ACS.ENERGYFUELS.2C01868.

[7] Michael Saliba et al. “Incorporation of rubidium cations into perovskite solar cells improves photovoltaic performance”. In: *Science* 354 (6309 Oct. 2016), pp. 206–209. ISSN: 10959203. DOI: 10.1126/SCIENCE.AAH5557/SUPPL_FILE/SALIBA.SM.PDF.

[8] Giles E. Eperon et al. “Formamidinium lead trihalide: a broadly tunable perovskite for efficient planar heterojunction solar cells”. In: *Energy & Environmental Science* 7 (3 Feb. 2014), pp. 982–988. ISSN: 1754-5706. DOI: 10.1039/C3EE43822H.

[9] Woon Seok Yang et al. “High-performance photovoltaic perovskite layers fabricated through intramolecular exchange”. In: *Science* 348 (6240 June 2015), pp. 1234–1237. ISSN: 10959203. DOI: 10.1126/SCIENCE.AAA9272/SUPPL_FILE/YANG-SM.PDF.

[10] Michael M. Lee et al. “Efficient hybrid solar cells based on meso-superstructured organometal halide perovskites”. In: *Science* 338 (6107 Nov. 2012), pp. 643–647. ISSN: 10959203. DOI: 10.1126/SCIENCE.1228604/SUPPL_FILE/LEE.SM.PDF.

[11] Samuel D. Stranks et al. “Electron-Hole Diffusion Lengths Exceeding 1 Micrometer in an Organometal Trihalide Perovskite Absorber”. In: *Science* 342 (6156 Oct. 2013), pp. 341–344. ISSN: 0036-8075. DOI: 10.1126/science.1243982.

[12] Oct. 2023. URL: https://www.nrel.gov/pv/cell-efficiency.html.

[13] Sven Rühle. “Tabulated values of the Shockley–Queisser limit for single junction solar cells”. In: *Solar Energy* 130 (June 2016), pp. 139–147. ISSN: 0038092X. DOI: 10.1016/j.solener.2016.02.015.

[14] Marina R. Filip et al. “Steric engineering of metal-halide perovskites with tunable optical band gaps”. In: *Nature Communications* 5 (1 Dec. 2014), p. 5757. ISSN: 2041-1723. DOI: 10.1038/ncomms6757.

[15] Sneha A. Kulkarni et al. “Band-gap tuning of lead halide perovskites using a sequential deposition process”. In: *J. Mater. Chem. A* 2 (24 2014), pp. 9221–9225. ISSN: 2050-7488. DOI: 10.1039/C4TA00435C.

[16] Christian Wehrenfennig et al. “High Charge Carrier Mobilities and Lifetimes in Organolead Trihalide Perovskites”. In: *Advanced Materials* 26 (10 Mar. 2014), pp. 1584–1589. ISSN: 0935-9648. DOI: 10.1002/adma.201305172.

[17] Zhibin Yang et al. “Enhancing electron diffusion length in narrow-bandgap perovskites for efficient monolithic perovskite tandem solar cells”. In: *Nature Communications* 10 (1 Oct. 2019). ISSN: 2041-1723. DOI: 10.1038/s41467-019-12513-x.

[18] Tomas Leijtens et al. “Opportunities and challenges for tandem solar cells using metal halide perovskite semiconductors”. In: *Nature Energy* (). DOI: 10.1038/s41560-018-0190-4. URL: https://doi.org/10.1038/s41560-018-0190-4.

[19] Giles E. Eperon, Maximilian T. Hörantner, and Henry J. Snaith. “Metal halide perovskite tandem and multiple-junction photovoltaics”. In: *Nature Reviews Chemistry* 1 (12 Nov. 2017). ISSN: 2397-3358. DOI: 10.1038/s41570-017-0095.

[20] Ben Minnaert and Peter Veelaert. “Guidelines for the Bandgap Combinations and Absorption Windows for Organic Tandem and Triple-Junction Solar Cells”. In: *Materials* 5 (10 Oct. 2012). ISSN: 1996-1944. DOI: 10.3390/ma5101933.

[21] Jino Im et al. “Antagonism between Spin-Orbit Coupling and Steric Effects Causes Anomalous Band Gap Evolution in the Perovskite Photovoltaic Materials CH3NH3Sn1-xPbxI3”. In: *Journal of Physical Chemistry Letters* 6 (17 Aug. 2015), pp. 3503–3509. ISSN: 19487185. DOI: 10.1021/ACS.JPCLETT.5B01738/SUPPL_FILE/JZ5B01738_SI_001.PDF.

[22] Ahmed Esmail Shalan. “Challenges and approaches towards upscaling the assembly of hybrid perovskite solar cells”. In: *Materials Advances* 1 (3 June 2020), pp. 292–309. ISSN: 2633-5409. DOI: 10.1039/D0MA00128G.

[23] Longbin Qiu, Luis K. Ono, and Yabing Qi. “Advances and challenges to the commercialization of organic–inorganic halide perovskite solar cell technology”. In: *Materials Today Energy* 7 (Mar. 2018), pp. 169–189. ISSN: 2468-6069. DOI: 10.1016/J.MTENER.2017.09.008.

[24] Jorge Pascual et al. “Fluoride Chemistry in Tin Halide Perovskites”. In: *Angewandte Chemie International Edition* 60 (39 Sept. 2021), pp. 21583–21591. ISSN: 1521-3773. DOI: 10.1002/ANIE.202107599.

[25] Peipei Du et al. “Thermal Evaporation for Halide Perovskite Optoelectronics: Fundamentals, Progress, and Outlook”. In: *Advanced Optical Materials* 10 (4 Feb. 2022). ISSN: 2195-1071. DOI: 10.1002/adom.202101770.

[26] Hyemin Lee et al. “Progress and outlook of Sn–Pb mixed perovskite solar cells”. In: *Nano Convergence* 10 (1 June 2023), p. 27. ISSN: 2196-5404. DOI: 10.1186/s40580-023-00371-9.

[27] Jorge Pascual et al. “Origin of Sn(II) oxidation in tin halide perovskites”. In: *Materials Advances* 1 (5 Aug. 2020), pp. 1066–1070. ISSN: 2633-5409. DOI: 10.1039/D0MA00245C.

[28] Eros Radicchi et al. “Solvent dependent iodide oxidation in metal-halide perovskite precursor solutions”. In: *Physical Chemistry Chemical Physics* 25 (5 Feb. 2023), pp. 4132–4140. ISSN: 1463-9084. DOI: 10.1039/D2CP04266E.

[29] Zhihao Zhang et al. “Mechanistic Understanding of Oxidation of Tin□based Perovskite Solar Cells and Mitigation Strategies”. In: *Angewandte Chemie International Edition* (Aug. 2023). ISSN: 1433-7851. DOI: 10.1002/anie.202308093.

[30] Felix Utama Kosasih et al. “Thermal evaporation and hybrid deposition of perovskite solar cells and mini-modules”. In: *Joule* 6 (12 Dec. 2022), pp. 2692–2734. ISSN: 2542-4785. DOI: 10.1016/J.JOULE.2022.11.004.

[31] S. R. Bae, D. Y. Heo, and S. Y. Kim. “Recent progress of perovskite devices fabricated using thermal evaporation method: Perspective and outlook”. In: *Materials Today Advances* 14 (June 2022), p. 100232. ISSN: 2590-0498. DOI: 10.1016/J.MTADV.2022.100232.

[32] Hao Hu et al. “Vapour-based processing of hole-conductor-free CH3NH3PbI3 perovskite/C60 fullerene planar solar cells”. In: *RSC Advances* 4 (55 July 2014), pp. 28964–28967. ISSN: 2046-2069. DOI: 10.1039/C4RA03820G.

[33] Yanqing Zhu et al. “Bilayer metal halide perovskite for efficient and stable solar cells and modules”. In: *Materials Futures* 1 (4 Oct. 2022), p. 042102. ISSN: 2752-5724. DOI: 10.1088/2752-5724/AC9248.

[34] T. Moser et al. “Understanding the Formation Process of Perovskite Layers Grown by Chemical Vapour Deposition”. In: *Frontiers in Energy Research* 10 (June 2022), p. 883882. ISSN: 2296598X. DOI: 10.3389/FENRG.2022.883882/BIBTEX.

[35] Yanyu Deng et al. “Recent advances in Pb–Sn mixed perovskite solar cells”. In: *Journal of Energy Chemistry* 73 (Oct. 2022), pp. 615–638. ISSN: 2095-4956. DOI: 10.1016/J.JECHEM.2022.07.003.

[36] Rajapakshe Mudiyanselage Indrachapa Bandara et al. “Progress of Pb-Sn Mixed Perovskites for Photovoltaics: A Review”. In: *Energy & Environmental Materials* 5 (2 Apr. 2022), pp. 370–400. ISSN: 2575-0356. DOI: 10.1002/EEM2.12211.

[37] Witchaya Arpavate, Kamonchanok Roongraung, and Surawut Chuangchote. “Photochemical solid-state reactions”. In: *Green Sustainable Process for Chemical and Environmental Engineering and Science: Solid State Synthetic Methods* (Jan. 2021), pp. 189–203. DOI: 10.1016/B978-0-12-819720-2.00012-6.

[38] Michal Baranowski and Paulina Plochocka. “Excitons in Metal□Halide Perovskites”. In: *Advanced Energy Materials* 10 (26 July 2020). ISSN: 1614-6832. DOI: 10.1002/aenm.201903659.

[39] Stefaan De Wolf et al. “Organometallic Halide Perovskites: Sharp Optical Absorption Edge and Its Relation to Photovoltaic Performance”. In: *The Journal of Physical Chemistry Letters* 5 (6 Mar. 2014), pp. 1035–1039. ISSN: 1948-7185. DOI: 10.1021/jz500279b.

[40] Ming Shi et al. “Tuning the Optoelectronic Property of All□Inorganic Lead□Free Perovskite via Finely Microstructural Modulation for Photovoltaics”. In: *Small Methods* (May 2023). ISSN: 2366-9608. DOI: 10.1002/smtd.202300405.

[41] Zongqi Li et al. “Cost Analysis of Perovskite Tandem Photovoltaics”. In: *Joule* 2 (8 Aug. 2018). ISSN: 25424351. DOI: 10.1016/j.joule.2018.05.001.

[42] Pavel Čulík et al. “Design and Cost Analysis of 100 MW Perovskite Solar Panel Manufacturing Process in Different Locations”. In: *ACS Energy Letters* 7 (9 Sept. 2022), pp. 3039–3044. ISSN: 2380-8195. DOI: 10.1021/acsenergylett.2c01728.

[43] Fraunhofer ISE. *Solar Cell Development*. URL: https://www.ise.fraunhofer.de/en/key-topics/tandem-photovoltaics/solar-cell-development.html.

[44] Weiqiang Liao et al. “Fabrication of Efficient Low-Bandgap Perovskite Solar Cells by Combining Formamidinium Tin Iodide with Methylammonium Lead Iodide”. In: (2016). DOI: 10.1021/jacs.6b08337. URL: https://pubs.acs.org/sharingguidelines.

[45] Feng Hao et al. “Anomalous band gap behavior in mixed Sn and Pb perovskites enables broadening of absorption spectrum in solar cells”. In: *Journal of the American Chemical Society* 136 (22 June 2014), pp. 8094–8099. ISSN: 15205126. DOI: 10.1021/JA5033259/SUPPL_FILE/JA5033259_SI_001.PDF.

[46] Ziwei Zheng et al. “Development of formamidinium lead iodide-based perovskite solar cells: efficiency and stability”. In: *Chemical Science* 13 (8 Feb. 2022), pp. 2167–2183. ISSN: 20416539. DOI: 10.1039/D1SC04769H.

[47] Hanul Min et al. “Efficient, stable solar cells by using inherent bandgap of a-phase formamidinium lead iodide”. In: *Science* 366 (6466 Nov. 2019), pp. 749–753. ISSN: 10959203. DOI: 10.1126/SCIENCE.AAY7044/SUPPL_FILE/AAY7044-MIN-SM.PDF.

[48] Farhad Fouladi Targhi, Yousef Seyed Jalili, and Faramarz Kanjouri. “MAPbI3 and FAPbI3 perovskites as solar cells: Case study on structural, electrical and optical properties”. In: *Results in Physics* 10 (Sept. 2018), pp. 616–627. ISSN: 2211-3797. DOI: 10.1016/J.RINP.2018.07.007.

[49] Weijun Ke et al. “Diammonium Cations in the FASnI3 Perovskite Structure Lead to Lower Dark Currents and More Efficient Solar Cells”. In: *ACS Energy Letters* 3 (7 July 2018), pp. 1470–1476. ISSN: 23808195. DOI: 10.1021/ACSENERGYLETT.8B00687.

[50] Weijun Ke et al. ““Unleaded” Perovskites: Status Quo and Future Prospects of Tin-Based Perovskite Solar Cells”. In: *Advanced Materials* 31 (47 Nov. 2019), p. 1803230. ISSN: 1521-4095. DOI: 10.1002/ADMA.201803230.

[51] Qidong Tai et al. “Recent advances toward efficient and stable tin-based perovskite solar cells”. In: *EcoMat* 1 (1 Dec. 2019), e12004. ISSN: 2567-3173. DOI: 10.1002/EOM2.12004.

[52] Anuj Goyal et al. “Origin of Pronounced Nonlinear Band Gap Behavior in Lead–Tin Hybrid Perovskite Alloys”. In: *Chemistry of Materials* 30 (11 June 2018), pp. 3920–3928. ISSN: 0897-4756. DOI: 10.1021/acs.chemmater.8b01695.

[53] Mulmudi Hemant Kumar et al. “Lead-Free Halide Perovskite Solar Cells with High Photocurrents Realized Through Vacancy Modulation”. In: *Advanced Materials* 26 (41 Nov. 2014). ISSN: 09359648. DOI: 10.1002/adma.201401991.

[54] Kimberley J. Savill, Aleksander M. Ulatowski, and Laura M. Herz. “Optoelectronic Properties of Tin–Lead Halide Perovskites”. In: *ACS Energy Letters* 6 (7 July 2021). ISSN: 2380-8195. DOI: 10.1021/acsenergylett.1c00776.

[55] Matthew T. Klug et al. “Metal composition influences optoelectronic quality in mixed-metal lead–tin triiodide perovskite solar absorbers”. In: *Energy & Environmental Science* 13 (6 June 2020), pp. 1776–1787. ISSN: 1754-5706. DOI: 10.1039/D0EE00132E.

[56] Kimberley J. Savill et al. “Charge-Carrier Cooling and Polarization Memory Loss in Formamidinium Tin Triiodide”. In: *The journal of physical chemistry letters* 10 (20 Oct. 2019), pp. 6038–6047. ISSN: 1948-7185. DOI: 10.1021/ACS.JPCLETT.9B02353.

[57] Sachin Dev Verma et al. “Slow Carrier Cooling in Hybrid Pb-Sn Halide Perovskites”. In: *ACS Energy Letters* 4 (3 Mar. 2019), pp. 736–740. ISSN: 23808195. DOI: 10.1021/ACSENERGYLETT.9B00251.

[58] Mingjie Li et al. “Slow Hot-Carrier Cooling in Halide Perovskites: Prospects for Hot-Carrier Solar Cells”. In: *Advanced materials (Deerfield Beach, Fla.)* 31 (47 Nov. 2019). ISSN: 1521-4095. DOI: 10.1002/ADMA.201802486.

[59] James M. Ball et al. “Dual-Source Coevaporation of Low-Bandgap FA _{1– x} Cs _x Sn _{1– y} Pb _y I ₃ Perovskites for Photovoltaics”. In: *ACS Energy Letters* 4 (11 Nov. 2019). ISSN: 2380-8195. DOI: 10.1021/acsenergylett.9b01855.

[60] Rebecca L. Milot et al. “The Effects of Doping Density and Temperature on the Optoelectronic Properties of Formamidinium Tin Triiodide Thin Films”. In: *Advanced materials (Deerfield Beach, Fla.)* 30 (44 Nov. 2018). ISSN: 1521-4095. DOI: 10.1002/ADMA.201804506.

[61] Krzysztof Galkowski et al. “Excitonic Properties of Low-Band-Gap Lead-Tin Halide Perovskites”. In: *ACS Energy Letters* 4 (3 Mar. 2019), pp. 615–621. ISSN: 23808195. DOI: 10.1021/ACSENERGYLETT.8B02243.

[62] Bumseop Kim, Jeongwoo Kim, and Noejung Park. “First-principles identification of the charge-shifting mechanism and ferroelectricity in hybrid halide perovskites”. In: *Scientific Reports* 10 (1 Dec. 2020). ISSN: 20452322. DOI: 10.1038/S41598-020-76742-7.

[63] Tingting Niu et al. “Phase-Pure α-FAPbI3for Perovskite Solar Cells”. In: *Journal of Physical Chemistry Letters* 13 (7 Feb. 2022), pp. 1845–1854. ISSN: 19487185. DOI: 10.1021/ACS.JPCLETT.1C04241/ASSET/IMAGES/MEDIUM/JZ1C04241_0006.GIF.

[64] Byung wook Park et al. “Stabilization of formamidinium lead triiodide α-phase with isopropylammonium chloride for perovskite solar cells”. In: *Nature Energy 2021 6:4* 6 (4 Apr. 2021), pp. 419–428. ISSN: 2058-7546. DOI: 10.1038/s41560-021-00802-z.

[65] Yan Shao et al. “Unlocking surface octahedral tilt in two-dimensional Ruddlesden-Popper perovskites”. In: *Nature Communications 2022 13:1* 13 (1 Jan. 2022), pp. 1–10. ISSN: 2041-1723. DOI: 10.1038/s41467-021-27747-x.

[66] Zhen Li et al. “Stabilizing Perovskite Structures by Tuning Tolerance Factor: Formation of Formamidinium and Cesium Lead Iodide Solid-State Alloys”. In: *Chemistry of Materials* 28 (1 Jan. 2016), pp. 284–292. ISSN: 15205002. DOI: 10.1021/ACS.CHEMMATER.5B04107/SUPPL_FILE/CM5B04107_SI_001.PDF.

[67] Marina R. Filip and Feliciano Giustino. “The geometric blueprint of perovskites”. In: *Proceedings of the National Academy of Sciences of the United States of America* 115 (21 May 2018), pp. 5397–5402. ISSN: 10916490. DOI: 10.1073/PNAS.1719179115/SUPPL_FILE/PNAS.1719179115.SD06.PDF.

[68] Quanyao Lin et al. “The race between complicated multiple cation/anion compositions and stabilization of FAPbI ₃ for halide perovskite solar cells”. In: *Journal of Materials Chemistry C* 11 (7 2023), pp. 2449–2468. ISSN: 2050-7526. DOI: 10.1039/D2TC04529J.

[69] Miguel Anaya et al. “ABX3 Perovskites for Tandem Solar Cells”. In: *Joule* 1 (4 Dec. 2017), pp. 769–793. ISSN: 2542-4785. DOI: 10.1016/J.JOULE.2017.09.017.

[70] Min Seok Han et al. “Cesium Doping for Performance Improvement of Lead(II)-acetate-Based Perovskite Solar Cells”. In: *Materials* 14 (2 Jan. 2021), pp. 1–9. ISSN: 19961944. DOI: 10.3390/MA14020363.

[71] Gabriella A. Tosado et al. “Impact of cesium on the phase and device stability of triple cation Pb–Sn double halide perovskite films and solar cells”. In: *Journal of Materials Chemistry A* 6 (36 Sept. 2018), pp. 17426–17436. ISSN: 2050-7496. DOI: 10.1039/C8TA06391E.

[72] Hang Li et al. “Sequential vacuum-evaporated perovskite solar cells with more than 24% efficiency”. In: *Science Advances* 8 (28 July 2022). ISSN: 2375-2548. DOI: 10.1126/sciadv.abo7422.

[73] Atefeh Yadegarifard et al. “FA/Cs-based mixed Pb–Sn perovskite solar cells: A review of recent advances in stability and efficiency”. In: *Nano Energy* 112 (July 2023), p. 108481. ISSN: 2211-2855. DOI: 10.1016/J.NANOEN.2023.108481.

[74] Waldemar Kaiser et al. “Stability of Tin- versus Lead-Halide Perovskites: Ab Initio Molecular Dynamics Simulations of Perovskite/Water Interfaces”. In: *The Journal of Physical Chemistry Letters* 13 (10 Mar. 2022), pp. 2321–2329. ISSN: 1948-7185. DOI: 10.1021/acs.jpclett.2c00273.

[75] Laura E. Mundt et al. “Surface-Activated Corrosion in Tin-Lead Halide Perovskite Solar Cells”. In: *ACS Energy Letters* 5 (11 Nov. 2020), pp. 3344–3351. ISSN: 23808195. DOI: 10.1021/ACSENERGYLETT.0C01445.

[76] Tomas Leijtens et al. “Mechanism of Tin Oxidation and Stabilization by Lead Substitution in Tin Halide Perovskites”. In: *ACS Energy Letters* 2 (9 Sept. 2017), pp. 2159–2165. ISSN: 23808195. DOI: 10.1021/ACSENERGYLETT.7B00636.

[77] Azat F. Akbulatov et al. “Comparative Intrinsic Thermal and Photochemical Stability of Sn(II) Complex Halides as Next-Generation Materials for Lead-Free Perovskite Solar Cells”. In: *Journal of Physical Chemistry C* 123 (44 Nov. 2019), pp. 26862–26869. ISSN: 19327455. DOI: 10.1021/ACS.JPCC.9B09200.

[78] Francesco Ambrosio et al. “Composition-Dependent Struggle between Iodine and Tin Chemistry at the Surface of Mixed Tin/Lead Perovskites”. In: *ACS Energy Letters* 6 (3 Mar. 2021), pp. 969–976. ISSN: 23808195. DOI: 10.1021/ACSENERGYLETT.1C00111.

[79] Damiano Ricciarelli et al. “Instability of tin iodide perovskites: Bulk p-doping versus surface tin oxidation”. In: *ACS Energy Letters* 5 (9 Sept. 2020), pp. 2787–2795. ISSN: 23808195. DOI: 10.1021/ACSENERGYLETT.0C01174.

[80] Nakita K. Noel et al. “Lead-free organic–inorganic tin halide perovskites for photovoltaic applications”. In: *Energy & Environmental Science* 7 (9 Aug. 2014), pp. 3061–3068. ISSN: 1754-5706. DOI: 10.1039/C4EE01076K.

[81] Luis Lanzetta, Nicholas Aristidou, and Saif A. Haque. “Stability of Lead and Tin Halide Perovskites: The Link between Defects and Degradation”. In: *Journal of Physical Chemistry Letters* 11 (2 Jan. 2020), pp. 574–585. ISSN: 19487185. DOI: 10.1021/ACS.JPCLETT.9B02191.

[82] Luis Lanzetta et al. “Degradation mechanism of hybrid tin-based perovskite solar cells and the critical role of tin (IV) iodide”. In: *Nature communications* 12 (1 Dec. 2021). ISSN: 2041-1723. DOI: 10.1038/S41467-021-22864-Z.

[83] Rohit Prasanna et al. “Stability of Tin-Lead Halide Perovskite Solar Cells”. In: *Conference Record of the IEEE Photovoltaic Specialists Conference* (June 2019), pp. 2359–2361. ISSN: 01608371. DOI: 10.1109/PVSC40753.2019.8980810.

[84] Chaneui Park et al. “Suppression of Oxidative Degradation of Tin–Lead Hybrid Organometal Halide Perovskite Solar Cells by Ag Doping”. In: *ACS Energy Letters* 5 (10 Oct. 2020). ISSN: 2380-8195. DOI: 10.1021/acsenergylett.0c01648.

[85] Daniele Meggiolaro et al. “Tin versus Lead Redox Chemistry Modulates Charge Trapping and Self-Doping in Tin/Lead Iodide Perovskites”. In: *Journal of Physical Chemistry Letters* 11 (9 May 2020), pp. 3546–3556. ISSN: 19487185. DOI: 10.1021/ACS.JPCLETT.0C00725/SUPPL_FILE/JZ0C00725_SI_001.PDF.

[86] Yiting Jiang et al. “Dual-site passivation of tin-related defects enabling efficient lead-free tin perovskite solar cells”. In: *Nano Energy* 103 (Dec. 2022), p. 107818. ISSN: 2211-2855. DOI: 10.1016/J.NANOEN.2022.107818.

[87] Huanhuan Yao et al. “Strategies for Improving the Stability of Tin-Based Perovskite (ASnX3) Solar Cells”. In: *Advanced Science* 7 (10 May 2020), p. 1903540. ISSN: 2198-3844. DOI: 10.1002/ADVS.201903540.

[88] Jianhang Qiu et al. “Dark-blue mirror-like perovskite dense films for efficient organic-inorganic hybrid solar cells”. In: *Journal of Materials Chemistry A* 4 (10 2016), pp. 3689–3696. ISSN: 20507496. DOI: 10.1039/C5TA08772D.

[89] Wiley A. Dunlap-Shohl et al. “Synthetic Approaches for Halide Perovskite Thin Films”. In: *Chemical Reviews* 119 (5 Mar. 2019), pp. 3193–3295. ISSN: 15206890. DOI: 10.1021/ACS.CHEMREV.8B00318/ASSET/IMAGES/MEDIUM/CR-2018-00318H_0058.GIF.

[90] Shindume Lomboleni Hamukwaya et al. “A Review of Recent Developments in Preparation Methods for Large-Area Perovskite Solar Cells”. In: *Coatings 2022, Vol. 12, Page 252* 12 (2 Feb. 2022), p. 252. ISSN: 2079-6412. DOI: 10.3390/COATINGS12020252.

[91] Jincheol Kim et al. “Overcoming the Challenges of Large-Area High-Efficiency Perovskite Solar Cells”. In: *ACS Energy Letters* 2 (9 Sept. 2017), pp. 1978–1984. ISSN: 23808195. DOI: 10.102

1/ACSENERGYLETT.7B00573. URL: https://pubs.acs.org/doi/abs/10.1021/acsenergylett.7b00573.

[92] Antonio Agresti et al. “Scalable deposition techniques for large-area perovskite photovoltaic technology: A multi-perspective review”. In: *Nano Energy* 122 (Apr. 2024), p. 109317. ISSN: 2211-2855. DOI: 10.1016/J.NANOEN.2024.109317.

[93] Tatiana Soto-Montero, Wiria Soltanpoor, and Monica Morales-Masis. “Pressing challenges of halide perovskite thin film growth”. In: *APL Materials* 8 (11 Nov. 2020), p. 110903. ISSN: 2166532X. DOI: 10.1063/5.0027573/569855.

[94] Satyajit Gupta, David Cahen, and Gary Hodes. “How SnF2 Impacts the Material Properties of Lead-Free Tin Perovskites”. In: *Journal of Physical Chemistry C* 122 (25 June 2018), pp. 13926–13936. ISSN: 19327455. DOI: 10.1021/ACS.JPCC.8B01045.

[95] Teck Ming Koh et al. “Formamidinium tin-based perovskite with low Eg for photovoltaic applications”. In: *Journal of Materials Chemistry A* 3 (29 July 2015), pp. 14996–15000. ISSN: 2050-7496. DOI: 10.1039/C5TA00190K.

[96] Yue Yu et al. “Thermally evaporated methylammonium tin triiodide thin films for lead-free perovskite solar cell fabrication”. In: *RSC Advances* 6 (93 Sept. 2016), pp. 90248–90254. ISSN: 20462069. DOI: 10.1039/C6RA19476A.

[97] T Feeney et al. “From Groundwork to Efficient Solar Cells: On the Importance of the Substrate Material in Co-Evaporated Perovskite Solar Cells”. In: *Advanced Functional Materials* 31 (42 Oct. 2021), p. 2104482. ISSN: 1616-3028. DOI: 10.1002/ADFM.202104482.

[98] Jingjing Liu et al. “Crystalline quality control in sequential vapor deposited perovskite film toward high efficiency and large scale solar cells”. In: *Solar Energy Materials and Solar Cells* 233 (Dec. 2021), p. 111382. ISSN: 0927-0248. DOI: 10.1016/J.SOLMAT.2021.111382.

[99] Weijie Chen et al. “A Semitransparent Inorganic Perovskite Film for Overcoming Ultraviolet Light Instability of Organic Solar Cells and Achieving 14.03% Efficiency”. In: *Advanced Materials* 30 (21 May 2018), p. 1800855. ISSN: 1521-4095. DOI: 10.1002/ADMA.201800855.

[100] G Carter. “Preferred orientation in thin film growth — the survival of the fastest model”. In: *Vacuum* 56 (2 Feb. 2000), pp. 87–93. ISSN: 0042207X. DOI: 10.1016/S0042-207X(99)00171-2.

[101] Long Luo et al. “19.59% Efficiency from Rb0.04-Cs0.14FA0.86Pb(BryI1−y)3 perovskite solar cells made by vapor–solid reaction technique”. In: *Science Bulletin* 66 (10 May 2021), pp. 962–964. ISSN: 2095-9273. DOI: 10.1016/J.SCIB.2021.01.031.

[102] Lyubov A. Frolova et al. “Highly efficient all-inorganic planar heterojunction perovskite solar cells produced by thermal coevaporation of CsI and PbI2”. In: *Journal of Physical Chemistry Letters* 8 (1 Jan. 2017), pp. 67–72. ISSN: 19487185. DOI: 10.1021/ACS.JPCLETT.6B02594/SUPPL_FILE/JZ6B02594_SI_001.PDF.

[103] Oleksandra Shargaieva et al. “Influence of the Grain Size on the Properties of CH3NH3PbI3 Thin Films”. In: *ACS Applied Materials and Interfaces* 9 (44 Nov. 2017), pp. 38428–38435. ISSN: 19448252. DOI: 10.1021/ACSAMI.7B10056/ASSET/IMAGES/MEDIUM/AM-2017-10056B_0008.GIF.

[104] Vanessa L. Pool et al. “Thermal engineering of FAPbI3 perovskite material via radiative thermal annealing and in situ XRD”. In: *Nature Communications 2017 8:1* 8 (1 Jan. 2017), pp. 1–8. ISSN: 2041-1723. DOI: 10.1038/ncomms14075.

[105] Tsutomu Miyasaka et al. “Perovskite Solar Cells: Can We Go Organic-Free, Lead-Free, and Dopant-Free?” In: *Advanced Energy Materials* 10 (13 Apr. 2020), p. 1902500. ISSN: 1614-6840. DOI: 10.1002/AENM.201902500.

[106] Julian A. Steele et al. “Phase Transitions and Anion Exchange in All-Inorganic Halide Perovskites”. In: *Accounts of Materials Research* 1 (1 Oct. 2020), pp. 3–15. ISSN: 26436728. DOI: 10.1021/ACCOUNTSMR.0C00009/ASSET/IMAGES/MEDIUM/MR0C00009_0007.GIF.

[107] Maryline Ralaiarisoa et al. “Correlation of annealing time with crystal structure, composition, and electronic properties of CH3NH3PbI3−xClx mixed-halide perovskite films”. In: *Physical Chemistry Chemical Physics* 19 (1 Dec. 2016), pp. 828–836. ISSN: 1463-9084. DOI: 10.1039/C6CP06347K.

[108] Ashish Dubey et al. “Room temperature, air crystallized perovskite film for high performance solar cells”. In: *Journal of Materials Chemistry A* 4 (26 June 2016), pp. 10231–10240. ISSN: 2050-7496. DOI: 10.1039/C6TA02918C.

[109] Lung Chien Chen et al. “Annealing Effect on (FAPbI3)1−x(MAPbBr3)x Perovskite Films in Inverted-Type Perovskite Solar Cells”. In: *Materials 2016, Vol. 9, Page 747* 9 (9 Sept. 2016), p. 747. ISSN: 1996-1944. DOI: 10.3390/MA9090747.

[110] Ping Fan et al. “High-performance perovskite CH3NH3PbI3 thin films for solar cells prepared by single-source physical vapour deposition”. In: *Scientific Reports 2016 6:1* 6 (1 July 2016), pp. 1–9. ISSN: 2045-2322. DOI: 10.1038/srep29910.

[111] Tatiana Soto-Montero et al. “Single-Source Vapor-Deposition of MA1–xFAxPbI3 Perovskite Absorbers for Solar Cells”. In: *Advanced Functional Materials* (2023), p. 2300588. ISSN: 1616-3028. DOI: 10.1002/ADFM.202300588.

[112] T Kuku. “Transport properties of PbSnI4”. In: *Solid State Ionics* 31 (1 Oct. 1988), pp. 73–78. ISSN: 01672738. DOI: 10.1016/0167-2738(88)90289-5.

[113] T. A. Kuku. “Ion transport studies on vacuum deposited PbSnI4 thin films”. In: *Thin Solid Films* 340 (1-2 Feb. 1999), pp. 292–296. ISSN: 0040-6090. DOI: 10.1016/S0040-6090(98)00869-4.

[114] Dhanashree Moghe et al. “All vapor-deposited lead-free doped CsSnBr3 planar solar cells”. In: *Nano Energy* 28 (Oct. 2016), pp. 469–474. ISSN: 2211-2855. DOI: 10.1016/J.NANOEN.2016.09.009.

[115] Ana M. Igual-Muñoz et al. “Vacuum-Deposited Multication Tin–Lead Perovskite Solar Cells”. In: *ACS Applied Energy Materials* 3 (3 Mar. 2020). ISSN: 2574-0962. DOI: 10.1021/acsaem.9b02413.

[116] Hui-Jie Yan et al. “Annealing temperature effects on the performance of the perovskite solar cells”. In: *IOP Conference Series: Materials Science and Engineering* 757 (1 Mar. 2020), p. 012039. ISSN: 1757-899X. DOI: 10.1088/1757-899X/757/1/012039.

[117] D. O. Oyewole et al. “Annealing effects on interdiffusion in layered FA-rich perovskite solar cells”. In: *AIP Advances* 11 (6 June 2021), p. 65327. ISSN: 21583226. DOI: 10.1063/5.0046205/995307.

[118] Amalie Dualeh et al. “Effect of Annealing Temperature on Film Morphology of Organic–Inorganic Hybrid Pervoskite Solid□State Solar Cells”. In: *Advanced Functional Materials* 24 (21 June 2014), pp. 3250–3258. ISSN: 1616-301X. DOI: 10.1002/adfm.201304022.

[119] Yuhang Liu et al. “Stabilization of Highly Efficient and Stable Phase□Pure FAPbI ₃ Perovskite Solar Cells by Molecularly Tailored 2D□Overlayers”. In: *Angewandte Chemie International Edition* 59 (36 Sept. 2020), pp. 15688–15694. ISSN: 1433-7851. DOI: 10.1002/anie.202005211.

[120] Yong Zhang et al. “Achieving Reproducible and High-Efficiency Perovskite Solar Cells with a Presynthesized FAPbI3 Powder”. In: *ACS Energy Letters* 5 (2 Feb. 2020), pp. 360–366. ISSN: 2380-8195. DOI: 10.1021/acsenergylett.9b02348.

[121] Wikimedia Commons Hadmack M. *Bragg diffraction*. 2006. URL: https://commons.wikimedia.org/wiki/File:Bragg_diffraction.png.

[122] Cameron F. Holder and Raymond E. Schaak. “Tutorial on Powder X-ray Diffraction for Characterizing Nanoscale Materials”. In: *ACS Nano* 13.7 (2019), pp. 7359–7365. DOI: 10.1021/acsnano.9b05157.

[123] Mojtaba Abdi-Jalebi et al. *Chapter 3 - Optical absorption and photoluminescence spectroscopy*. Ed. by Meysam Pazoki, Anders Hagfeldt, and Tomas Edvinsson. Micro and Nano Technologies. Elsevier, 2020, pp. 49–79. ISBN: 978-0-12-814727-6. DOI: https://doi.org/10.1016/B978-0-12-814727-6.00003-7.

[124] Hutter Eline. “Revealing the Fate of Photo-Generated Charges in Metal Halide Perovskites”. In: (June 2018).

[125] Patrycja Makuła, Michał Pacia, and Wojciech Macyk. “How To Correctly Determine the Band Gap Energy of Modified Semiconductor Photocatalysts Based on UV-Vis Spectra”. In: *Journal of Physical Chemistry Letters* 9 (23 Dec. 2018), pp. 6814–6817. ISSN: 19487185. DOI: 10.1021/ACS.JPCLETT.8B02892.

[126] V.M. Caselli. “Revealing loss and degradation mechanisms in metal halide perovskite solar cells: The role of defects and trap states”. PhD thesis. 2022. DOI: 10.4233/UUID:F8361576-F35D-4334-8BEE-68A48ED70037.

[127] Jim Koning. “Computational Modelling of a Resonant Microwave Cavity”. In: (July 2023).

[128] Wikimedia Commons Claudionico. *Electron Interaction with Matter*. 2013. URL: https://commons.wikimedia.org/wiki/File:Electron_Interaction_with_Matter.svg.

[129] The Surface Science Society of Japan. “Compendium of Surface and Interface Analysis”. In: *Compendium of Surface and Interface Analysis* (2018). DOI: 10.1007/978-981-10-6156-1.

[130] Antonis Nanakoudis. *Scanning Electron Microscopy - SEM - Advancing Materials*. Nov. 2019. URL: https://www.thermofisher.com/blog/materials/what-is-sem-scanning-electron-microscopy-explained/.

[131] S. Tougaard. *SURFACE ANALYSIS X-Ray Photoelectron Spectroscopy*. Ed. by Paul Worsfold, Alan Townshend, and Colin Poole. Second Edition. Oxford: Elsevier, 2005, pp. 446–456. ISBN: 978-0-12-369397-6. DOI: https://doi.org/10.1016/B0-12-369397-7/00589-6.

[132] Michael Huff. “Review Paper: Residual Stresses in Deposited Thin-Film Material Layers for Micro- and Nano-Systems Manufacturing”. In: *Micromachines* 13 (12 Nov. 2022), p. 2084. ISSN: 2072-666X. DOI: 10.3390/mi13122084.

[133] S Tamulevičius. “Stress and strain in the vacuum deposited thin films”. In: *Vacuum* 51 (2 Oct. 1998), pp. 127–139. ISSN: 0042207X. DOI: 10.1016/S0042-207X(98)00145-6.

[134] Jintara Padchasri and Rattikorn Yimnirun. “Effects of annealing temperature on stability of methylammonium lead iodide perovskite powders”. In: *Journal of Alloys and Compounds* 720 (Oct. 2017), pp. 63–69. ISSN: 09258388. DOI: 10.1016/j.jallcom.2017.05.170.

[135] Bin□Bin Yu et al. “Heterogeneous 2D/3D Tin□Halides Perovskite Solar Cells with Certified Conversion Efficiency Breaking 14%”. In: *Advanced Materials* 33 (36 Sept. 2021). ISSN: 0935-9648. DOI: 10.1002/adma.202102055.

[136] Cheng-Min Tsai et al. “Role of Tin Chloride in Tin-Rich Mixed-Halide Perovskites Applied as Mesoscopic Solar Cells with a Carbon Counter Electrode”. In: *ACS Energy Letters* 1 (6 Dec. 2016), pp. 1086–1093. ISSN: 2380-8195. DOI: 10.1021/acsenergylett.6b00514.

[137] Renxing Lin et al. “Monolithic all-perovskite tandem solar cells with 24.8% efficiency exploiting comproportionation to suppress Sn(ii) oxidation in precursor ink”. In: *Nature Energy* 4 (10 Sept. 2019), pp. 864–873. ISSN: 2058-7546. DOI: 10.1038/s41560-019-0466-3.

[138] Xiao Liu et al. “Improved efficiency and stability of Pb–Sn binary perovskite solar cells by Cs substitution”. In: *Journal of Materials Chemistry A* 4 (46 2016), pp. 17939–17945. ISSN: 2050-7488. DOI: 10.1039/C6TA07712A.

[139] Guoming Lin et al. “Novel exciton dissociation behavior in tin-lead organohalide perovskites”. In: *Nano Energy* 27 (Sept. 2016), pp. 638–646. ISSN: 22112855. DOI: 10.1016/j.nanoen.2016.08.015.

[140] Lan Wang et al. “Annealing Engineering in the Growth of Perovskite Grains”. In: *Crystals* 12 (7 June 2022), p. 894. ISSN: 2073-4352. DOI: 10.3390/cryst12070894.

[141] Xin Guo et al. “Identification and characterization of the intermediate phase in hybrid organic–inorganic MAPbI3 perovskite”. In: *Dalton Transactions* 45 (9 2016), pp. 3806–3813. ISSN: 1477-9226. DOI: 10.1039/C5DT04420K.

[142] Kimberley J. Savill et al. “Impact of Tin Fluoride Additive on the Properties of Mixed Tin-Lead Iodide Perovskite Semiconductors”. In: *Advanced Functional Materials* 30 (52 Dec. 2020), p. 2005594. ISSN: 1616-3028. DOI: 10.1002/ADFM.202005594.

[143] Jinhui Tong et al. “Carrier lifetimes of >1 μs in Sn-Pb perovskites enable efficient all-perovskite tandem solar cells”. In: *Science (New York, N.Y.)* 364 (6439 2019), pp. 475–479. ISSN: 1095-9203. DOI: 10.1126/SCIENCE.AAV7911.

[144] Alan R. Bowman et al. “Microsecond Carrier Lifetimes, Controlled p-Doping, and Enhanced Air Stability in Low-Bandgap Metal Halide Perovskites”. In: *ACS Energy Letters* 4 (9 Sept. 2019), pp. 2301–2307. ISSN: 23808195. DOI: 10.1021/ACSENERGYLETT.9B01446.

[145] Dianxing Ju et al. “Tunable Band Gap and Long Carrier Recombination Lifetime of Stable Mixed CH3NH3PbxSn1- xBr3 Single Crystals”. In: *Chemistry of Materials* 30 (5 Mar. 2018), pp. 1556–1565. ISSN: 15205002. DOI: 10.1021/ACS.CHEMMATER.7B04565.

[146] Rohit Prasanna et al. “Band Gap Tuning via Lattice Contraction and Octahedral Tilting in Perovskite Materials for Photovoltaics”. In: *Journal of the American Chemical Society* 139 (32 Aug. 2017), pp. 11117–11124. ISSN: 15205126. DOI: 10.1021/JACS.7B04981.

[147] Christopher J. Bartel et al. “New tolerance factor to predict the stability of perovskite oxides and halides”. In: *Science Advances* 5 (2 Feb. 2019). ISSN: 2375-2548. DOI: 10.1126/sciadv.aav0693.

[148] Bethan Charles et al. “Understanding the stability of mixed A-cation lead iodide perovskites”. In: *Journal of Materials Chemistry A* 5 (43 Nov. 2017), pp. 22495–22499. ISSN: 20507496. DOI: 10.1039/C7TA08617B.

[149] W. Travis et al. “On the application of the tolerance factor to inorganic and hybrid halide perovskites: a revised system”. In: *Chemical Science* 7 (7 June 2016), pp. 4548–4556. ISSN: 2041-6539. DOI: 10.1039/C5SC04845A. URL: https://pubs.rsc.org/en/content/articlehtml/2016/sc/c5sc04845a%20https://pubs.rsc.org/en/content/articlelanding/2016/sc/c5sc04845a.

[150] Zhaohua Zhu et al. “Metal halide perovskites: stability and sensing-ability”. In: *Journal of Materials Chemistry C* 6 (38 2018), pp. 10121–10137. ISSN: 20507526. DOI: 10.1039/C8TC03164A.

[151] Qingde Sun and Wan Jian Yin. “Thermodynamic Stability Trend of Cubic Perovskites”. In: *Journal of the American Chemical Society* 139 (42 Oct. 2017), pp. 14905–14908. ISSN: 15205126. DOI: 10.1021/JACS.7B09379/SUPPL_FILE/JA7B09379_SI_001.PDF.

[152] Hyosung Choi et al. “Cesium-doped methylammonium lead iodide perovskite light absorber for hybrid solar cells”. In: *Nano Energy* 7 (July 2014), pp. 80–85. ISSN: 2211-2855. DOI: 10.1016/J.NANOEN.2014.04.017.

[153] Azadeh Farzaneh et al. “The preparation of cesium-iodide thin films via sol–gel method for the detection of ionizing radiation”. In: *Journal of Sol-Gel Science and Technology* 78 (2 May 2016), pp. 313–321. ISSN: 0928-0707. DOI: 10.1007/s10971-016-3959-6.

[154] Bo Li et al. “Surface passivation engineering strategy to fully-inorganic cubic CsPbI3 perovskites for high-performance solar cells”. In: *Nature Communications 2018 9:1* 9 (1 Mar. 2018), pp. 1–8. ISSN: 2041-1723. DOI: 10.1038/s41467-018-03169-0.

[155] Shuai Gu et al. “Thermal-stable mixed-cation lead halide perovskite solar cells”. In: *Chinese Optics Letters, Vol. 15, Issue 9, pp. 093501* - 15 (9 July 2018), p. 093501. ISSN: 1671-7694. DOI: 10.3788/COL201715.093501.

[156] Guangda Niu et al. “Enhancement of thermal stability for perovskite solar cells through cesium doping”. In: *RSC Advances* 7 (28 Mar. 2017), pp. 17473–17479. ISSN: 2046-2069. DOI: 10.1039/C6RA28501E.

[157] Adharsh Rajagopal et al. “On understanding bandgap bowing and optoelectronic quality in Pb–Sn alloy hybrid perovskites”. In: *Journal of Materials Chemistry A* 7 (27 2019), pp. 16285–16293. ISSN: 2050-7488. DOI: 10.1039/C9TA05308E.

[158] Somayeh Gholipour and Michael Saliba. “Bandgap tuning and compositional exchange for lead halide perovskite materials”. In: Elsevier, 2020, pp. 1–22. DOI: 10.1016/B978-0-12-814727-6.00001-3.

[159] Haizhou Lu et al. “Compositional and Interface Engineering of Organic-Inorganic Lead Halide Perovskite Solar Cells”. In: *iScience* 23 (8 Aug. 2020), p. 101359. ISSN: 25890042. DOI: 10.1016/j.isci.2020.101359.

[160] R. Thandaiah Prabu et al. “Bandgap Assessment of Compositional Variation for Uncovering High-Efficiency Improved Stable All-Inorganic Lead-Free Perovskite Solar Cells”. In: *physica status solidi (a)* 220 (6 Mar. 2023), p. 2200791. ISSN: 1862-6319. DOI: 10.1002/PSSA.202200791.

[161] Keith T. Butler. “The chemical forces underlying octahedral tilting in halide perovskites”. In: *Journal of Materials Chemistry C* 6 (44 Nov. 2018), pp. 12045–12051. ISSN: 2050-7534. DOI: 10.1039/C8TC02976H.

[162] Johnpaul Kurisinkal Pious et al. “Revealing the Role of Tin Fluoride Additive in Narrow Bandgap Pb-Sn Perovskites for Highly Efficient Flexible All-Perovskite Tandem Cells”. In: *ACS Applied Materials & Interfaces* 15 (7 Feb. 2023), pp. 10150–10157. ISSN: 1944-8244. DOI: 10.1021/acsami.2c19124.

[163] Hongki Kim et al. “Synergistic Effects of Cation and Anion in an Ionic Imidazolium Tetrafluoroborate Additive for Improving the Efficiency and Stability of Half-Mixed Pb-Sn Perovskite Solar Cells”. In: *Advanced Functional Materials* 31 (11 Mar. 2021), p. 2008801. ISSN: 1616-3028. DOI: 10.1002/ADFM.202008801.

[164] Chongwen Li et al. “Low-bandgap mixed tin–lead iodide perovskites with reduced methylammonium for simultaneous enhancement of solar cell efficiency and stability”. In: *Nature Energy 2020 5:10* 5 (10 Oct. 2020), pp. 768–776. ISSN: 2058-7546. DOI: 10.1038/s41560-020-00692-7.

[165] Nabin Ghimire et al. “Mitigating Open-Circuit Voltage Loss in Pb-Sn Low-Bandgap Perovskite Solar Cells via Additive Engineering”. In: *ACS Applied Energy Materials* 4 (2 Feb. 2021), pp. 1731–1742. ISSN: 25740962. DOI: 10.1021/ACSAEM.0C02895.

[166] Yulong Zhang et al. “Moisture assisted CsPbBr3 film growth for high-efficiency, all-inorganic solar cells prepared by a multiple sequential vacuum deposition method”. In: *Materials Science in Semiconductor Processing* 98 (Aug. 2019), pp. 39–43. ISSN: 1369-8001. DOI: 10.1016/J.MSSP.2019.03.021.

[167] Kuifeng Jia et al. “Improved Performance for Thermally Evaporated Perovskite Light-Emitting Devices via Defect Passivation and Carrier Regulation”. In: *ACS Applied Materials and Interfaces* 12 (13 Apr. 2020), pp. 15928–15933. ISSN: 19448252. DOI: 10.1021/ACSAMI.0C01173.

[168] Zhurong Liang et al. “A large grain size perovskite thin film with a dense structure for planar heterojunction solar cells via spray deposition under ambient conditions”. In: *RSC Advances* 5 (74 July 2015), pp. 60562–60569. ISSN: 2046-2069. DOI: 10.1039/C5RA09110A.

[169] Jin-Wook Lee et al. “The role of grain boundaries in perovskite solar cells”. In: *Materials Today Energy* (2017). DOI: 10.1016/j.mtener.2017.07.014.

[170] Zhaodong Chu et al. “Impact of grain boundaries on efficiency and stability of organic-inorganic trihalide perovskites”. In: *Nature Communications 2017 8:1* 8 (1 Dec. 2017), pp. 1–8. ISSN: 2041-1723. DOI: 10.1038/s41467-017-02331-4.

[171] Lucie McGovern et al. “Grain Size Influences Activation Energy and Migration Pathways in MAPbBr3Perovskite Solar Cells”. In: *Journal of Physical Chemistry Letters* 12 (9 Mar. 2021), pp. 2423–2428. ISSN: 19487185. DOI: 10.1021/ACS.JPCLETT.1C00205.

[172] Qimu Yuan et al. “Thermally Stable Perovskite Solar Cells by All-Vacuum Deposition”. In: *ACS Applied Materials and Interfaces* 15 (1 2023), pp. 772–781. ISSN: 19448252. DOI: 10.1021/ACSAMI.2C14658.

[173] Xiaobing Cao et al. “High annealing temperature induced rapid grain coarsening for efficient perovskite solar cells”. In: *Journal of Colloid and Interface Science* 524 (Aug. 2018), pp. 483–489. ISSN: 0021-9797. DOI: 10.1016/J.JCIS.2018.04.019.

A

APPENDIX A: $PBSNI_4$ ALLOY

XRD Spectra

$PbSnI_4$ Powder

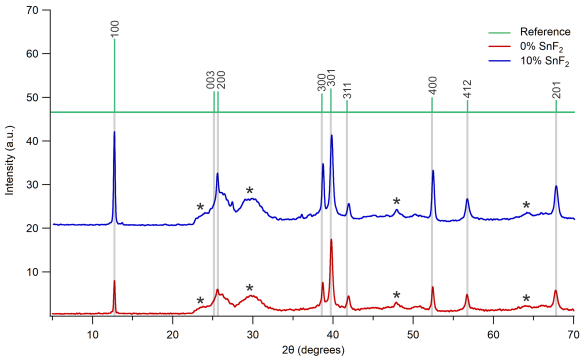

Figure A.1: Powder XRD of $PbSnI_4$ (red) and $PbSnI_4$+10% SnF_2 (blue) measured on monocrystalline silicon substrate at ambient conditions. Reference peaks of $PbSnI_4$ (green) were reproduced from Kuku et al.(1988).[112]

RESEARCH INTO THE BROAD PEAKS OBSERVED IN THE POWDER XRD OF $PBSNI_4$

The two broad peaks located at approximately 24 and 29 degrees were observed in one source, showing an XRD of a PbI_2 single crystal: https://www.hqgraphene.com/PbI2.php. The peaks in the spectrum are not labelled, although the supporting EDS spectrum shows Pb and I, with an atomic ratio of 1:2. Additional unfitted peaks are present at the <1 keV region, which is associated with the elements C, N and O. Although the oxygen peak is small compared to the Pb and I peak, the relative light weight of oxygen versus lead and iodide means that there are significant amounts of oxygen present. This makes PbI_2 and PbO likely candidates for the first two broad peaks.

When taking the third and fourth peaks into account, located at approx. 48 and 68 degrees, SnO forms a perfect match. SnO is readily formed from SnI_2 upon contact with oxygen and water via the following reaction equations:

$$SnI_2(s) + H_2O(g) + SnO(s) + 2\,HI(g)$$

$$2\,SnI_2(s) + O_2(g) + 2\,SnO(s) + I_2(g)$$

$PbSnI_4$ Thin Films (post-deposition)

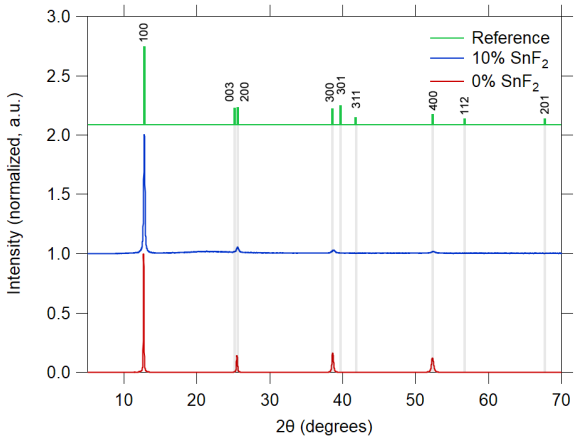

Figure A.2: XRD of $PbSnI_4$ (red) and $PbSnI_4$+10% SnF_2 (blue) thin films (after deposition) measured at ambient conditions. Reference peaks of $PbSnI_4$ (green) were reproduced from Kuku et al.(1988).[112]

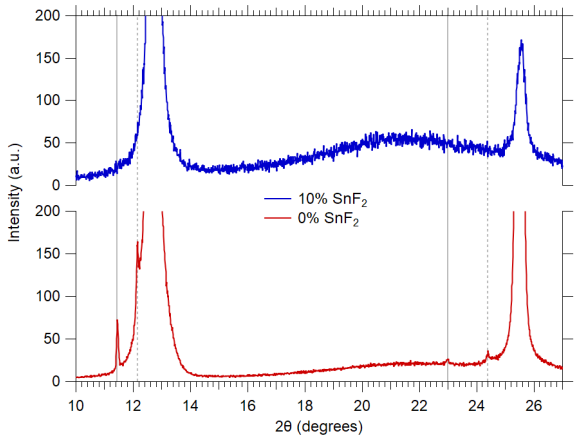

Figure A.3: Zoomed XRD of $PbSnI_4$ (red) and $PbSnI_4$+10% SnF_2 (blue) thin films (after deposition) measured at ambient conditions showing four minor peaks (two reflections).

1st Solid grey line at 11.45 translates to a d-spacing of 3.882 A (n=1) or 7.763 A (n=2)
2nd Solid grey line at 22.99 translates to a d-spacing of 3.945 A (n=2) or 7.889 A (n=4)
1st Dotted grey line at 12.16 translates to a d-spacing of 3.658 A (n=1) or 7.315 A (n=2)
2nd Dotted grey line at 24.40 translates to a d-spacing of 3.723 A (n=2) or 7.459 A (n=4)
SnI2 (monoclinic) a=4.49, b=7.61, c=11.10
PbI2 (trigonal) a=4.61, b=4.62, c=7.26
PbI2 (hexagonal) a=4.62, b=4.62, c=14.55
SnI4(cubic) a=6.36
SnO (triclinic) a=11.34, b=12.20, c=12.54
SnO(orthorhombic) a=5.47, b =5.48, c=10.2
SnO(tetragonal) a=3.28, b= 3.28, c= 3.05
PbO(orthorhombic) a=4.73, b=5.62, c=6.10
PbO(tetragonal) a=4.00, b=4.00, c=5.26
PbIO(orthorhombic) a=3.59, b=8.24, c=11.41

B

APPENDIX B: OPTIMIZING ANNEALING TEMPERATURE

B.1. Appendix B1: $FAPb_{0.5}Sn_{0.5}I_3$

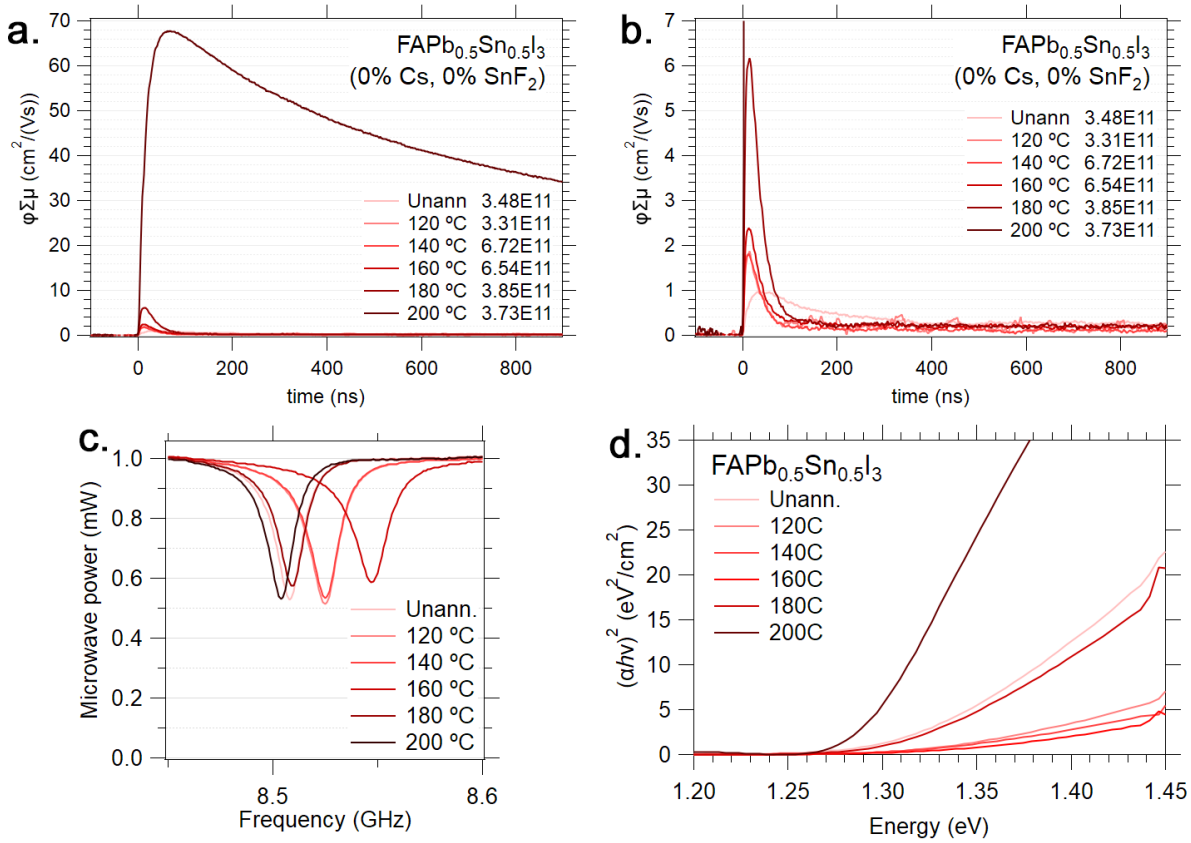

Figure B.1: a. TRMC plot of $FAPb_{0.5}Sn_{0.5}I_3$ annealing trend **b.** with magnification to show lower annealing temperatures. Traces were selected based on having similar fluencies. Note: due to differences in absorption not all samples were measured in the same fluency range.

Table B.1: Table showing film thickness as measured using stylus profilometry versus annealing temperature in $FAPb_{0.5}Sn_{0.5}I_3$.

Annealing T (C)	Unnann.	120	140	160	180	200
Thickness (nm)	175.21 ± 9.43	180.62 ± 7.95	176.03 ± 15.91	165.24 ± 10.17	159.84 ± 4.39	145.24 ± 8.07

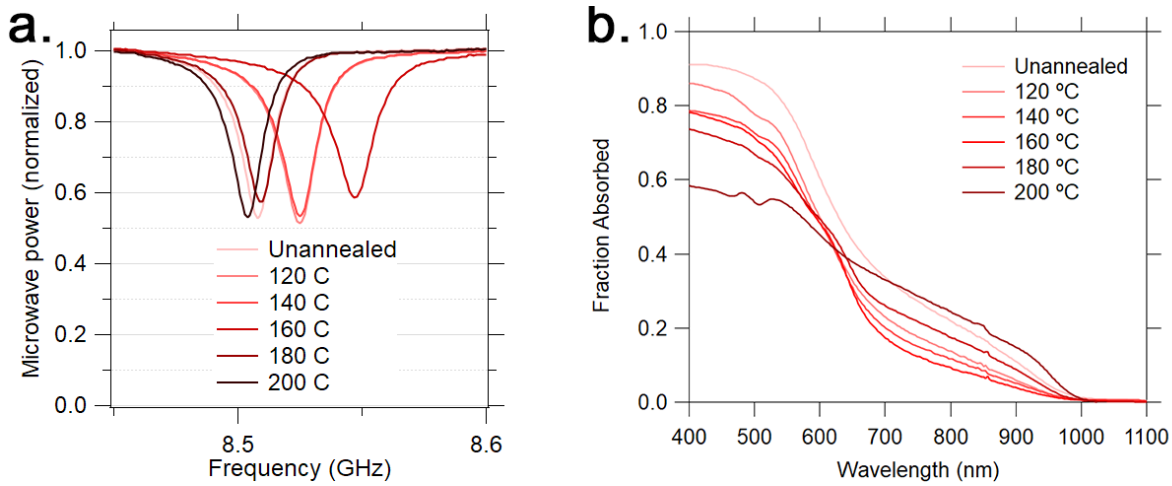

Figure B.2: a. SSMC plot of $FAPb_{0.5}Sn_{0.5}I_3$ annealing trend. The position of f_0 is shifted due to differences in substrate dimensions. **b.** Shows a UV-Vis-NIR absorption spectrum of the $FAPb_{0.5}Sn_{0.5}I_3$ annealing trend. The figure was not normalized for thickness.

B.2. Appendix B2: $Cs_{0.05}FA_{0.75}Pb_{0.5}Sn_{0.5}I_3$

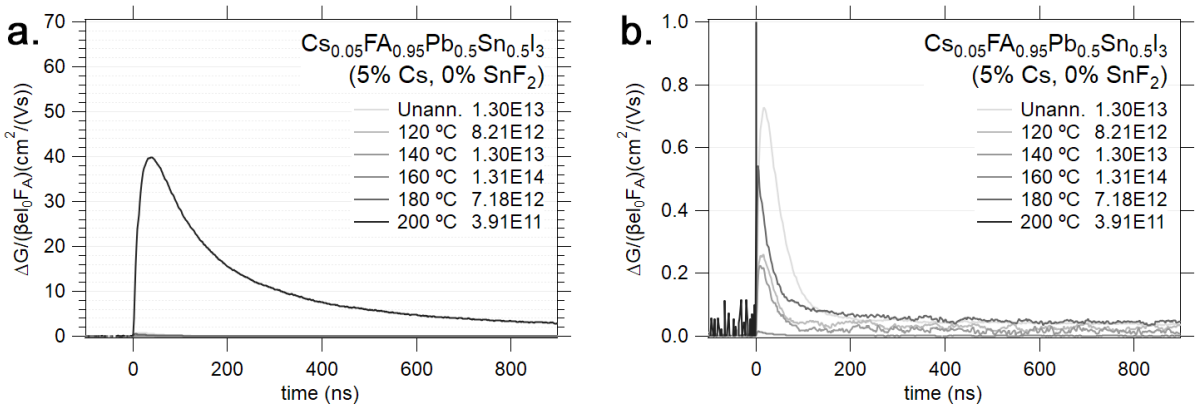

Figure B.3: a. TRMC of $Cs_{0.05}FA_{0.75}Pb_{0.5}Sn_{0.5}I_3$ annealing trend **b.** with magnification to show lower annealing temperatures. Traces were selected based on having similar fluencies. Note: due to differences in absorption not all samples were measured in the same fluency range.

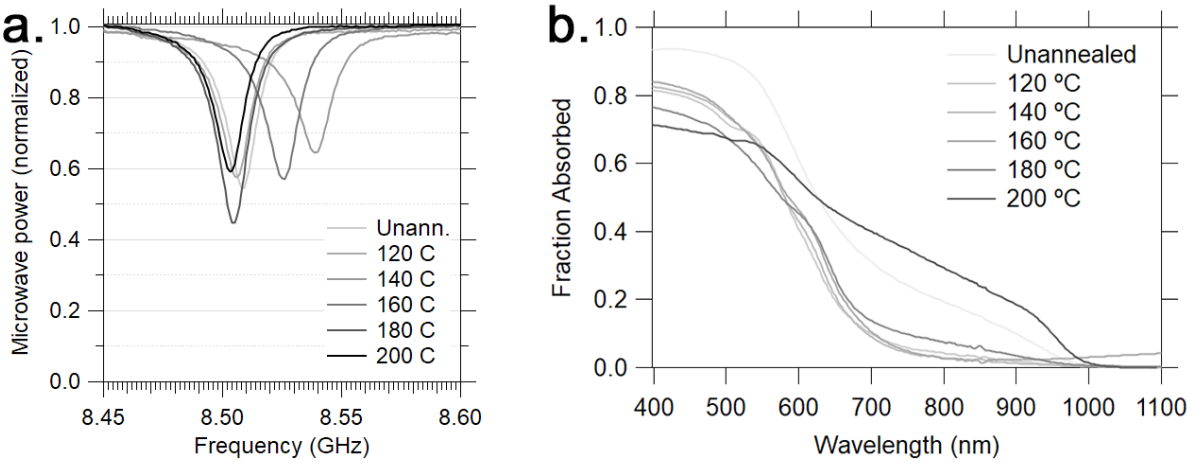

Figure B.4: a. SSMC plot of $Cs_{0.05}FA_{0.75}Sn_{0.5}I_3$ annealing trend. The position of f_0 is shifted due to differences in substrate dimensions. **b.** Shows a UV-Vis-NIR absorption spectrum of the $Cs_{0.05}FA_{0.75}Pb_{0.5}Sn_{0.5}I_3$ annealing trend. The figure was not normalized for thickness.

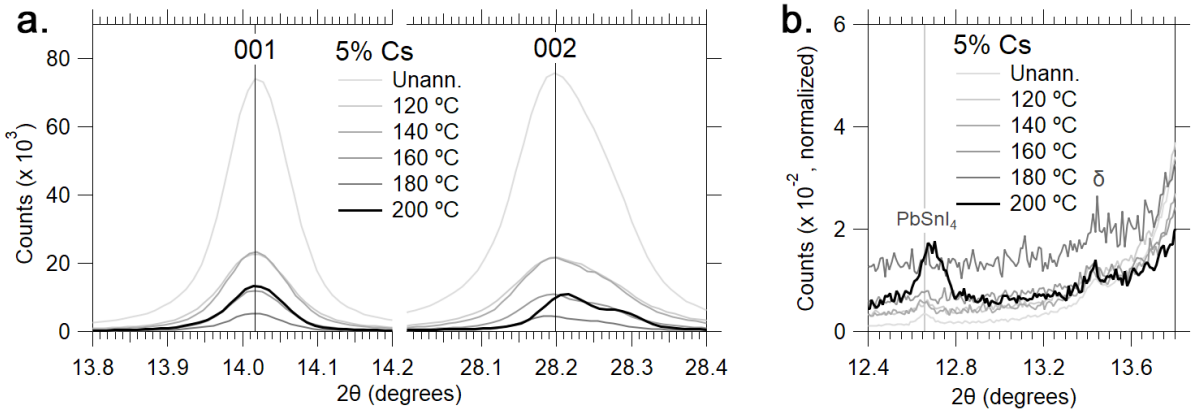

Figure B.5: XRD plots of the **a.** 001 and 002 peaks and **b.** excess precursor and δ phase of the $Cs_{0.05}FA_{0.75}Pb_{0.5}Sn_{0.5}I_3$ annealing trend.

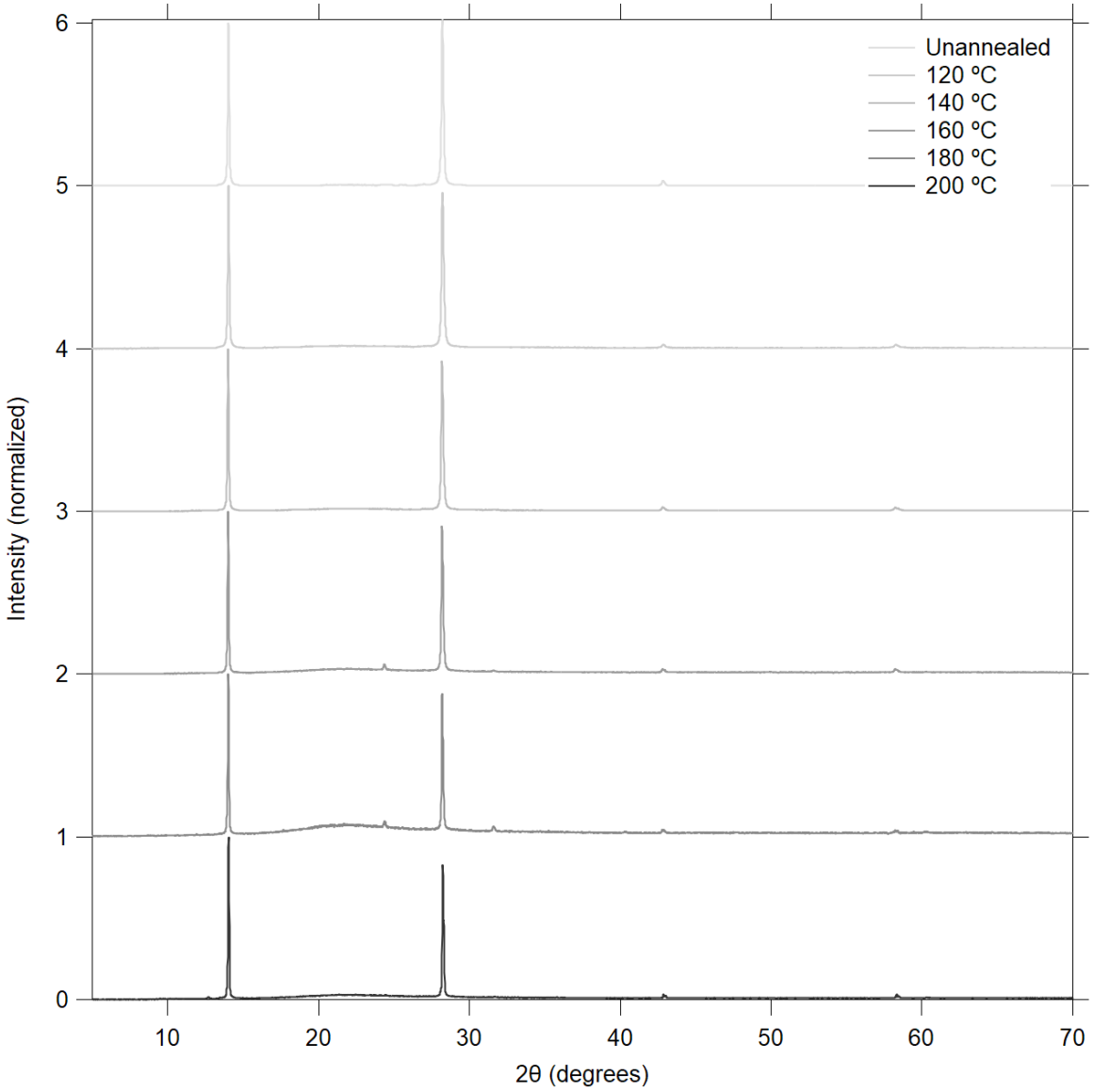

Figure B.6: Full XRD spectra of the $Cs_{0.05}FA_{0.75}Pb_{0.5}Sn_{0.5}I_3$ annealing trend. Note the increase in $PbSnI_4$ phase at 200 °C and the presence of only the H00 orientations.

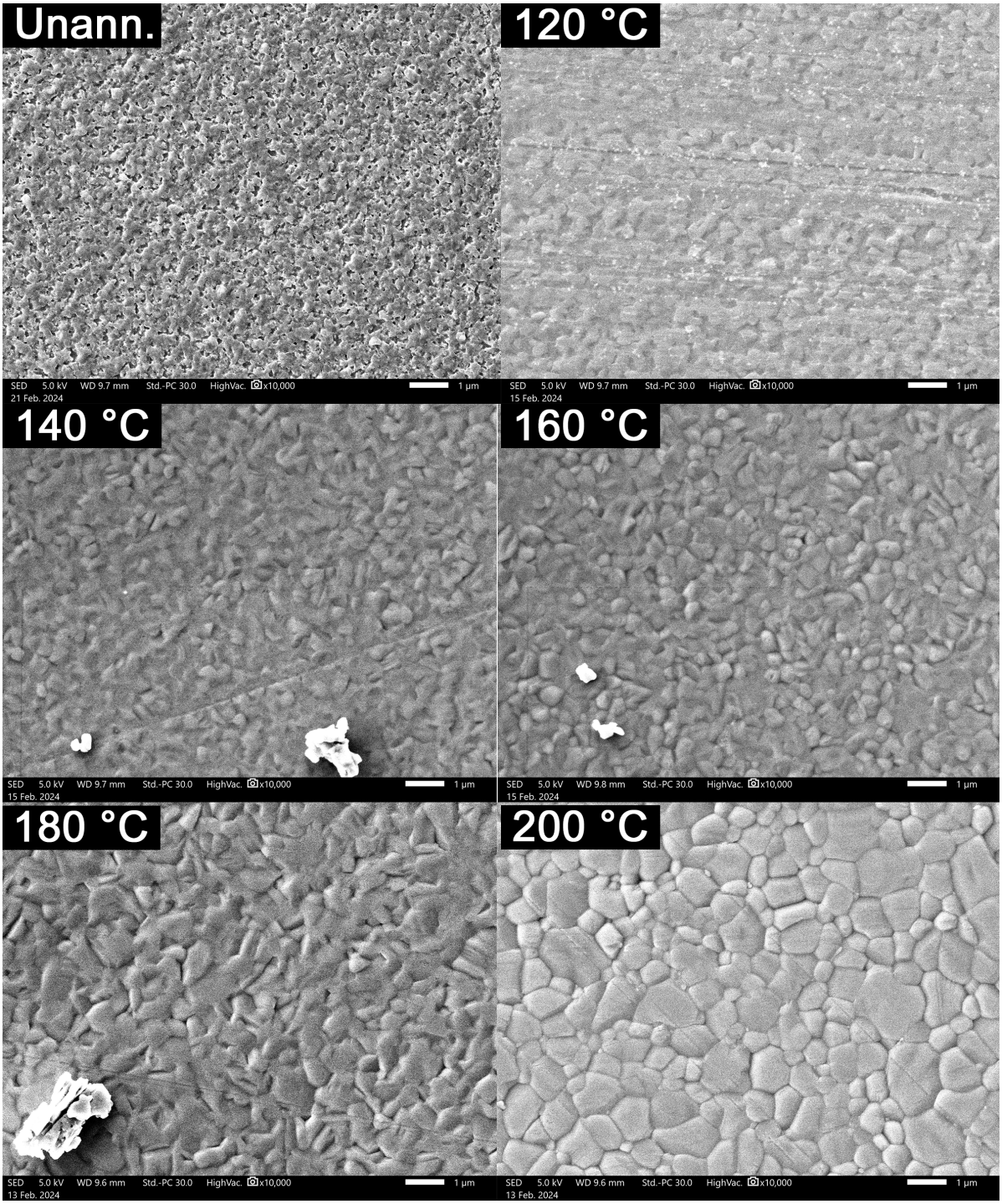

Figure B.7: SEM images of the $Cs_{0.05}FA_{0.75}Pb_{0.5}Sn_{0.5}I_3$ annealing trend taken at a magnification of 10,000x. The scratches observed in the 120, 140 and 160 °C are damage as a result of storage. The dark area seen in the 180 °C sample is caused by a previous scan etching the surface.

B.3. Appendix B3: $Cs_{0.05}FA_{0.75}Pb_{0.5}Sn_{0.5}I_3$, Reverse Deposition Order

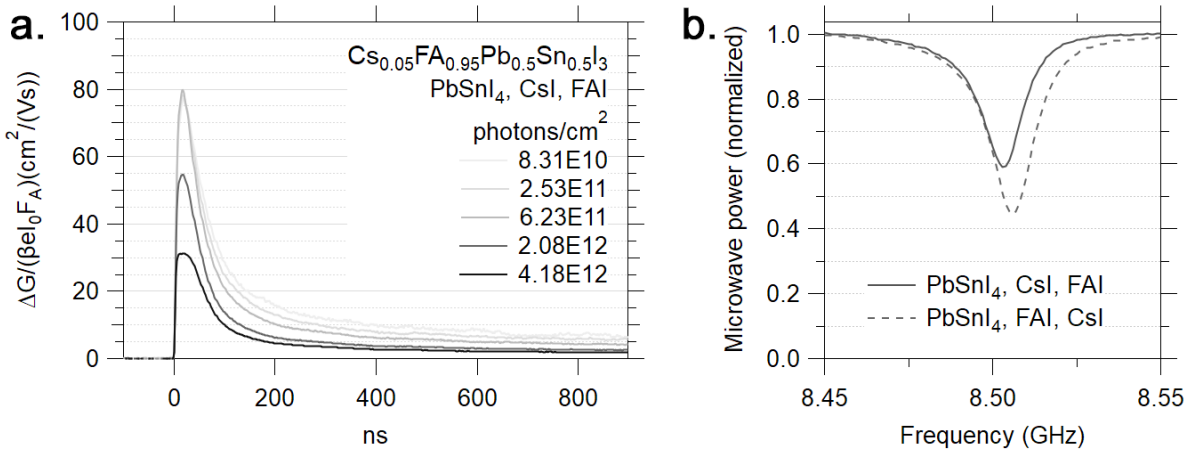

Figure B.8: a. TRMC plot of $Cs_{0.05}FA_{0.75}Pb_{0.5}Sn_{0.5}I_3$ deposited in reversed order ($PbSnI_4$, CsI, FAI), annealed at 200 °C. **b.** SSMC plot of $Cs_{0.05}FA_{0.75}Pb_{0.5}Sn_{0.5}I_3$ deposited in normal and reversed order.

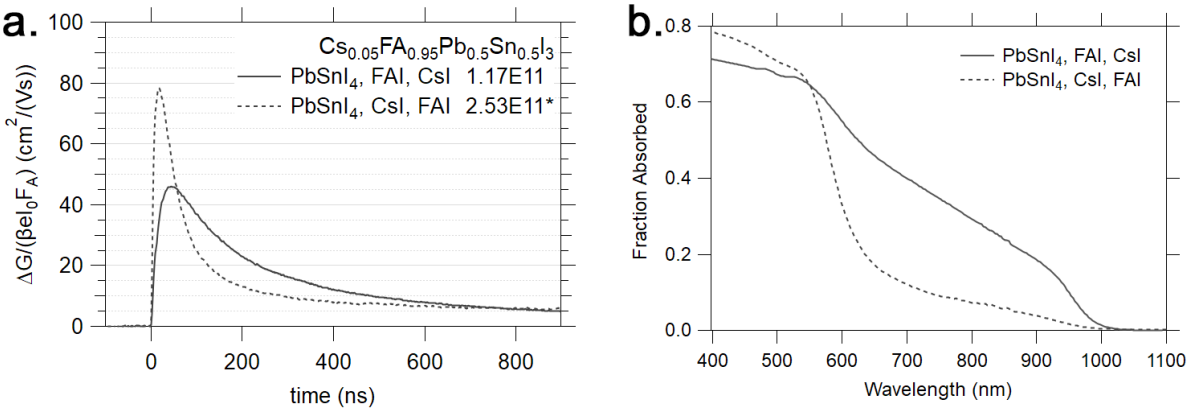

Figure B.9: a. Comparison between TRMC traces of $Cs_{0.05}FA_{0.75}Pb_{0.5}Sn_{0.5}I_3$ deposited in normal and reversed order. Note: although the fluencies are similar, the difference in absorption makes direct comparison difficult. **b.** Comparison between absorption spectra of $Cs_{0.05}FA_{0.75}Pb_{0.5}Sn_{0.5}I_3$ deposited in normal and reversed order. Note the large difference in absorption. The absorption was not normalized for thickness as the measured thickness was comparable.

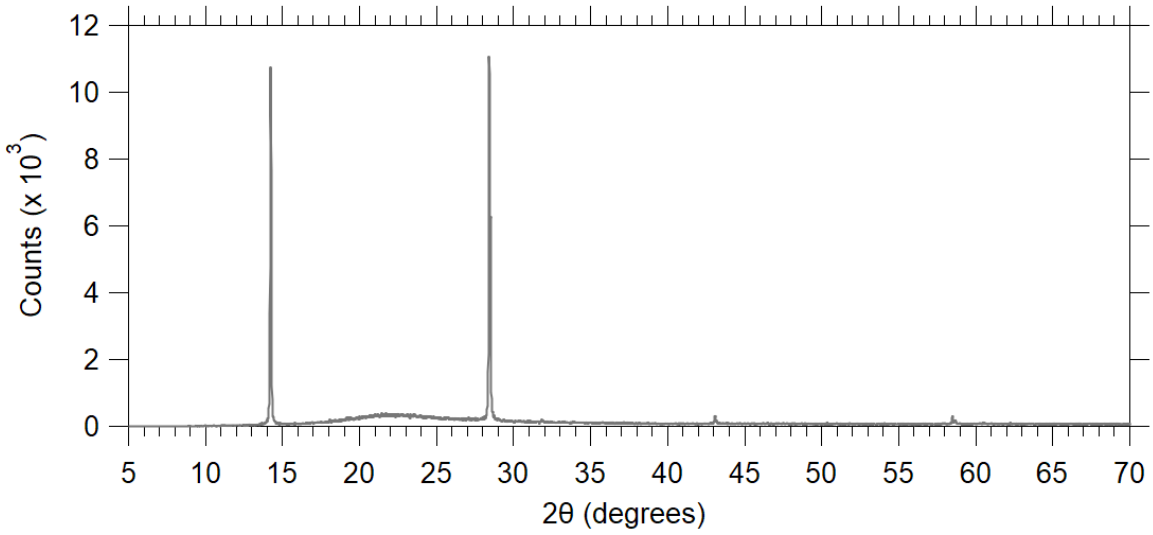

Figure B.10: XRD spectrum of $Cs_{0.05}FA_{0.75}Pb_{0.5}Sn_{0.5}I_3$ deposited in reverse order, annealed at 200 °C.

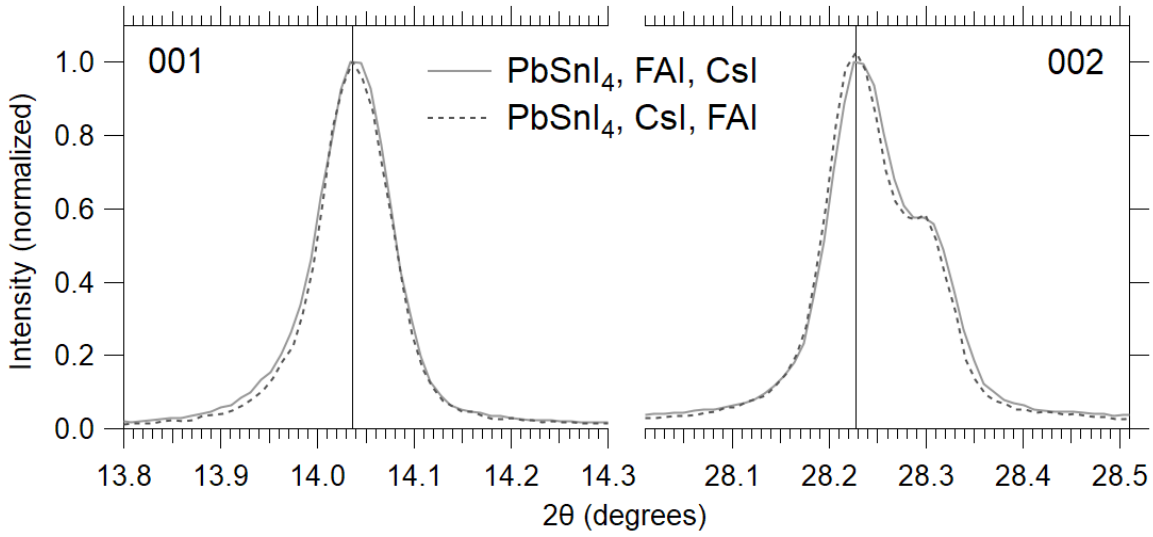

Figure B.11: Comparison of the 001 and 002 peaks of the XRD spectrum of $Cs_{0.05}FA_{0.75}Pb_{0.5}Sn_{0.5}I_3$ deposited in normal and reverse order annealed at 200 °C.

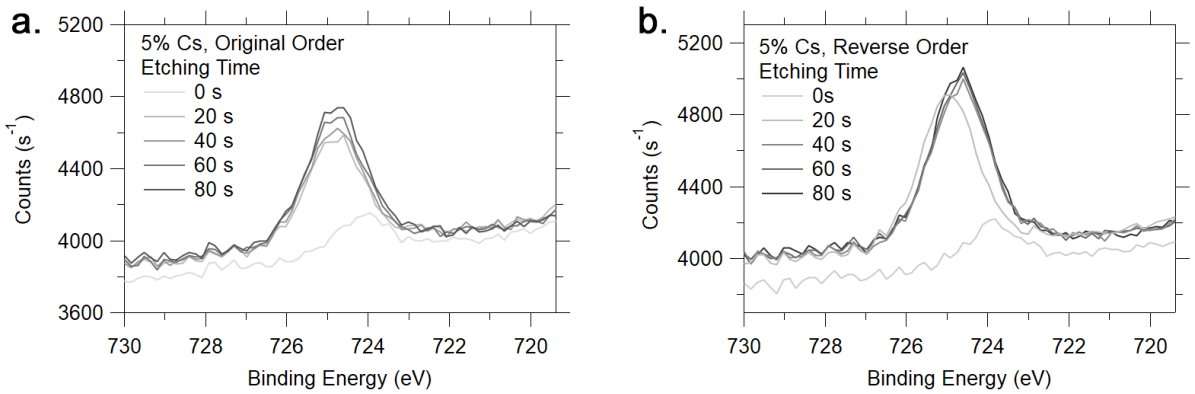

Figure B.12: XPS depth profile of $Cs_{0.05}FA_{0.75}Pb_{0.5}Sn_{0.5}I_3$ deposited in normal and reverse order, annealed at 200 °C.

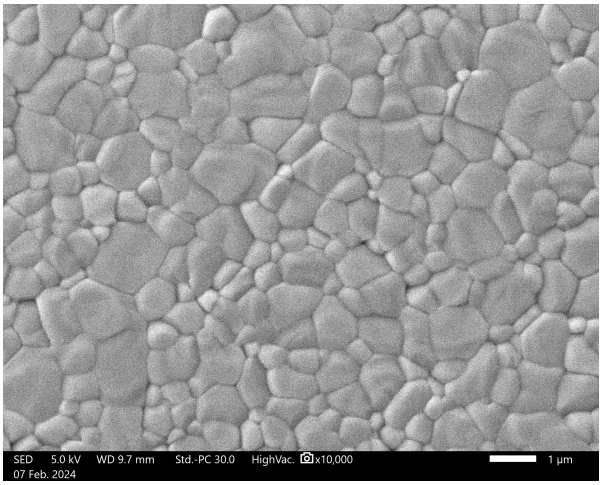

Figure B.13: SEM image of XRD spectrum of $Cs_{0.05}FA_{0.75}Pb_{0.5}Sn_{0.5}I_3$ deposited in reverse order, annealed at 200 °C at a magnification of x10,000.

C

APPENDIX C: EFFECT OF CESIUM FRACTION

Table C.1: Table showing the film thickness measured using stylus profilometry as a function of the A-site composition in $Cs_xFA_{1-x}Pb_{0.5}Sn_{0.5}I_3$.

Cs Composition	0%	5%	25%	40%
Thickness (nm)	145.24 ± 8.07	147.44 ± 7.82	143.48 ± 5.22	151.67 ± 13.78

Table C.2: Table showing the ratio of Sn:Pb as measured by EDS versus A-site composition in $Cs_xFA_{1-x}Pb_{0.5}Sn_{0.5}I_3$. Minimum of 10 measurements were performed per composition.

Cs Composition	Ratio Sn:Pb
0%	1:1.08 ± 0.21
5%	1:1.01 ± 0.14
25%	1:1.02 ± 0.12
40%	1:1.36 ± 0.35

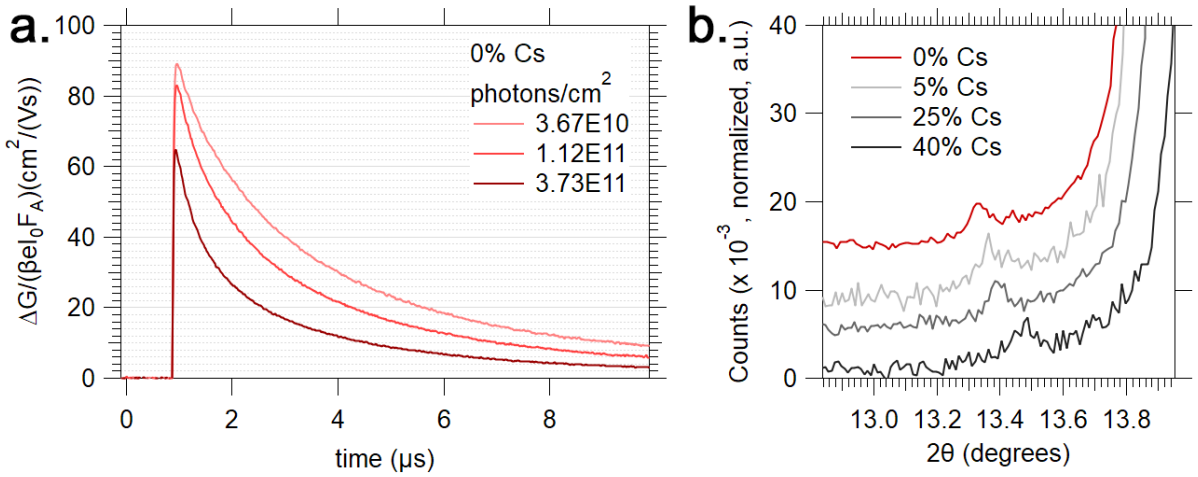

Figure C.1: a. TRMC plot of $FAPb_{0.5}Sn_{0.5}I_3$ with a longer timescale of 10 μs. **b.** Normalized XRD of the δ phase peaks in $Cs_xFA_{1-x}Pb_{0.5}Sn_{0.5}I_3$

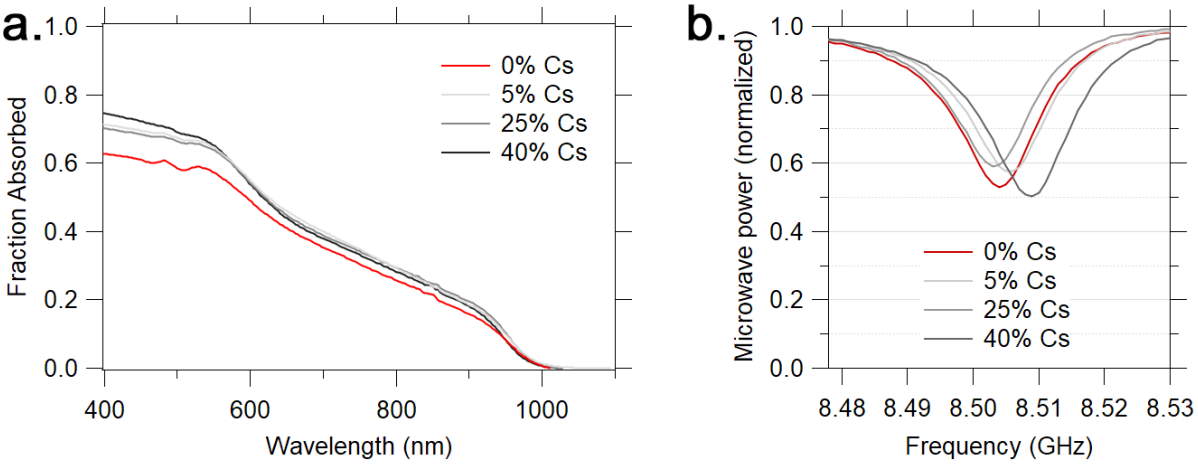

Figure C.2: a. UV-Vis-NIR absorption spectrum (not normalized for thickness) and **b.** SSMC of $Cs_xFA_{1-x}Pb_{0.5}Sn_{0.5}I_3$.

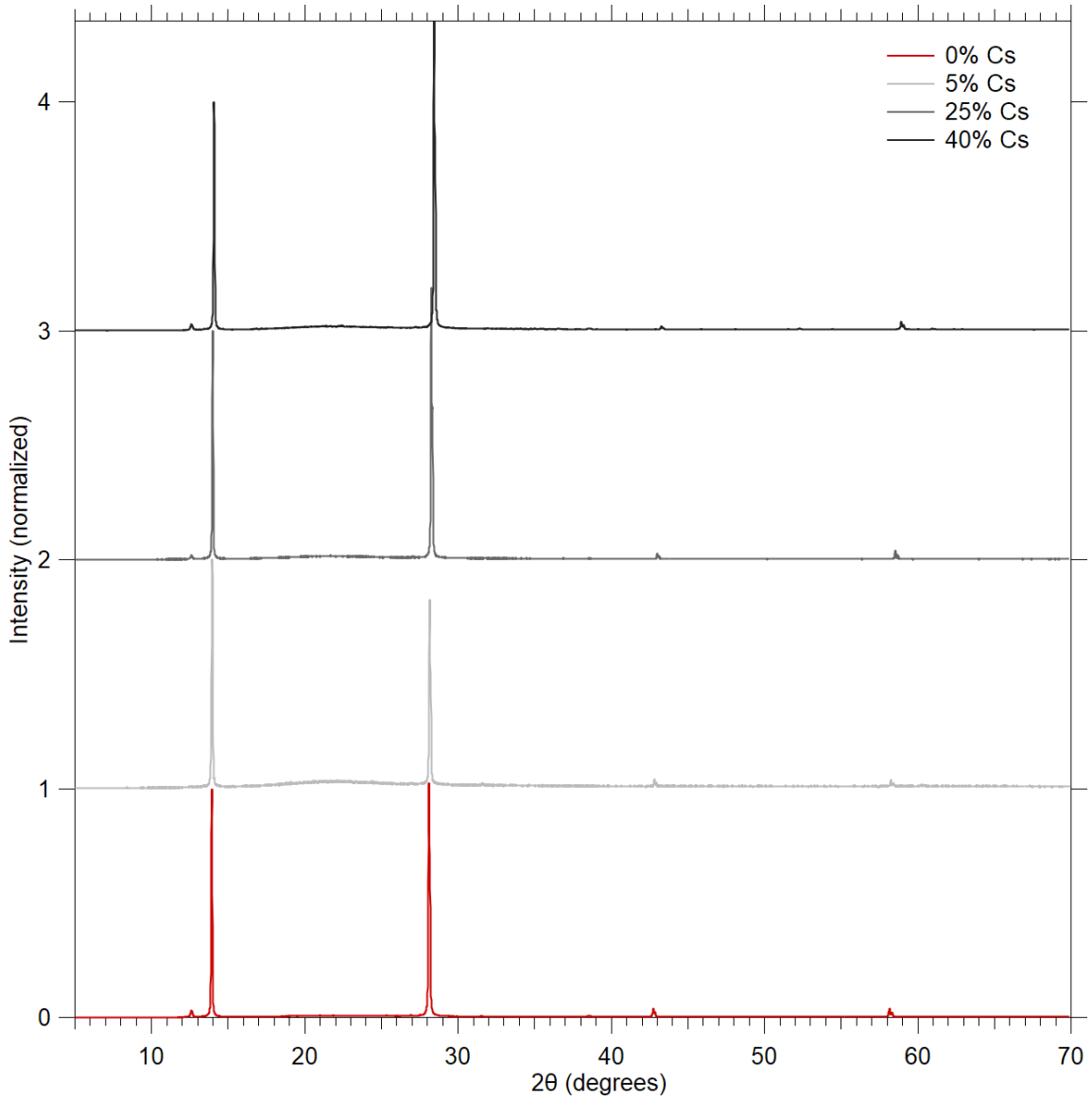

Figure C.3: Full normalized XRD spectra of $Cs_xFA_{1-x}Pb_{0.5}Sn_{0.5}I_3$.

D

APPENDIX D: EFFECT OF SNF_2

Table D.1: Table showing the film thickness as measured using stylus profilometry of $FAPb_{0.5}Sn_{0.5}I_3$ annealed at 200 °C with and without 10 mol% SnF_2.

SnF_2	0%	10%
Thickness (nm)	145.24 ± 8.07	168.45 ± 7.31

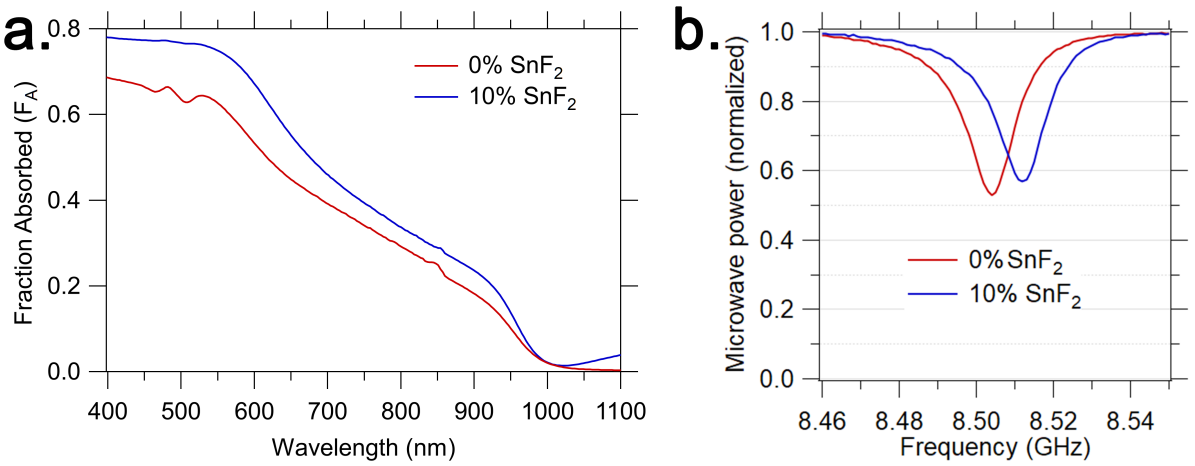

Figure D.1: Plots showing the **a.** UV-Vis-NIR absorption spectrum (non-normalized for thickness) and **b.** SSMC of $FAPb_{0.5}Sn_{0.5}I_3$ annealed at 200 °C with and without 10 mol% SnF_2. The position of f_0 is shifted due to differences in quartz substrate dimensions.

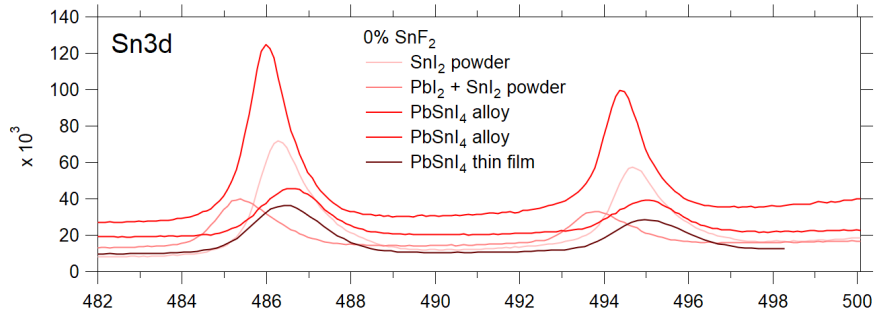

Figure D.2: XPS spectrum showing the change in binding energy of the Sn3d electrons in the various stages of production without SnF_2.

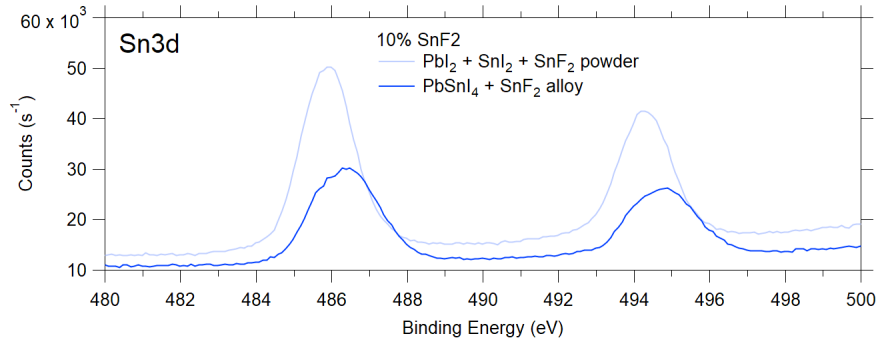

Figure D.3: XPS spectrum showing the change in binding energy of the Sn3d electrons from raw materials to alloy of production with 10 mol% SnF_2

E

APPENDIX E: SYNTHESIS PROTOCOLS

Mask Design and Substrate Holder

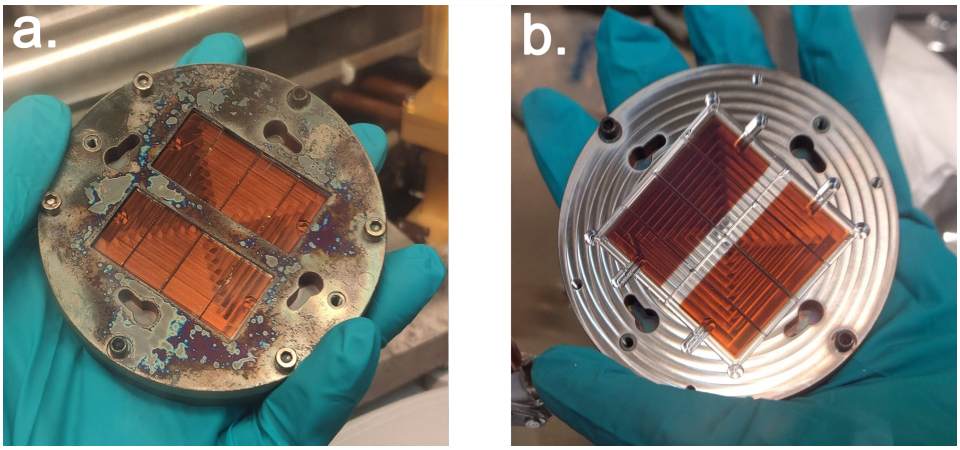

Figure E.1: Substrate holder containing deposited samples with (**a.**) and without (**b.**) a mask. The substrate holder can be loaded with a maximum of eight substrates. The coverage area is shown in image **b.**.

Powder Exchange

The vacuum pump of the evaporation was turned off, and allowed to spin down. A fume extractor was placed on top of the lid of the evaporation chamber. Next, N_2 flow was introduced until a positive pressure was reached, indicated by the lid of the chamber opening slightly. The lid of the chamber was opened, and the fume extractor was positioned on top of the opened chamber.

To remove the crucibles, the substrate and source shutters were opened. Next, the mantles were removed from the crucibles and stored inside the chamber. The crucibles were removed and covered with aluminium foil while being held inside the chamber. Now the aluminium foil covered crucibles could be transferred to the ante chamber of a glovebox in which the precursors were stored. The aluminium foil was removed from the crucibles once inside of the ante chamber to avoid the introduction of oxygen into the glovebox.

Once inside the glovebox, the crucibles were refilled. CsI was refilled by eye to a layer of 0.5 to 1 cm. Any old FAI was removed from its crucible and 350-500 mg of new FAI was added to the crucible using a microbalance. CsI was refilled when (close to being) empty. FAI was replaced every three to four depositions. Glass crucibles are used for the inorganic compounds, while a polymer crucible is used for the FAI source.

After refilling the crucibles, they were covered in aluminium foil and transferred out of the glovebox to the evaporator chamber. Once inside the evaporator chamber, the aluminium foil was removed, and the crucibles were placed inside their respective sources. The substrate and source shutters were shut and the lid of the evaporation chamber was closed. The N_2 flow was shut off, and

the chamber was returned to vacuum.

Replacing Quartz Crystal Microbalance (QCM)

During each powder exchange, the condition of the QCM was checked. If the resonance frequency of the QCM was less than 90% of the original resonance frequency it was replaced.

Alloying of $PbSnI_4$

Under N_2 atmosphere, SnI_2 powder was prepared by grinding the pellets in a pestle and mortar. For 1 gram of $PbSnI_4$, 553.1 mg PbI_2 powder and 446.9 mg SnI_2 powder were weighed on a microbalance and combined in a glass crucible to form a orange-yellow mixture with a molar ratio of SnI_2:PbI_2 1:1.

Meanwhile, the vacuum pump of the evaporation chamber was deactivated. After the pump had spun down, the N_2 flow was opened to bring the chamber to positive pressure. A fume extractor was positioned on top of the chamber. The chamber could now be opened. Next, the fume extractor was positioned on top of the open chamber.

Next, the crucible containing the powder mixture was fully covered with aluminum foil and transferred through ambient atmosphere to the opened chamber of the evaporation set-up. Next, the crucible was placed inside a mantle at the bottom of the evaporation chamber. The opening of the source was covered with aluminium foil to prevent evaporation during alloying. The evaporation chamber was now closed, N_2 flow was stopped, and the chamber was returned to vacuum. The lid of the chamber was secured using the knob.

After the chamber had reached a pressure of $<10^{-5}$ bar, the vacuum pump was turned off. Once the vacuum pump had spun down, N_2 flow was introduced to bring the chamber to atmospheric pressure. Finally, the N_2 flow was turned off, and the vacuum pump was turned on. This procedure was performed three times in total.

After the chamber had been flushed three times, the vacuum pump was turned off, and N_2 flow was introduced once the vacuum pump had spun down. After atmospheric pressure had been reached inside the chamber, the N_2 flow was turned off.

The heating element corresponding to the source which contains the PbI_2/SnI_2 powder mixture was turned on. Starting from ambient temperature, the temperature was increased in increments of 20-30 °C to 420 °C. This procedure was performed quickly, as to prevent excess evaporation of the components. Once 420 °C was reached, this temperature was held for 20 minutes.

After being heated for 20 minutes at 420 °C, the heating was turned off, and the source was allowed to cool to ambient temperatures. After reaching ambient temperatures, the evaporation chamber was returned to vacuum.

The knob securing the lid was unscrewed and the vacuum pump was turned off. After the vacuum pump had spun down, N_2 flow was introduced into the chamber until a positive pressure had been reached. A fume extractor was positioned on top of the chamber. The chamber could now be opened.

To use the alloy, the aluminum foil covering the crucible was removed while the crucible remained placed in the mantle. The lid of the chamber was closed, and N_2 flow was stopped. The chamber was then returned to vacuum.

To store the alloy, the crucible was removed from the mantle and covered in an additional layer of aluminum foil while still inside the chamber. Next, the covered crucible was transferred to the ante chamber of a glovebox, being careful to remove the aluminum foil once inside the ante chamber. The crucible was now brought into the glovebox and stored in a closed container. In the end, a crimson red colored ingot was obtained (figure 4.1). The evaporation chamber was closed, N_2 flow stopped, and the vacuum pump was turned on.

Alloying of $PbSnI_4$ + 10 mol% SnF_2

The procedure of the synthesis of $PbSnI_4$ + 10 mol% SnF_2 was identical to that of $PbSnI_4$ described above, with the addition of 18.8 mg of SnF_2 to the mixture of 446.9 mg SnI_2 and 553.1 mg PbI_2 before alloying.

Substrate Cleaning

Two Petri dishes were cleaned with 2-propanol (IPA) and acetone, and dried using a Kimtech Science tissue. Eight quartz plates were placed inside one of the Petri dishes. The Petri dish containing the substrates was filled with a small layer of IPA. Each quartz plate was individually dried using a Kimtech tissue and placed in the dry Petri dish. Once all substrates were dried off, the Petri dish containing the IPA was emptied, cleaned using acetone and then dried using a Kimtech tissue. Next, the Petri dish containing the samples was filled with a small layer of acetone. Again, the substrates were individually wiped down with a Kimtech tissue and placed in the dry Petri dish. Finally, the Petri dish containing the substrates was placed inside a Harrick Plasma plasma-ozone cleaner for at least ten minutes.

Substrate Loading

After the substrate cleaning procedure was completed, the quartz plates were placed on top of the substrate holder. Next, the substrate mask was placed on top, and attached using four bolts.

The substrate holder and the transfer unit were placed inside the ante chamber of the evaporation set-up. Once the ante chamber was closed, the load lock vacuum pump was deactivated. After coming to atmospheric pressure, the load lock was opened, and the substrate holder was positioned upside down on top of the transfer arm. The load lock was closed, and the vacuum pump reactivated.

Once the pressure in the evaporation chamber and the load lock was equal, the gate separating them was opened, and the substrate holder was transferred inside. The substrate holder was attached to the spindle inside the evaporation chamber, and the transfer arm was retracted. Finally, the gate between the evaporation chamber and the load lock was closed.

Substrate Unloading

Once a deposition was completed and the measured deposition rate reached zero, the gate between the evaporation chamber and the load lock was opened. The substrate holder was retrieved using the transfer arm. The gate was closed, and the load lock vacuum pump was turned off. Once the load lock reached atmospheric pressure, the lid was opened, and the substrate holder was retrieved. The substrate holder was then placed inside the transfer unit, and the transfer unit was closed. The lid of the load lock was replaced, and the load lock vacuum pump was reactivated.

Next, the ante chamber of the evaporation set-up was opened, and the transfer unit was retrieved. The transfer unit was then brought into a glovebox and opened. The substrate mask was removed to retrieve the coated substrates (figure E.1).

Sample Storage

The coated substrates were placed in plastic sample trays which were then covered in aluminium foil. The entire package was stored inside a lidded plastic box inside of the glovebox. For long=term storage, samples were sealed inside vacuum bags.